UNIVERSITÀ DEGLI STUDI DI BERGAMO

PROCEEDINGS OF THE DIPSI WORKSHOP 2012

Droplet Impact Phenomena & Spray Investigations

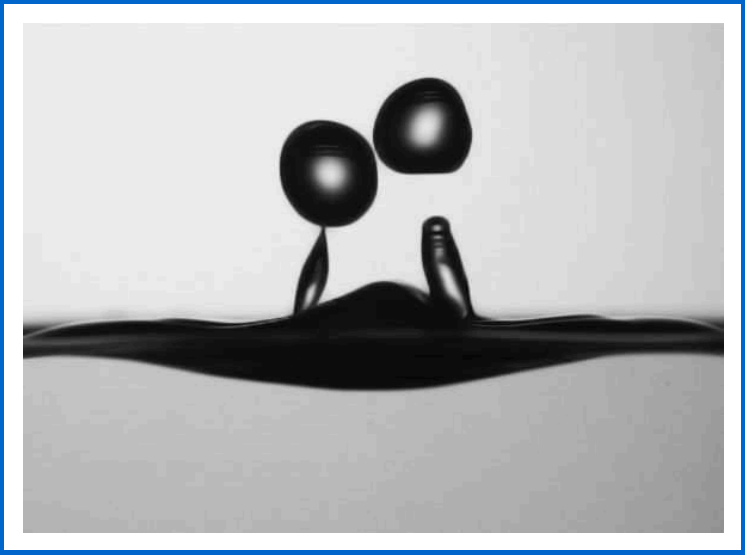

Double drop impact onto liquid pool

BERGAMO, ITALY, 18TH MAY 2012

UNIVERSITÀ DEGLI STUDI DI BERGAMO

PROCEEDINGS OF THE DIPSI WORKSHOP 2012

Droplet Impact Phenomena & Spray Investigations

BERGAMO, ITALY, 18TH MAY 2012

PROCEEDINGS OF THE DIPSI WORKSHOP 2012
Droplet Impact Phenomena & Spray Investigations

Editors
Gianpietro Elvio Cossali and Simona Tonini
Industrial Engineering Department
Università degli Studi di Bergamo
Viale Marconi 5, 24044 Dalmine, Italy
e-mail: elvio.cossali@unibg.it
simona.tonini@unibg.it

p. 50 - cm 29,7
ISBN – 978-88-97413-04-2

Preface

This Proceedings contains the papers presented at the DIPSI Workshop 2012 on Droplet Impact Phenomena and Spray Investigation, organised by the Università degli Studi di Bergamo on Friday 18th May 2012 in Bergamo, Italy.

This workshop, which is now at its sixth edition, represents an important opportunity to share the recent knowledge on droplets and sprays in a variety of research fields and industrial applications.

The support and sponsorship of the Department of Industrial Engineering of the Università degli Studi di Bergamo, Luchsinger s.r.l. and all the other participating are acknowledged and appreciated.

Bergamo, September 2012

Prof. Gianpietro Elvio Cossali

Main Sponsors

UNIVERSITÀ DEGLI STUDI DI BERGAMO
www.unibg.it

LUCHSINGER
www.luchsinger.it

Contents

SPRAY CHARACTERISATION AND HEAT TRANSFER DURING COOLING PROCESSES BY INTERMITTENT SPRAYS

Stephan BAER[1,C], Jürgen SCHMIDT[1]

[1]Institute of fluid mechanics and thermodynamics, Otto-von-Guericke University of Magdeburg, Universitätsplatz 2, 39106 Magdeburg, Germany
[C]Corresponding author: stephan.baer@ovgu.de

ABSTRACT
Spray cooling is used in many technical areas to cool hot materials. There are different boiling phenomena depending on the surface temperature. So the heat flow varies through these boiling ranges. Large local temperature gradients can cause mechanical tensions and also effect material properties strongly. Intermittent spray cooling offers much potential to ensure a uniform cooling, also in the crossing from film to transition boiling. In this work, a high pressure gasoline direct injector (HDEV-5) is used for spray investigations with water and infrared thermography recordings during cooling processes of a heated nickel alloy sheet. Additional measurements of droplet size and velocity by a phase Doppler analyzer (PDA) are conducted to characterise the spray properties. Furthermore, the local mass flux is determined by using a Patternator. The additional setting parameters of an intermittent spray can be expressed by the duty cycle (DC), which is composed of the frequency and the injection duration. This paper offers a basic characterisation of the spray and various physical mechanisms during a cooling process shown in temperature profiles.

INTRODUCTION

Higher requirements on industrial components or manufacturing processes leads to the demand for new ways of cooling technology. Especially in electronic systems, e.g. the cooling of microprocessors, but also in other applications high heat flux cooling systems had received more attention. Spray cooling is a common application to cool quickly and uniform. This technique provides the latent heat of nearly the entire cooling fluid [1].

Intermittent Spray Cooling (ISC) offers much potential to ensure a controlled cooling process. The parameter settings mass flux and droplet properties of a continuous spray can be extended by the frequency and the duration of injection. These additional values are summarized in the duty cycle ($DC = f_{inj} \cdot t_{inj} \cdot 100\%$) [2], which gives the control about the length of the injection breaks. These spray disruptions influence the local water saturation and therefore the extracted heat flow of the sheet.

There are different boiling regimes depending on the temperature of the sheet. It is very important to know the Leidenfrost temperature which depends on many fluid properties and parameters of the cooling process, e.g. the droplet diameter and velocity, the local mass flux and the roughness of the sheet. Furthermore it limits the stable film boiling from the transition and nucleate boiling regime. Above that temperature a vapour layer between water and sheet is formed, which has an insulating effect of removing the heat. By cooling below that limit the local heat fluxes grow due to the direct contact of water and solid [3, 4].

Previous works investigated the ISC with low pressure nozzles. Panão et al. [5] cooled a cylindrical copper block with an intermittent multijet spray with 1, 1.6 and 2.2 bar injection pressure. Fest-Santini [2] also used ISC for a study of the heat transfer coefficient in the stable film boiling regime. The applied injector was a Bosch EV14 low pressure (7 bar) gasoline injector and the cooled component was a nickel alloy sheet. It was shown that by using intermittent spray cooling and short injection durations coolant liquid could be saved.

In this work the injection pressure is increased up to 200 bar and the temperature range passes through film-, transition- and nucleate boiling regime. The chosen injector is a currently in the automotive industry used gasoline injection nozzle with water as working fluid. To investigate just one spray jet of the 6-hole injector due to symmetry, one injection hole is orientated vertically down. Furthermore the spray is characterised by PDA and Patternator measurements and visualized by high-speed-camera recordings. The temperature of the sheet during a cooling process is recorded with an infrared camera on the dry side. Initially, investigations of physical basic effects are in the focus and illustrated in temperature profiles.

METHODS AND MATERIALS

The experimental setup is based on a BOSCH® 6-hole gasoline direct injector (HDEV-5) used with water. It is triggered by a TTL pulse of a self-made trigger box and software. The investigated spray jet is separated and orientated vertically down. The material to be cooled is a (150x100x0.1 mm) nickel alloy sheet, which is directly electrical heated. The pressure application operates with nitrogen N_2, which directly loads the piston and has a transformation ratio low/high of 1/2. In addition to the below explained measuring systems, high-speed-recordings with a frequency of 5000 up to 40000 Hz are conducted to visualize the spray and the spray impact. The used camera is a High-Speed-Star-system from LaVision®.

Phase Doppler Analyzer (PDA)

The spray droplets are particularly characterised by their diameters and velocities. These properties are measured with the help of a PDA-system. The schematic experimental setup is shown in Figure 1. Two laser beam pairs create a measuring volume. Any droplet crosses this volume scatter the light of the laser beams and generate a doppler

displacement. Trough superposition of the doppler signals of the two laser beams a beat frequency is formed and can be measured with photodetectors. The frequency of that signal is proportional to the particle velocity. The determination of the droplet diameter is based on the effect of phase shifting. The scattered light is detected from a differently arranged receiver with a certain phase shift, which is proportional to the particle size [6].

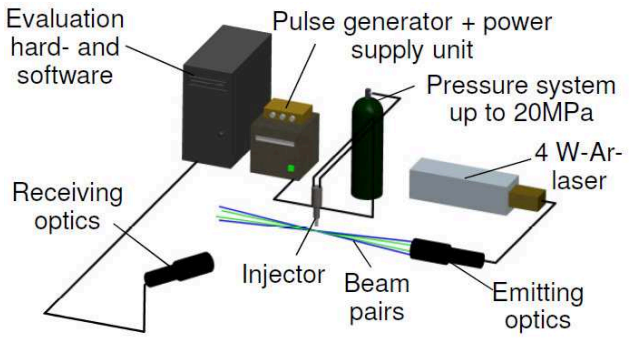

Figure 1: schematic experimental setup of the Phase-Doppler-Analyzer (PDA)

The measuring volume is placed on the position of the nickel alloy sheet by a traverse. The injector was placed above the measuring point. Consequently the distance between the crossed laser beams and the injector is varied from 100, 150, 200 up to 225 mm. In addition the measuring point is adjusted in the horizontal plane in one direction to capture the entire spray angle. Furthermore the injection pressures used are 50, 100 and 200 bar. The time of injection is set to 0.625, 1.25, 2.5 and 5 ms. As in [2] is shown, the PDA measurements are frequency independent.

The mean velocities and diameters are determined on the basis of time classes, which have a range of 50, partly 66 µs, to capture the high temporal dynamics of the spray. The usage of a small class size leads to high number of classes, so it is necessary to smooth the mean value profiles, which is done with a 30 point Savitzky-Golay smoothing filter. To characterise the droplet size the diameter d_{10} is chosen and is defined out of Eq. (1) [7, 8].

$$d_{ab}^{(a-b)} = \frac{\sum n_i \cdot d_i^{\,a}}{\sum n_i \cdot d_i^{\,b}} \qquad (1)$$

According to that, the d_{10} diameter is the arithmetic mean value of the droplets.

Patternator

This measuring system consists of eleven parallel tubes with a diameter d_R. These tubes are connected with glass containers through hoses with a certain coating so that water can directly drop in. The injector is placed above these tubes with the adjusted distance of 150 and 200 mm. After a certain period of measuring time the collected water masses of each glass container is determined through weighing. This procedure is done repeatedly to get a significant result. Afterwards a mean value is formed. The whole Patternator-system is traversed and shifted in steps with the value of the tube diameter. The duty cycles are adjusted to 2.5 and 5 %. Figure 2 shows the schematic experimental setup of the Patternator.

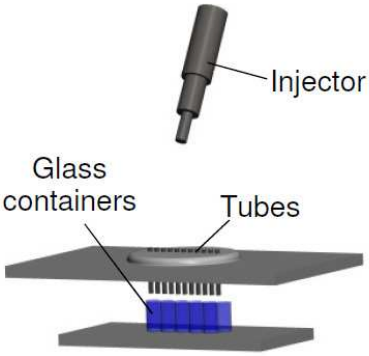

Figure 2: schematic experimental setup of the Patternator

Based on the weighed mass of water and the known geometric dimensions of the tubes, the local mass flux can be calculated from Eq. (2).

$$\dot{m} = \frac{M}{A_{tube} \cdot \Delta t_{inj}} = \frac{M}{\frac{}{4} \cdot d_R \cdot \Delta t_{inj}} \qquad (2)$$

Infrared thermography

To detect the surface temperature of the nickel alloy sheet, infrared thermography (IR) measurements are conducted. The IR-camera is placed on the dry side below the sheet, which has a black coat on the bottom side. The schematic experimental setup is shown in Figure 3. There is a certain temperature difference between wet and dry side, especially in the transition and nucleate boiling regime. In further investigations an inverse algorithm will be created to calculate the heat transfer coefficient of the wet side using the raw temperature signal of the bottom side.

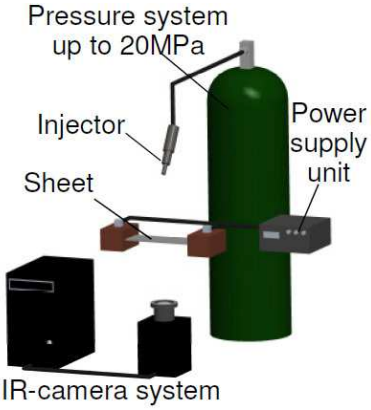

Figure 3: schematic experimental setup of the IR-measuring-system

The applied infrared camera was the Infratec ImageIR® 8300. The used resolution is 640 x 515 Px with 50 Hz uptake rate. The recorded section of the sheet is limited to the impact area of a single spray jet. In an evaluation routine the mean value of the 100 lowest temperatures is calculated to get temperature versus time profiles. The evaluated section is shown in figure 4 with an arbitrary view of an IR-recording. For the temperature profiles, there is another analysis routine to detect the Leidenfrost

temperature and a turning point temperature. These two points of the curves are defined as turning points and can be calculated.

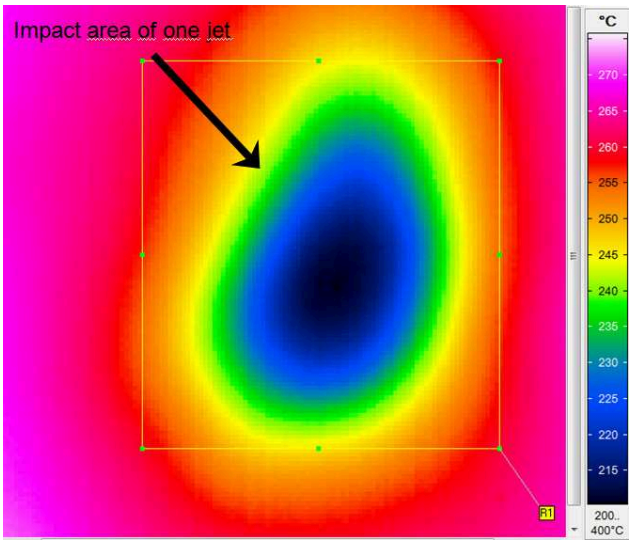

Figure 4: evaluation section of the impact area of the investigated spray jet

RESULTS AND DISCUSSION

The experimental results can be considered in two main categories. On the one hand the spray characterisation with the determination of the droplet properties (velocity and diameter) and the local mass flux, on the other hand the temperature profiles.

Spray characterisation

As an example, the distribution of the droplet velocity versus time shows figure 5, even the unsmoothed and smoothed mean value profile. Complementary, it illustrates the droplet number distribution to get more information about the dominant droplet speed. The same is illustrated for the droplet diameter, it is merely abstained from the unsmoothed profile versus time. This measurement is done in the spray centre with a liquid pressure of 200 bar, an injection duration of 5 ms and a distance of 150 mm. The first droplets which arrive at the measured volume are larger ones than the following. Smaller droplets are slowed down and influenced by the air resistance. Accordingly some droplets reaches a size of about 40 µm, but also very small ones are already measured. The bandwidth of the arriving spray has a wide range with a Δd of nearly 35 µm. The following droplets are predominant small with a size of less than 5 µm. This is shown very clearly in the histogram. Concerning to the velocity, there is a wide range, especially around the time when the spray arrives. The first droplets are consequently faster as the following spray particles. Its velocity ranges from slow ones with 5 m/s up to very fast ones with over 40 m/s. Afterwards the value decreases and settles to round about 5 m/s.

This effect is illustrated in some high-speed-recordings in figure 6. The first droplets which arrives at the sheet are isolated and large compared to the rest of the particles. The spray reaches the sheet subsequent of these drops. It is clearly shows a higher density and the droplets are smaller.

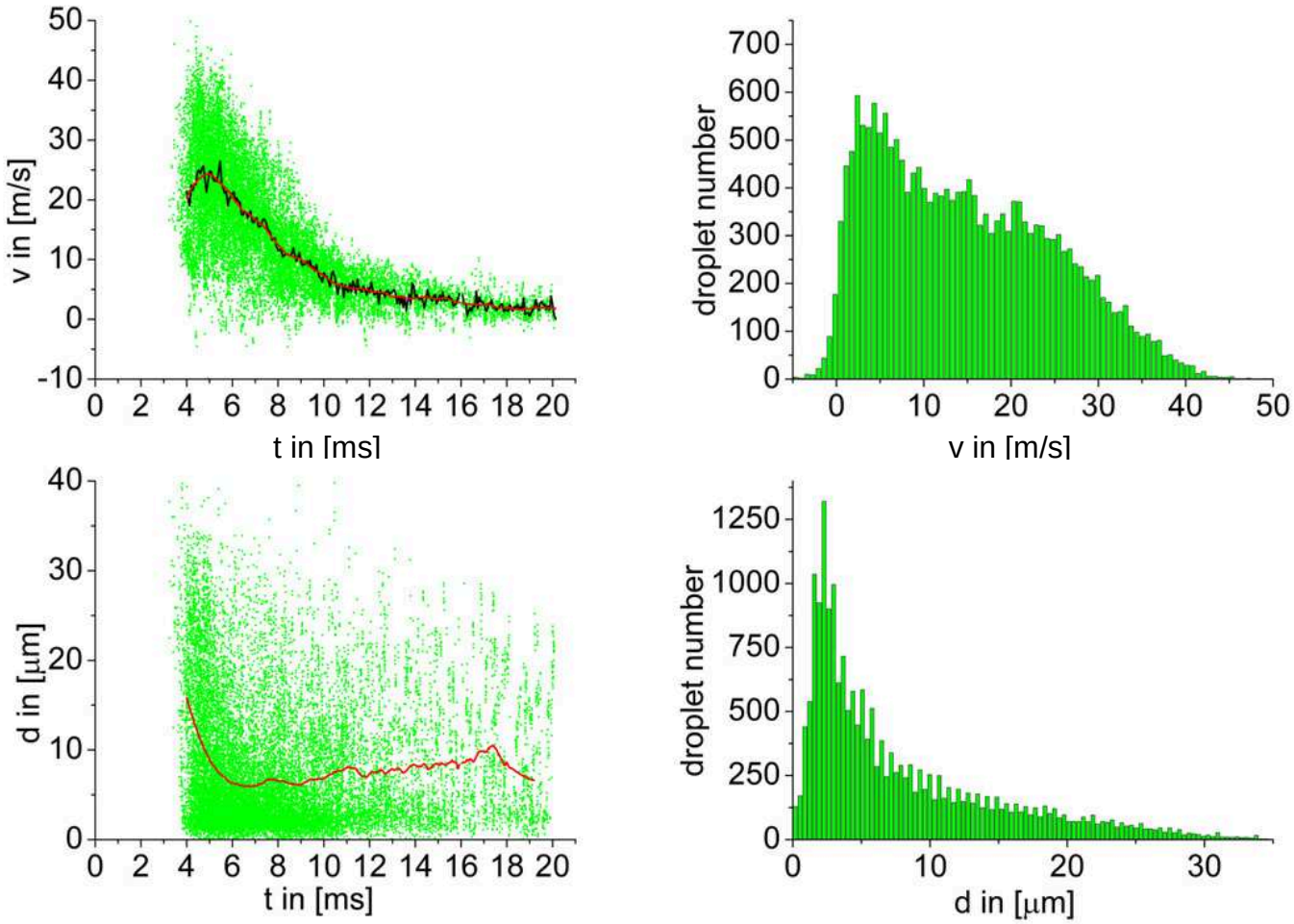

Figure 5: Illustration of the droplet velocity and diameter distribution

They also has to be slower, because they arrive with a certain offset.

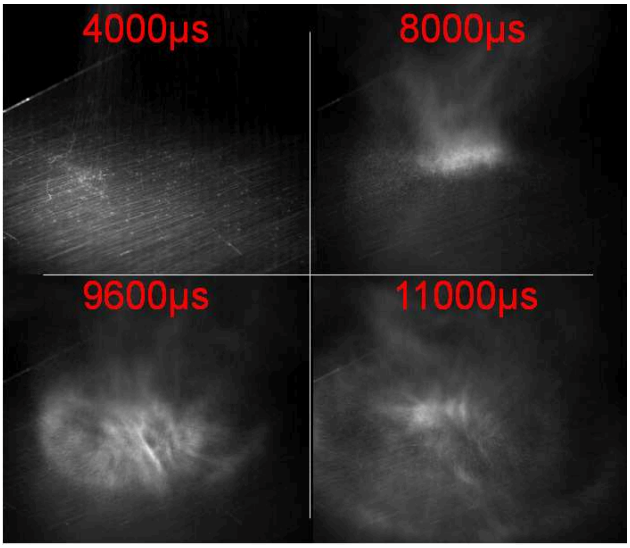

Figure 6: High-speed image sequence at certain points of time of a spray impact

Figure 7 illustrates some comparisons between parameter settings and their influence on the main droplet size (d_{10}). Increasing the distance between nozzle and nickel alloy sheet only the arrival time of the spray changes. The applied injection pressure is constantly 200 bar. With doubling the distance from 100 to 200 mm the spray takes three times as much time to get the range. But the droplet diameters are still similar, just the first arriving ones are insignificant smaller at bigger distances.

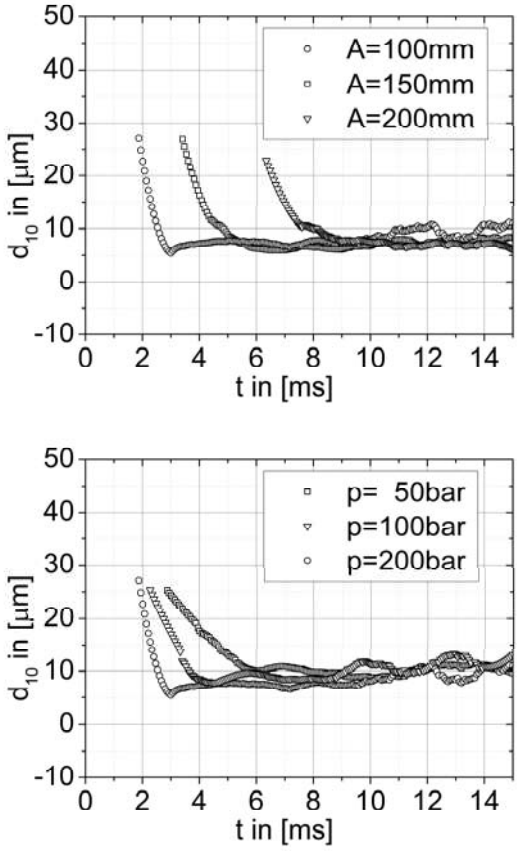

Figure 7: Influence of distance A and injection pressure p of the mean droplet diameter d_{10}

Increasing the injection pressure results in smaller droplet diameters. The spray also arrives earlier at the sheet and gets faster smaller droplets than with less liquid pressure. Following the spray front, the d_{10} droplet diameter settles to a certain value, which is from approximately 7 µm at 200 bar up to 10 µm at 50 bar. These experiments are performed in a distance between nozzle and sheet of 100 mm.

The local mass flux is illustrated in figure 8 for a distance of 150 mm, a liquid pressure of 200 bar, an injection time of 10 ms and a duty cycle of 5 %. In relation to the impact area of one jet in comparison with the results of [2], the local mass flux is about twice as high in this experiment. This is mainly due to the higher injection pressure used.

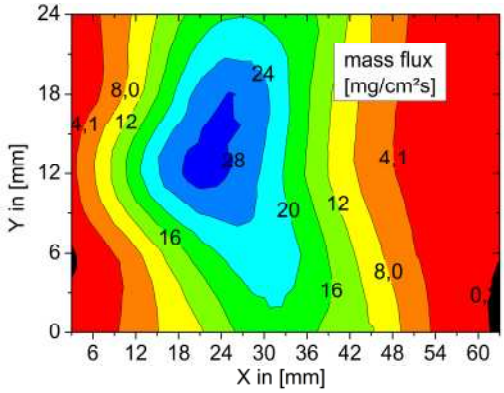

Figure 8: Local mass flux $\dot{m}$ of one vertically down directed spray jet

A cooling sequence reaching over all boiling regimes is illustrated in figure 9. The parameter setting for this example is a distance of 100 mm, an injection pressure of 50 bar, a frequency of 5 Hz and a duty cycle of 0.625 %. The different ranges and temperatures are marked. The Leidenfrost temperature acts as the transition between the boiling regimes.

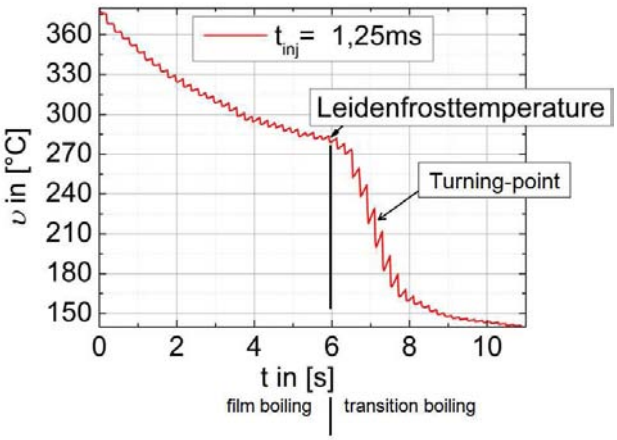

Figure 9: Temperature profile during a cooling process versus time

The difference of the temperature drops during an injection between film- and transition boiling regime are very significant. The process of cooling down 100 K takes roughly just one second after exceeding the Leidenfrost-temperature. In contrast to that this process takes six times

longer in the film boiling regime. Due to these large differences in the cooling velocities it is not trivial to calculate heat transfer coefficient of the wet side out of the temperature signal of the dry side of the sheet. In this boiling range it is no longer permitted to neglect the heat conduction in the sheet in reference to the heat transfer (Bi>0.1). Therefore this results in an inverse problem, which will be solved in future works.

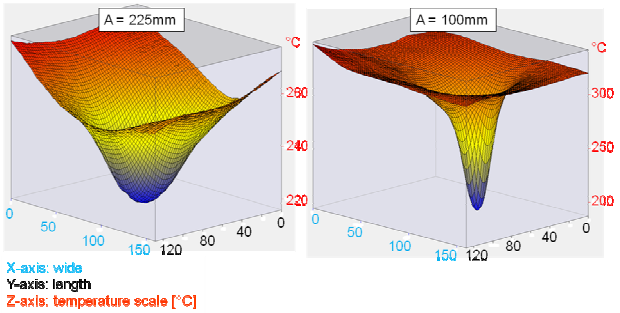

Figure 10: Temperature distribution of the spray impact area at the turning point time

In the investigation of the parameter variation for the IR-measurements a larger and more homogenous temperature field is aimed. Figure 10 illustrates the field at the turning point time for two different distances between sheet and injector. The used injection pressure is 100 bar and the duty cycle is 0.625 % with a injection time of 1.25 ms. The larger distance leads to a more uniform distribution of the spray and as a consequence a more uniform temperature distribution. This is very important for the evaluation and also for the avoidance of mechanical stresses.

CONCLUSION

This paper reports experimental studies to characterise the spray of an gasoline direct injector used with water and shows its potential for intermittent spray cooling. The possibility to work with high injection pressure leads to predominantly very small droplets. It also influences the mass flux, so that very short injection times are possible. The local mass flux has a big influence on the heat flux, especially in the transition boiling regime. High pressure and larger distances create a larger impact area, which provides a more uniform temperature distribution on the sheet.

However, the dry surface temperature profiles are shown for all boiling regimes. Large differences in the cooling behaviour make it impossible to determine the temperature or the heat transfer coefficient of the wet side in a trivial way.

Future work will include an inverse algorithm to calculate the additional information of the wet side of the sheet. Final infrared measurements with a certain parameter setting will be used as a basis for this calculation.

ACKNOWLEDGMENT

The financial support of the German Research Foundation (DFG-Graduiertenkolleg 1554 “Micro-Macro-Interactions in Structured Media and Particle Systems”) is gratefully acknowledged.

REFERENCES

[1] Panão M. R. O., Moreira A. L. N., ***Intermittent spray cooling: A new technology for controlling surface temperature***, International Journal of Heat and Fluid Flow 30 (2009), pp 117-130, DOI: 10.1016/j.ijheatfluidflow.2008.10.005.

[2] Fest-Santini S., ***Wärmeübergang bei der Sprühkühlung mit intermittierenden Sprays oberhalb der Leidenfrosttemperatur,*** PhD thesis, Otto-von-Guericke Universität Magdeburg, Germany, 2009.

[3] Weickgenannt C. M., Zhang Y., Sinha-Ray S., Roisman I.V., Gambaryan-Roisman T., Tropea C., Yarin A.L., ***Inverse-Leidenfrost phenomenon on nanofiber mats on hot surfaces***, Physical Review E84, 036310 (2011), DOI: 10.1103/PhysRevE.84.036310.

[4] Bernardin J. D., Mudawar I., ***The Leidenfrost Point: Experimental Study and Assessment of Existing Models***, Trans. ASME, 121, 894-903 (1999)

[5] Panão M. R. O., Correira A. M., Moreira A. L. N., ***High-power electronics thermal management with intermittent multijet sprays***, Applied Thermal Engineering 37 (2012), pp 293-301, DOI: 10.1016/j.applthermaleng.2011.11.031

[6] Prommersberger K., ***Untersuchung der Gemischaufbereitung in Gasturbinenbrennkammern unter Berücksichtigung der Eigenschaften kommerzieller Flüssigbrennstoffe***, PhD thesis, Universität Karlsruhe (TH), Germany, 20/2004

[7] Mugele R. A., Evans H. D., ***Droplet Size Distribution in Sprays***, Ind. Eng. Chem., 1951, 43 (6), pp 1317–1324, DOI: 10.1021/ie50498a023

[8] Ashgriz N., ***Handbook of Atomization and Sprays***, Springer Science+Business Media, 2011, DOI: 10.1007/978-1-4419-7264-4.

DROP IMPACT MORPHOLOGY ON HEATED SURFACES

Kate BLACK[1], Volfango BERTOLA[2,C]

[1]University of Liverpool, School of Engineering, Brownlow Hill, Liverpool L69 3GH (United Kingdom)
[C]Corresponding author: Volfango.Bertola@liverpool.ac.uk

ABSTRACT
The impact morphology of water drops on a polished aluminium surface has been studied experimentally by high-speed imaging, for surface temperatures between 50°C and 400°C, and Weber numbers up to 160. Five impact regimes are defined based on the final outcome of the impact: three independent regimes (secondary atomisation, rebound, and splashing), and two mixed regimes (rebound with secondary atomisation and splashing with secondary atomisation). Impact regimes are displayed on a quantitative two-dimensional map, having the surface temperature and the impact Weber number at ambient conditions as coordinates. Some characteristics of the transition boundaries between impact regimes are discussed.

INTRODUCTION

The impact of liquid droplets on heated surfaces is a complex phenomenon, characterised by a close interplay of hydrodynamics with different heat transfer modes, under large spatial and temporal gradients of the state variables (see, e.g., [1]). Despite its complexity, and the fundamental scientific challenges it gives the research community, drop impact on heated surfaces is commonplace in several practical applications. These include spray cooling, painting, inkjet printing for advanced manufacturing processes, and nuclear reactor safety

From a qualitative standpoint, this phenomenon consists of three stages: approach (between drop generation and impact), spreading (between impact and maximum spreading), and final outcome (after maximum spreading).

During the approach to a heated surface, the drop falls in counter-flow to a rising plume of hot air. This initiates to initiates to heat the liquid, and slightly reduces the impact velocity with respect to the theoretical free-fall velocity; moreover, the drop is exposed to radiation from the heated surface, which is not negligible at higher temperatures.

After impact, the drop spreads on the heated surface in a short lapse of time (~5 ms), increasing the area exposed to heat transfer. This induces a heat transfer regime that can be related to the well-known boiling curve. In particular, one can observe convection for surface temperatures below the boiling point of the liquid, nucleate boiling, film boiling, where the drops is separated from the surface by a vapour cushion, and transitional boiling, where the said vapour cushion is unstable and the liquid may locally get into contact with the surface.

After maximum spreading, different final outcomes are possible, depending on the impact velocity, the fluid and surface properties, and the surface temperature. If perturbations on the free surface of the liquid are too large, then the drop will break down into smaller droplets (splashing). Otherwise, it will recoil in order to minimise the surface energy, and eventually bounce off the surface if there is sufficient kinetic energy at the end of the recoil.

Early studies of this phenomenon focused on the heat transfer characteristics [2], [3], and less attention was paid to drop impact morphology due to the limitations of stroboscopic imaging [4]. Later on, the development of high-speed imaging has allowed researchers to visualise and analyse more quantitatively the various impact regimes [5]-[7]. However, a comprehensive and detailed study of drop impact morphology on heated surfaces using 3-D imaging was published only very recently [9]. In particular, this work presents a fine analysis of the physical mechanisms behind different impact outcomes, sometimes highlighting differences that can hardly be noticeable from the mere analysis of the final outcomes.

The first attempt to construct a global mapping of drop impact regimes on heated surfaces was proposed by Bernardin and co-workers [6]. This work, however, focuses on the temporal evolution of the drop morphology rather than on the final outcome, which is of greater importance in practical applications. Rein [1] proposed a qualitative impact regime map using the surface temperature and the impact Weber number as coordinates. However, transition boundaries between different impact regimes are not defined quantitatively.

The present work aims at proposing a classification of drop impact regimes on a heated surface, which is based on physical principles, but at the same time can be useful in practical applications. These regimes are then plotted on a two-dimensional map, where transition boundaries are defined quantitatively.

EXPERIMENTAL APPARATUS AND PROCEDURE

The experimental setup is schematically described in Figure 1. Drops of de-ionised water (Barnstead Easypure II) were released from a blunt hypodermic needle (gauge 21, i.d. 0.495 mm) and impacted on a polished aluminium surface electrically heated and kept at constant temperature by a PID controller.

Drop weight measurements made with a precision balance (Mettler Toledo MT100) allowed calculation of the drop diameter at equilibrium, $D_0 = \sqrt[3]{6m/\pi\rho}$: the average value, calculated over 50 samples, was 3.09 ± 0.1 mm. The drop equilibrium radius, $D_0/2$, was therefore smaller than the capillary length, $a = \sqrt{\sigma/\rho g}$ (2.48 mm), which is indicative of the competition between surface forces and gravity: thus, surface forces prevail ensuring that the equilibrium shape of drops is spherical.

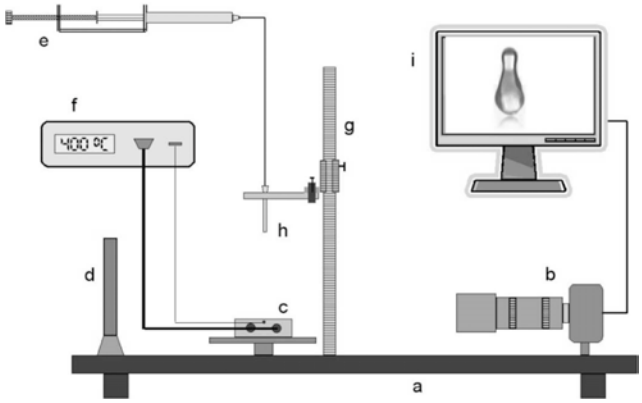

Figure 1: Schematic of the experimental setup: (a) optical breadboard (b) high-speed camera (c) heated aluminium block (d) LED backlight (e) drop dispensing system (f) temperature controller (g) height gauge (h) needle (i) computer.

Adjusting the position of the dispensing needle with a digital height gauge allowed changing the impact velocity hence the impact Weber number, $We = \rho D_0 u^2 / \sigma$, which expresses the competition between kinetic energy and surface energy. For falling heights smaller than 15 cm, the impact velocity is almost identical to the theoretical free fall velocity, $u = \sqrt{2g(H - D_0)}$ [11], so that the Weber number can be calculated as:

$$We = \frac{\rho D_0 u^2}{\sigma} = \frac{2\rho g D_0 (H - D_0)}{\sigma} \qquad (1)$$

In the present work, the impact Weber number ranged between 7 and 160.

The impacts of single drops were recorded using a high-speed CMOS camera (Mikrotron MC1310) at the rate of 1000 frames per second. The camera was horizontally aligned with the impact surface in order to measure the bouncing height of the drop with precision. Back-to-front illumination was provided by a LED light source equipped with light diffuser (ThorLabs).

For each set of experimental parameters (i.e., surface temperature and Weber number), the impact experiment was repeated five times for the sake of statistical analysis.

Figure 2: Typical outcome of drop impact on a surface at a temperature below the boiling point of the liquid (T = 100°C, We = 100): the drop is deposited on the surface and convection is the main heat transfer mode.

RESULTS

Morphology of impact regimes

For temperatures of the impact surface below the boiling point of water, the only active heat transfer mode is convection. This does not significantly affect the impact morphology as compared with homo-thermal impact (Figure 2). Thus, the impact morphology depends only on the fluid and surface properties, and on the impact velocity.

When the surface temperature is above the boiling point, vapour bubbles created on the hot surface rise by buoyancy and burst on the free surface of the drop, scattering a great number of satellite droplets (Figure 3).

The intensity of secondary atomisation may vary depending on the surface temperature or the impact Weber number (compare, e.g., the two cases in Figure 3). The size distribution of secondary droplets is not uniform, but bi-modal, with smaller droplets created by bubbles bursting on the liquid free surface with a bag-breakup mechanism [10], and bigger droplets created by free-surface instabilities. Secondary atomisation depends much on the surface properties, and in particular on its thermal effusivity [11].

For high temperatures (T > 350°C in the case of water on polished aluminium), two outcomes are possible: drop rebound (Figure 4), for low Weber numbers (We < 100), and drop splashing (Figure 5) for higher Weber numbers.

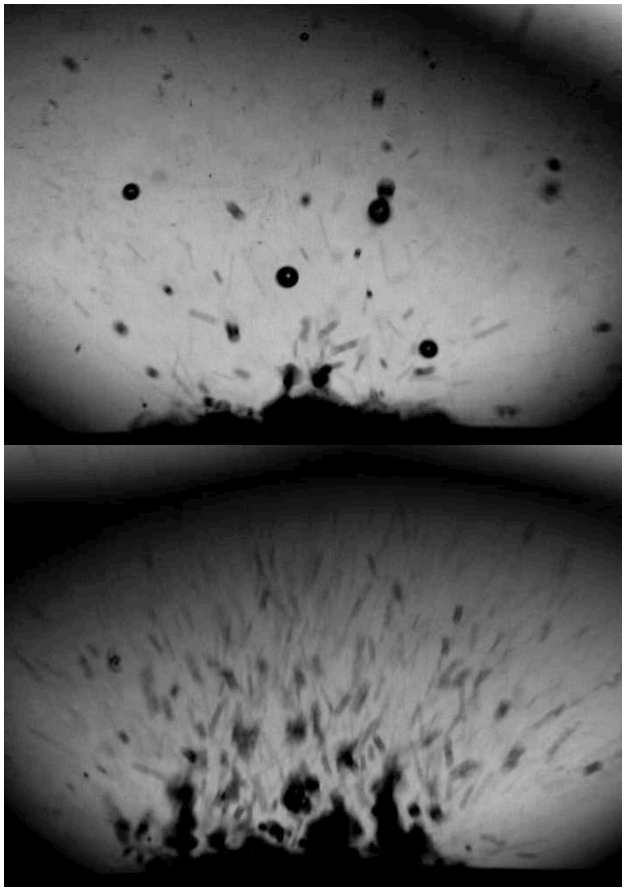

Figure 3: Typical outcome of drop impact on a surface at a temperature above the boiling point of the liquid (top: T = 150°C, We = 40; bottom: T = 150°C, We = 100): the drop ejects minuscule satellite droplets (secondary atomisation).

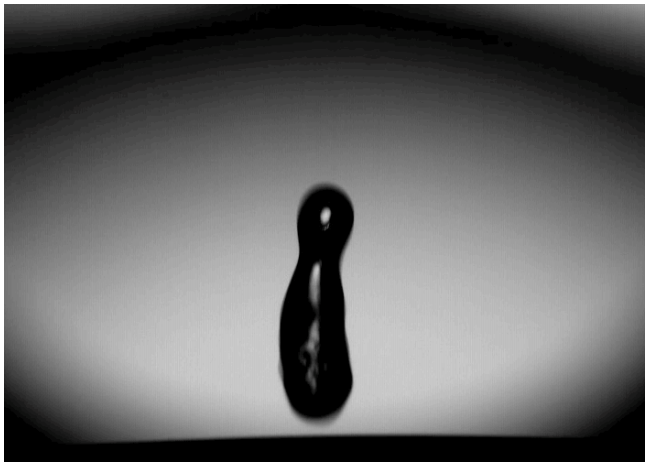

Figure 4: Typical outcome of drop impact on a surface at a temperature above the dynamic Leidenfrost point and low Weber numbers (T = 400°C, We = 40): the drop bounces on the surface without secondary atomisation.

Drop rebound occurs because at high temperatures (i.e., well above the Leidenfrost point [3],[12]) a vapour film forms between the liquid and the surface immediately upon impact. This vapour film acts as a lubricant layer, reducing energy dissipation during drop spreading and recoil. Therefore at the end of retraction there is still some kinetic energy available for rebound. This regime can be associated to the film boiling heat transfer mode, characterised by a stable vapour layer, which prevents any contact between the liquid and the surface.

For temperatures below 350 °C, one can observe two additional mixed regimes: rebound with secondary atomisation (Figure 6), and splashing with secondary atomisation (Figure 7).

These regimes are characterised by an unstable vapour film between the drop and the impact surface. This allows local contact between the liquid and the hot surface, where vapour bubbles can grow and generate secondary atomisation as they burst on the free surface of the drop. Unlike secondary atomisation shown in Figure 3, which occurs with the nucleate boiling heat transfer regime, these two regimes occur with transition boiling.

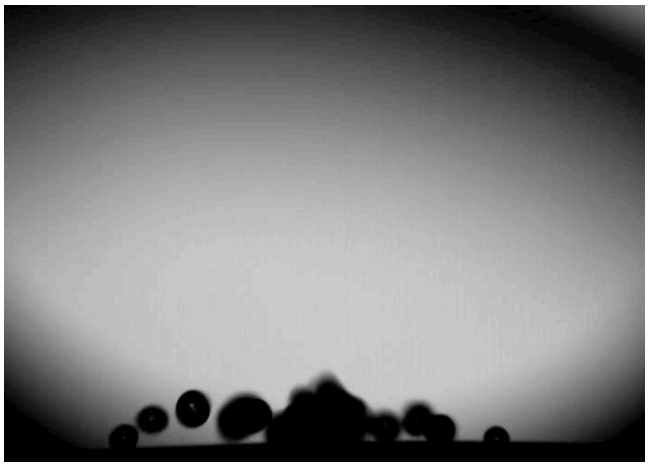

Figure 5: Typical outcome of drop impact on a surface at a temperature above the dynamic Leidenfrost point and High Weber number (T = 400°C, We = 100): the drop breaks down into smaller droplets (splashing).

Figure 6: Typical outcome of drop impact on a surface at a temperature below the dynamic Leidenfrost point and low Weber numbers (T = 250°C, We = 40): the drop bounces and simultaneously scatters secondary droplets.

Impact regime map

The occurrence of impact regimes described in the previous section can be visualised graphically on a two-dimensional map, which is shown in Figure 8, and whose coordinates are temperature and the reference Weber number at ambient conditions (i.e., with the fluid properties at ambient temperature).

Whilst the map is valid specifically for water drops on polished aluminium, it can also be representative of other systems, at least qualitatively.

The boundary between the ***rebound*** and ***rebound with secondary atomisation*** regimes defines the so-called dynamic Leidenfrost temperature, i.e. the minimum temperature to observe dry rebound, without secondary atomisation. Yao and Cai [5] proposed the following empirical correlation for the dynamic Leidenfrost temperature as a function of the Weber number:

$$T_{LD} = T_S + 135.6We^{0.09} \quad (2)$$

where T_S is the saturation temperature of water.

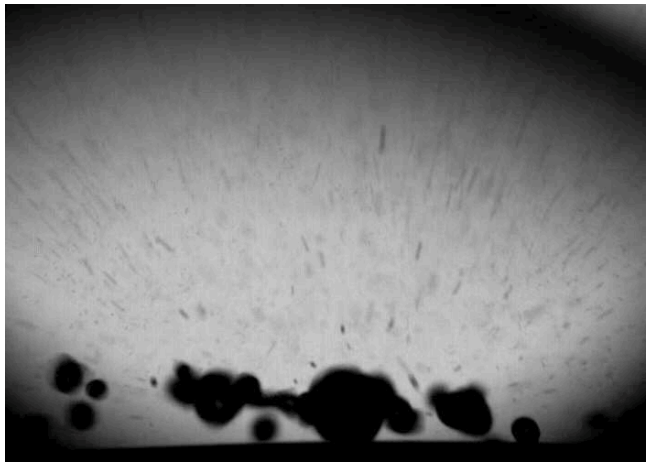

Figure 7: Typical outcome of drop impact on a surface at a temperature below the dynamic Leidenfrost point and high Weber numbers (T = 250°C, We = 100): the drop splashes and simultaneously scatters secondary droplets.

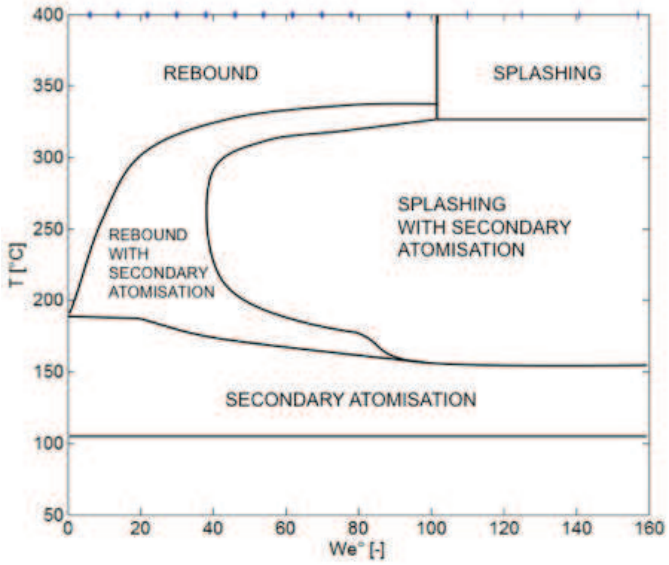

Figure 8: Impact regime map for water droplets (D ≈ 3mm) impacting on a heated, polished aluminium surface,

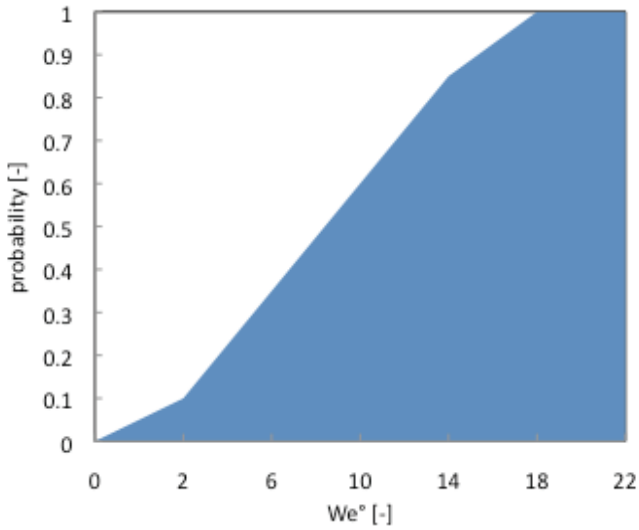

Figure 9: Probability of observing secondary atomisation during drop impact on a surface at 250°C, as a function of the Weber number.

However, Eq. (2) cannot predict the Leidenfrost temperature for a drop gently deposited on a hot surface (We $\rightarrow$ 0), which is significantly higher than T_S [12], therefore this transition is better characterised by correlations in the form:

$$T_{LD} = T_L + AWe^b \tag{3}$$

where T_L is the Leidenfrost temperature, and A and b empirical constants.

Another phenomenon that receives much attention is the onset of splashing, which is usually characterised in terms of the K dimensionless number [13][14].

$$K = WeOh^{-2/5} \tag{4}$$

where Oh is the Ohnesorge number:

$$Oh = \frac{\eta}{\sqrt{\sigma \rho D_0}} \tag{5}$$

It was found that splashing occurs at a constant value of the K number, for drops impacting on both dry and wetted surfaces [15]. Empirical correlations were also proposed to take into account the effects of surface roughness and of the relative liquid layer thickness [16].

Figure 8 shows that the splashing criterion based on the K number (K = const.) applies to impacts on heated surfaces in the Leidenfrost regime (i.e., with surface temperature above the dynamic Leidenfrost point), as well as to impacts on dry and wetted surfaces. Indeed, for assigned fluid properties and drop diameter, the condition K = const. reduces to We = const. This is no longer true in for the transition between mixed regimes (i.e., in the presence of secondary atomisation).

It is important to remark that the transition boundaries reported in Figure 8 are plotted as a function of the Weber number at ambient conditions, We°, therefore they may not reflect entirely the physical mechanisms of transitions.

In fact, the fluid properties, hence the dimensionless groups introduced above, change with the fluid temperature. For example, when the fluid temperature changes from 20°C to 99°C, viscosity reduces from 1 mPa·s to 0.28 mPa·s, and surface tension reduces from 72 mN/m to 58 mN/m; this causes the Weber number to increase by 20%, the Ohnesorge number to reduce by 70%, and the K number to increase by 90%.

Another important feature of these transitions is their probabilistic nature: if one repeats an impact experiment several times with experimental conditions (i.e., surface temperature and Weber number) close to a transition boundary between two different impact regimes on the map displayed in Figure 8, both outcomes will be observed.

For example, if one considers the transition between the "rebound" regime and the "rebound with secondary atomisation" regime, at a temperature of 250°C, one finds that the probability of observing secondary atomisation has the trend shown in Figure 9, i.e. the probability can be non-zero even before the transition boundary. Taking the derivative with respect to the Weber number of this probability function returns the probability density function of the boundary location, which therefore is not a line but is "smoothed" over a certain area.

CONCLUSION

Extensive drop impact experiments on a heated surface, covering a range of surface temperatures and Weber numbers, led to propose a classification of impact regimes based on the final outcome rather than on the details of the drop morphology during impact.

Such impact regimes were displayed on a quantitative two-dimensional map, which can be used to predict the drop impact outcome for assigned impact Weber number and surface temperature.

The transition boundary between the rebound and rebound with secondary atomisation regimes, as well as that between rebound and splashing, are consistent with results reported in the literature.

NOMENCLATURE

Symbol	Quantity	SI Unit
a	Capillary length	m
D_0	Drop diameter	m
g	Gravity	ms^{-2}
H	Falling height	m
K	K-number	-
L	Length, distance	m
m	Mass	kg
Oh	Ohnesorge number	-
T	Temperature	K
u	Velocity	ms^{-1}
We	Weber number	-

Greek:

η	Viscosity	Pa·s
ρ	Density	kgm^{-3}
σ	Surface tension	Nm^{-1}

Subscripts and superscripts

L	Leidenfrost
LD	Leidenfrost, dynamic
S	Saturation conditions
°	Ambient conditions

REFERENCES

[1] Rein, M., Interactions between drops and hot surfaces. In: M. Rein (ed.), ***Drop-surface interactions***, CISM Courses and Lectures No. 456, Springer, 2003.

[2] Watchers, L.H.J., Westerling, N.A.Y., ***The heat transfer from a hot wall to impinging water drops in the spheroidal state***, Chem. Eng. Sci., 1966, 21, pp. 1047- 1056.

[3] Gottfried, B.S., Lee, C.J., Bell, K.J., ***The Leidenfrost phenomenon: film boiling of liquid droplets on a flat plate***, Int. J. Heat Mass Transfer, 1966, 9, pp. 1167-1188.

[4] Pedersen, C.O., ***An experimental study of the dynamic behavior and heat transfer characteristics of water droplets impinging upon a heated surface***, Int. J. Heat Mass Transfer, 1970, 13, pp. 369-381.

[5] Yao, S.-C., Cai, K.Y., ***The dynamics and Leidenfrost temperature of drops impinging on a hot surface at small angles***, Experimental Thermal and Fluid Sci., 1988, 1, pp. 363-371.

[6] Bernardin, J.D., Clinton, J., Stebbins, A., Mudawar, I., ***Mapping of impact and heat transfer regimes of water drops impinging on a polished surface***, Int. J. Heat Mass Transfer, 1997, 40, pp. 247-267.

[7] Wang, A.-B., Lin, C.-H., Chen, C.-C., ***The critical temperature of dry impact for tiny droplet impinging on a heated surface***, Phys. Fluids, 2000, 12, pp. 1622-1625.

[8] Cossali, G.E., Marengo, M., Santini, M., ***Secondary atomization produced by single drop vertical impact onto heated surfaces***, Intern. Experimental thermal and fluid Science, 2005, 29, pp. 937-946.

[9] Fujimoto, H., Oku, Y., Ogihara, T., Takuda H., ***Hydrodynamics and boiling phenomena of water droplets impinging on hot solid***, International Journal of Multiphase Flow, 2010, 36, pp. 620-642.

[10] Azzopardi, B.J., ***Mechanisms of entrainment in annular two-phase flow***, 1983, UKAEA Report No. AERE R-11068.

[11] Cossali, G. E., Marengo, M., Santini, M., Fest, S., ***Effect of wall effusivity on thermally induced secondary atomization of single drop impacting onto a tilted surface***, ICLASS-06, Kyoto, Japan, 2006.

[12] Bernardin, J.D., Mudawar, I., ***The Leidenfrost Point: Experimental Study and Assessment of Existing Models***, ASME Journal of Heat Transfer, 1999, 121, pp. 894-903.

[13] Stow, C. D., Hadfield, M. G., ***An Experimental Investigation of Fluid Flow Resulting from the Impact of a Water Drop with an Unyielding Dry Surface***, Proc. R. Soc. Lond. A, 1981, 373, pp 419-441.

[14] Mundo, C. H., Sommerfeld, M., Tropea, C., ***Droplet-wall collisions: Experimental studies of the deformation and breakup process***, Int. J. Multiphase Flow 1995, 21, pp. 151-173.

[15] Yarin, A.L., ***Drop impact dynamics: splashing, Spreading, receding, bouncing***, Annu. Rev. Fluid Mech., 2006, 38, pp. 159-192.

[16] Cossali, G.E., Coghe, A., Marengo, M., ***The impact of a single drop on a wetted solid surface***, Exp. Fluids, 1997, 22, pp. 463-472.

OSCILLATING DROPLET EVAPORATION MODELLING FOR SPRAY COMBUSTION SIMULATION

Gianpietro Elvio COSSALI [C], Simona TONINI

Industrial Engineering Department, University of Bergamo, Viale Marconi 5, 24044 Dalmine, Italy
[C] Corresponding author: cossali@unibg.it

ABSTRACT
The vapour and gas phase conservation equations are analytically solved in a spheroidal coordinate systems, yielding the drop surface vapour flux under steady-state conditions, for oblate and prolate drops. The drop evaporation rate can be defined as function of drop spheroid shape and drop surface. The solution is easily implementable to the case of prolate/oblate oscillating drops, under quasi-steady assumption, which is found to be valid under the range of operating conditions typical of spray combustion applications.

INTRODUCTION

The majority of liquid spray numerical models requires information on the behaviour of an individual liquid drop in a gaseous flow [1]. Simplified models for predicting the drop phenomena in a spray (aerodynamic forces, evaporation, collision, break-up) have been developed through analytic, experimental, and numerical studies of individual liquid drops. These models usually assume a spherical shape for the liquid drop; for example the modelling of drop evaporation in most commercial CFD code for spray numerical simulations is generally based on this assumption [2]. On the other hand, a spray consists of liquid drops that undergo significant shape deformations while interacting with the carrier phase [3]. More generally, dispersed fluid particles (bubbles and drops, away from walls) can deform based on the interaction of surface tension and the fluid-dynamic stresses on the particle surface [4]. The surface tension forces will always drive a free particle towards a spherical shape, whereas initial conditions and/or fluid-dynamic forces are the primary sources of non-sphericity.

Examining the deformation response, three competing effects are found responsible of drop deformation [1]. The first one is a convective effect in the gas phase which tends to generate oblate drops. The second one is a convective effect in the liquid phase, which induces the deformation towards the prolate shape. The third one is a combined effect of gas-phase viscous and convective forces; this is considered important in large Ohnesorge number cases and tends to cause dimpled shapes [1].

The drop deformation could have significant effects on inter-phase transfer phenomenon, thus resulting in some modifications in the existing correlations valid for spherical drops [3]. The numerical treatment of this effect should take into account the continuously evolving interface that is very closely coupled to the heat and mass transfer occurring in the drop. Previous studies concluded that the dynamics of the drop deformation is basically unaffected by vaporization, however, the evaporation rates (per unit area) are greater for deformed drops [5].

Several studies available in the literature found that heat and mass transfer between liquid particles and the surrounding gas can be enhanced by drop oscillations [6, 7]. Particle oscillation can be achieved by a variety of methods, including acoustic oscillation, electric field oscillation for charged particles, and magnetic field oscillation for magnetic particles [6].

Furthermore, drop-gas interaction activates many drop oscillation modes and actually no drop in a gaseous stream can be steadily spherical. Haywood et al. [8] show that circulation inside the drop is responsible for the strong damping and promotes the formation of prolate shapes for drops. They also found that effect of liquid viscosity and finite amplitude oscillation reduces the drop oscillation frequencies up to 25% of the theoretical natural frequency predicted by Lamb [9]. Moreover, the results from [3] show that the mass flux varies along the surface of the deformed drop, due to modifications of the isotherms near the interface.

Drop oscillations can become important in atomization systems, where the liquid is first disintegrated into small ligaments, which then oscillate towards the attainment of an equilibrium spherical shape. If these ligaments/drops are exposed to a hot gas then the heat and mass transfer could be affected by oscillations. The rate of evaporation of an oscillating drop varies in time, but it is always greater than or equal to the rate of evaporation of the equivalent spherical drop [5].

Mashayek [3] suggested a correction in the evaporation rate of a deformed drop, derived from the results obtained by numerical simulations. The model, valid for surface deformation up to 10% of the drop radius, predicts that the rate of evaporation increases with the increase of the amplitude of the surface deformation and varies significantly along the surface of the drop. The same author in [10] proposed an application of the correction to the case of free oscillating drops, showing that the increase in the evaporation rate results to be proportional to the square of the surface disturbance amplitude and larger for higher oscillating modes [10].

Since the early work of Lamb [8], drop oscillation was the subject of many investigations, and the open literature is rich of works on this important phenomenon. Linear theory was widely used to obtain results for small amplitude oscillation, perturbation theory and non-linear analysis were used to extend the results to moderate and large amplitude oscillation and effect of viscosity was shown to quickly damp the highest modes, then living only the oblate-prolate mode to survive and, among many other results, it was observed that drops, which are released from an initially

two-lobed configuration spend less time in prolate form than in oblate one [11].

The necessity to include such complex behaviour in spray numerical simulations, prompts the continuous request of relatively simple sub-models for predicting the inter-phase phenomena taking place during the spray evolution. The present work proposes a rather easy-to-implement analytical expression of the instantaneous evaporation rate from oblate and prolate spheroid liquid drops and a possible application to the calculation of evaporation enhancement in oscillating drops. The derivation of the mathematical model is briefly presented in the following section, followed by the description of the model application to oscillating drops. Finally the main conclusions are briefly summarised.

MATHEMATICAL MODEL

Specie transport equations

For a liquid drop made of a single component floating in a gaseous atmosphere, the specie conservation equations can be written as [12]:

$$\rho U_j \nabla_j \chi_\alpha = \nabla_j \left(\rho D_v \nabla_j \chi_\alpha \right) \tag{1}$$

where $\alpha = v, g$ refers to the vapour and gaseous phases respectively, while $\chi_\alpha = \dfrac{\rho_\alpha}{\rho}$ is the mass fraction.

The boundary conditions (B.C.) set to constant values the vapour mass fraction at drop surface $\left(\chi_{v,s}\right)$ and at infinite distance from the drop $\left(\chi_{v,\infty}\right)$.

Integrating equations (1), the specie fluxes are calculated as:

$$\gamma_\alpha = \rho U_j \chi_\alpha - \rho D_v \nabla_j \chi_\alpha \tag{2}$$

with the first term representing the Stefan flow component [12] and the second being the diffusive component.

Evaporation rate of spheroid drop

To find an analytical solution for spheroidal drops, equation (1) must be written in a proper system of coordinates, and the natural choice are spheroidal coordinates, that for the oblate and prolate cases are defined as follows:

Oblate	Prolate
$x = a\cosh\xi \sin\theta\cos\varphi$	$x = a\sinh\xi \sin\theta\cos\varphi$
$y = a\cosh\xi \sin\theta\sin\varphi$	$y = a\sinh\xi \sin\theta\sin\varphi$
$z = a\sinh\xi\cos\theta$	$z = a\cosh\xi\cos\theta$

In these coordinate systems, the spheroid surface equation is simply $\xi = \xi_0$ and the B.C. are then:

$$\chi_v\left(\xi_0, \theta, \varphi\right) = \chi_{v,s} \qquad \chi_v\left(\infty, \theta, \varphi\right) = \chi_{v,\infty} \tag{3}$$

A steady state analytical solution of the balance equations (1) and B.C. (3) exists under the form:

Oblate: $\chi_v = 1 - \left(1 - \chi_{v,s}\right)\left(\dfrac{1-\chi_{v,\infty}}{1-\chi_{v,s}}\right)^{\frac{\arctan\left(e^{\xi}\right) - \arctan\left(e^{\xi_0}\right)}{\frac{\pi}{2} - \arctan\left(e^{\xi_0}\right)}}$

Prolate: $\chi_v = 1 - \left(1 - \chi_{v,s}\right)\left(\dfrac{1-\chi_{v,\infty}}{1-\chi_{v,s}}\right)^{1 - \frac{\ln\left(e^{\xi}+1\right) - \ln\left(e^{\xi}-1\right)}{\ln\left(e^{\xi_0}+1\right) - \ln\left(e^{\xi_0}-1\right)}}$

From these solutions, the evaporation rate can be easily calculated by integrating equation (2) over the drop surface, yielding, in non-dimensional form:

$$\hat{m}_{ev} = \frac{m_{ev}}{4\pi R_0 \rho D_v} = C\left(\varepsilon\right) \ln \frac{1-\chi_{v,\infty}}{1-\chi_{v,s}} \tag{4}$$

where the parameter ε is defined as:

$$\varepsilon = \frac{a_z}{a_r}$$

and a_z and a_r are respectively the axial and radial spheroid axes, see Figure 1 for reference.

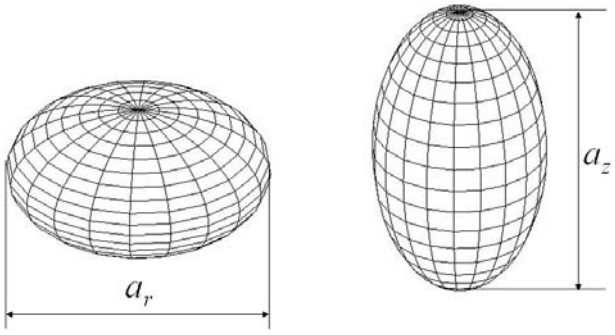

Figure 1. Oblate (left) and prolate (right) spheroids and definition of axial (a_z) and radial (a_r) spheroid axes.

The parameter $C\left(\varepsilon\right)$ in equation (4) is defined as follows:

$$C\left(\varepsilon\right) = \begin{cases} \dfrac{\sqrt{1-\varepsilon^2}}{\varepsilon^{1/3}\left(\pi - 2\arctan\sqrt{\dfrac{1+\varepsilon}{1-\varepsilon}}\right)} & , \varepsilon < 1, \text{ Oblate} \\ \dfrac{\sqrt{\varepsilon^2-1}}{\varepsilon^{1/3}\left[\ln\left(\sqrt{\dfrac{\varepsilon+1}{\varepsilon-1}}+1\right) - \ln\left(\sqrt{\dfrac{\varepsilon+1}{\varepsilon-1}}-1\right)\right]} & , \varepsilon > 1, \text{ Prolate} \end{cases}$$

and $C = 1$ for a sphere $\left(\varepsilon = 1\right)$.

It is of a certain interest to evaluate the surface of a spheroid having the same volume of a sphere with radius R_0. Defining with β the ratio between the spheroid surface and the surface of an isovolumic sphere, it is easy to show that a one-to-one relation exists between the parameters ε and β:

$$\beta\left(\varepsilon\right) = \frac{A_{spheroid}}{A_{sphere}} = \frac{1}{2\varepsilon^{2/3}} \begin{cases} 1 + \dfrac{\varepsilon^2 \ln\dfrac{1+\sqrt{1-\varepsilon^2}}{\varepsilon}}{\sqrt{1-\varepsilon^2}} & \text{Oblate} \\ 1 + \dfrac{\varepsilon^2 \arctan\sqrt{\varepsilon^2-1}}{\sqrt{\varepsilon^2-1}} & \text{Prolate} \end{cases}$$

The factor $C\left(\varepsilon\right)$ can then be related to the spheroid surface as in Figure 2. As expected, the evaporation rate of a spheroid is always larger than that of a sphere having the same volume, although that of a prolate spheroid is always

larger than that of an oblate spheroid having both the same volume and the same surface.

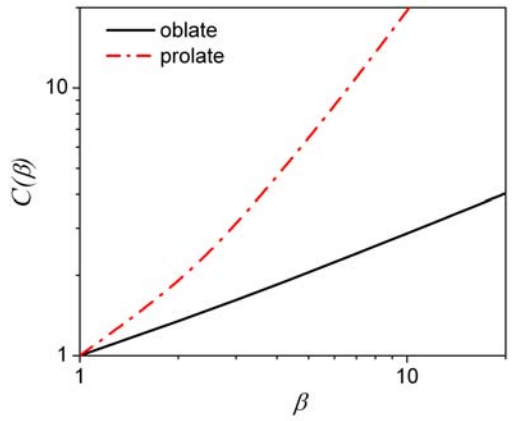

Figure 2: Non-dimensional evaporation factor as function of the spheroid surface ratio.

Oscillating drop

The oscillation modes of a liquid drop in gaseous environment can be described (for small oscillation amplitude) by the generalized Lamb equation [9].

$$\omega_n^2 = \frac{n(n+1)(n-1)(n+2)}{(n+1)\rho_{in} + n\rho_{out}} \frac{\sigma}{R_0^3} \tag{5}$$

where ρ_{in} and ρ_{out} refer to the densities of the inner and outer fluids respectively, and the index n refers to the various oscillation modes: $n=0$ stands for a pure expansion (typical for bubbles), $n=1$ refers to translation mode, without a corresponding frequency, $n=2$ refers to oblate-prolate mode, and finally $n>2$ describes more complex modes. It should be noticed that the linear theory predicts for the mode $n=2$ a shape that is only approximately oblate or prolate spheroid, although the difference for small oscillation amplitude (i.e. for the range where the linear theory holds) is almost negligible.

For a liquid drop oscillating in a gaseous environment $\rho_{in} \gg \rho_{out}$, then the Lamb equation (3) yields:

$$\omega_n^2 = \frac{n(n+1)(n-1)\sigma}{\rho_l R_0^3}$$

Considering the effect of liquid viscosity, according to [2], the higher modes are quickly damped and the mode $n=2$ is the only long lasting ones. The oscillation frequency then becomes:

$$\omega_n = \sqrt{\frac{8\sigma}{\rho_l R_0^3}}$$

As above mentioned, non linear theory [11] yields more accurate (but more complex) results, among others the fact that the time spent by a drop in the oblate shape is larger than the time spent in a prolate form, but this fact will not be considered here.

The drop shape variation of an axis-symmetric oscillating drop can be expressed through a perturbation parameter $a_n(t) = a_n^0 e^{i\varpi_n t}$ by the equation [13]:

$$r(\theta) = r_0^* \left(1 + \sum_{n=2} \frac{a_n(t)}{2n+1} P_n(\cos\theta)\right)$$

where $P_n(x)$ are the Legendre polynomials. The drop surface can then be calculated as a function of this parameter and to the third order in a_n it assumes the following expression [13]:

$$A_{spheroid} = 4\pi R_0^2 \left(1 + \sum_{n=2} \frac{(n+1)(n+2)}{2n+1} a_n^2 - \frac{1}{3} \sum_{\substack{m,n,l=2 \\ i+j+k=2}}^{m,n,l=\infty} \begin{pmatrix} 3 \\ i\ j\ k \end{pmatrix} \langle m,n,l \rangle a_m^i a_n^j a_l^k \right)$$

where:

$$\langle m,n,l \rangle = \int_0^\pi P_m(\cos\theta) P_n(\cos\theta) P_l(\cos\theta) \sin\theta d\theta$$

Considering only the mode $n=2$, at the second order accuracy, the dependence of the parameter β on time assumes the following expression:

$$\beta = \frac{A_{spheroid}}{A_{sphere}} = 1 + \frac{2}{5} a_{n,0}^2 \sin^2(\omega_2 t) \tag{6}$$

Quasi steady-state assumption

To apply the above found analytical solution for the evaporation rate (4), valid for steady conditions, to an oscillating drop, a quasi steady-state assumption is necessary. Such assumption may hold when the characteristic time scale of the oscillation process is much larger than that of the evaporation one. While the first one is easy to be defined as the inverse of the oscillation frequency:

$$t_{oscill} \approx \sqrt{\frac{\rho_l R_0^3}{\sigma}}$$

the evaporation time scale is not easily defined.

Evaporation is an overlapping of a diffusive phenomenon (driven by the coefficient D_v) and a convective one (i.e. the Stefan flow, driven by a characteristic velocity $U_0 = \frac{m_{ev}}{\beta 4\pi R_o^2 \rho} = \frac{\hat{m}_{ev}}{\beta} \frac{D_v}{R_0}$). From these two parameters and the drop size, three characteristic, but not independent, times (convective, diffusive and convective-diffusive) can be defined:

$$t_{conv} \approx \frac{R_0}{U_0}$$

$$t_{diff} \approx \frac{R_o^2}{D_v}$$

$$t_{cd} \approx \frac{D_v}{U_0^2} = \frac{t_{conv}^2}{t_{diff}}$$

Rearranging the previous definitions, the following correlation can be obtained:

$$t_{conv} \approx \frac{\beta R_0^2}{\hat{m}_{ev} D_v} = \frac{\beta t_{diff}}{\hat{m}_{ev}}$$

$$t_{cd} \approx \frac{\beta^2 R_0^2}{\hat{m}_{ev}^2 D_v} = \frac{\beta^2 t_{diff}}{\hat{m}_{ev}^2}$$

The quasi steady state assumption may be acceptable when:

$$t_{evap} \ll t_{oscill}$$

where t_{evap} may be one of the three above mentioned characteristic times. An inspection on the values of such characteristic times shows that the inequality may acceptably hold for small drops (few tenths of micron) in hot gaseous environment and for hydrocarbon drops. But it may be questionable for larger drops, for lower gas temperature and for water drops.

Under this assumption, the above developed model can be applied to an oscillating drop. The total evaporated mass from a single oscillating drop during an oscillating period (assuming the time spent in prolate state equal to that spent in oblate state) can be calculated as:

$$M = \int_0^T m_{ev}\,dt = m_{ev,sphere}\int_0^T C\left(\beta(t)\right)dt = \\ = m_{ev,sphere}\left[\int_0^{T/2} C_{oblate}\left(\beta(t)\right)dt + \int_0^{T/2} C_{prolate}\left(\beta(t)\right)dt\right] \quad (7)$$

where $\beta(t)$ is given by equation (6).

PRELIMINARY RESULTS

Considering a single oscillating drop, the temporal evolution of instantaneous non-dimensional evaporation rate ($m_{ev}/m_{ev,spehere}$) can be related to the deformation status, as reported in Figure 3. The non-dimensional evaporation rate is always greater than 1, confirming that for an oscillating liquid drop the evaporation rate is always higher than that of the corresponding non-oscillating isovolumic spherical drop. Furthermore, when the drop is in the prolate state, its evaporation rate reaches the highest values.

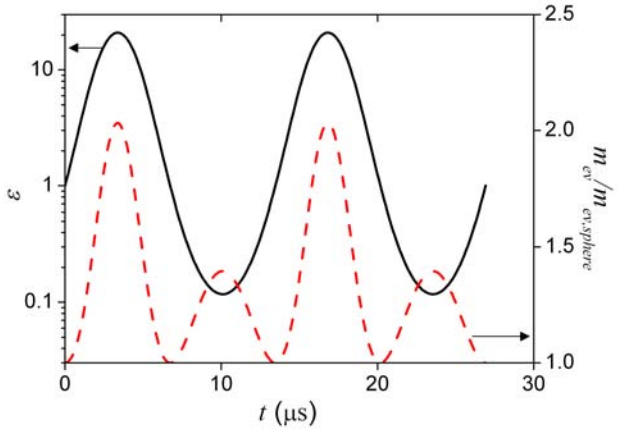

Figure 3: Temporal evolution of spheroid eccentricity (ε) and non-dimensional instantaneous evaporation rate ($m_{ev}/m_{ev,spehere}$) for a R_0 = 10 μm iso-octane drop.

The comparison between the evaporated mass from an oscillating drop and that from a spherical iso-volumic drop can be performed, for different values of the "excess" energy (defined as the kinetic energy associated to the oscillation modes), that can be easily related to the maximum drop surface area. The percentage difference in the evaporated mass, defined as:

$$\Delta ev\% = \frac{M - m_{ev,sphere}T}{m_{ev,sphere}T}\,100$$

where M is calculated from equation (7) can be related to the percentage excess area $\left(\Delta\beta_{\max}\% = \left(\beta_{\max} - 1\right)100\right)$ and Figure 4 reports the results for a 10 μm iso-octane drop in a hot (700°C) gaseous environment. These preliminary results show that a simple correction for evaporation from oscillating drops could be implemented by assuming an approximate linear relation between the two parameters, where the proportionality coefficient may depend on drop and environment characteristics.

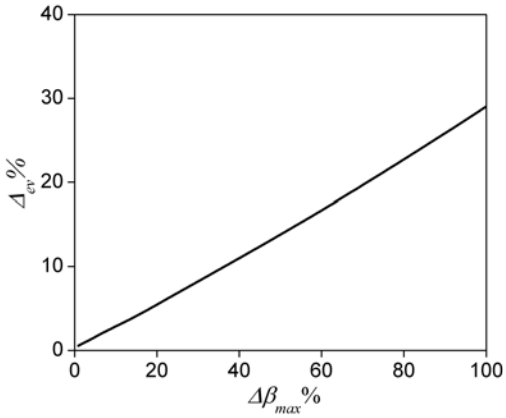

Figure 4: Percentage relative difference of evaporated mass as function of the maximum drop surface area ratio (in percentage).

CONCLUSIONS

Vapour and gas transport equations are analytically solved in oblate and prolate spheroidal coordinate systems, yielding the vapour distribution around a spheroidal drop and the surface flux under steady state conditions.

The drop evaporation rate can be defined as function of drop spheroidal shape and drop surface. Compared with iso-volumic spherical drop, spheroidal drops yield larger evaporation rate, with the oblate shape yielding a lower evaporation rate then the prolate one with the same surface area.

Application to oscillating drop is possible under quasi steady-state assumption, that may hold for small hydrocarbon drops in hot gaseous environment, yielding rather easy-to-implement corrections to the standard spherical case.

ACKNOWLEDGMENTS

This work was partially financed by the Project V.I.R.Berg. co-financed by Regione Lombardia.

NOMENCLATURE

Greek symbols

α	Species index	-
β	Surface ratio	-
Δ	Relative difference	-
ε	Spheroid eccentricity	-
ρ	Density	kg/m^3
ξ	Mass fraction	-
γ	Specie flux	kg/m^{2}s
σ	Surface tension	kg/s^2
ζ, ϕ, φ	Spheroid coordinates	-

ω	Oscillation frequency	1/s
Roman symbols		
a	Perturbation parameter	-
a_r, a_z	Radial and axial spheroid axes	m
C	Evaporation rate factor	
D_v	Diffusivity	m^2/s
M	Mass	kg
m_{ev}	Evaporation rate	kg/s
n	Oscillation mode	-
P_n	Legendre polynomials	-
R	Drop radius	m
t	Time	s
T	Oscillating period	s
U	Velocity	m/s
x, y, z	Cartesian coordinates	-
Subscripts		
conv	Convective	-
diff	Diffusive	-
cd	convective-diffusive	-
evap	Evaporation	-
g	Gaseous	-
l	Liquid	-
oscil	Oscillation	-
0, s	Surface	-
v	Vapour	-
∞	Infinity	-
Superscripts		
$\wedge$	Non-dimensional	-

REFERENCES

[1] Helenbrook B.T., and Edwards C.F., *Quasi-steady deformation and drag of uncontaminated liquid drops*, *International journal of multiphase flow*, 2002, 28(10), pp: 1631-1657.

[2] Abramzon B., and Sirignano W.A., *Droplet vaporization model for spray combustion calculations*, *International journal of heat and mass transfer*, 1989, 32(9), pp: 1605-1618.

[3] Mashayek F., *Dynamics of evaporating drops. Part I: formulation and evaporation model*, *International journal of heat and mass transfer*, 2001, 44(8), pp: 1517-1526.

[4] Loth E., *Quasi-steady shape and drag of deformable bubbles and drops*, *International Journal of Multiphase Flow*, 2008, 34(6), pp: 523-546.

[5] Jeng S.M., and Deng Z., *Numerical simulation of deformed droplet dynamics and evaporation*, *Recent advances in spray combustion: Spray combustion measurements and model simulation.*, 1996, 2, pp: 305-328.

[6] Zhu J., Zheng F., Laucks M.L., and Davis E.J., *Mass transfer from an oscillating microsphere*, *Journal of colloid and interface science*, 2002, 249(2), pp: 351-358.

[7] Guan G., Zhu J., Xia S., Feng Z., and Davis E.J., *Simulation of mass transfer from an oscillating microdroplet*, *International journal of heat and mass transfer*, 2005, 48(9), pp: 1705-1715.

[8] Haywood R.J., Renksizbulut M., and Raithby G.D., *Transient deformation and evaporation of droplets at intermediate Reynolds numbers*, *International journal of heat and mass transfer*, 1994, 37(9), pp: 1401-1409.

[9] Lamb H., *Hydrodynamics*, 6th ed: Cambridge University Press, 1932.

[10] Mashayek F., *Dynamics of evaporating drops. Part II: free oscillations*, *International journal of heat and mass transfer*, 2001, 44(8), pp: 1527-1541.

[11] Basaran O., *Nonlinear oscillations of viscous liquid drops*, *Journal of Fluid Mechanics*, 1992, 241, pp: 169-198.

[12] Fuchs N.A., *Vaporisation and droplet growth in gaseous media*, London: Pergamon Press, 1959.

[13] Daidzic N., *Nonlinear droplet oscillations and evaporation in ultrasonic levitator*, *Erlangen University*, 1995.

WATER DROP IMPACT INTO A DEEP POOL: INFLUENCE OF THE LIQUID POOL TEMPERATURE

Stephanie Fest-Santini[1,C], Manfredo Guilizzoni[2], Maurizio Santini[1], Gianpietro Elvio Cossali[1]

[1] Department of Industrial Engineering, University of Bergamo, viale Marconi 5, 24044 Dalmine (BG), Italy
[2] Department of Energy, Politecnico di Milano, via Lambruschini 4, 20156 Milan, Italy
[C]Corresponding author: stephanie.fest-santini@unibg.it

ABSTRACT
The cratering regime with its manifold characteristics like micro-entrapments, primary entrapment which could lead to the trampoline phenomena, vortex rings, micro-jetting and thick jets is chosen as a study case for the influence of liquid pool temperature on the drop impact into a deep pool. Characteristic drop impact which features micro-entrapments, primary entrapment and trampoline phenomena are selected as a test cases. Pool temperatures between 20 and 40 °C are studied, whereby the droplet temperature is kept constant. The experimental results are compared with simulations obtained using the *interFoam* solver of the OpenFOAM® open source CFD package.

INTRODUCTION

The impact of a drop onto a deep liquid layer produces an amazing amount of different phenomena, like coalescence, splashing, bubble entrapment, crater formation, vortex rings, etc. Comprehensive reviews can be found in [1-3]. Several classifications of the drop impact regimes are proposed by many authors of the occurring phenomena based on dimensionless numbers, like Weber and Froude, using thermophysical parameters of impacting drops. The influence of viscosity and/or surface tension on impact outcomes is usually studied altering both drop and pool liquid [4], so that pool and impacting drop offer equal properties. It has been observed [5] that variations of bath temperature can influence the vortex penetration depth, especially, for impacting water drop into water pool. This is likely due to the change of viscosity due to its strong temperature-dependency. However, thermophysical properties of the liquid pool do not define dimensionless numbers and consequently do not influence the classification or description of impact outcomes, but may affect the impact phenomena.

This paper is aimed to study experimentally and numerically the influence of the liquid pool temperature on the crater evolution and its surrounding phenomena like micro-entrapment and trampoline phenomena. The work consists of two conceptual parts. The first one is aimed to verify if CFD solvers may be able to reproduce the complex phenomena which are observed during deep pool impacts, and particularly the effect of temperature on the crater shape and evolution. The *interFoam* solver of the OpenFOAM® CFD package [6] is selected for the numerical simulations since promising results are obtained in the field of drop impact onto liquid films and pools [7-12]. The second aspect of the investigation is related to the influence of liquid pool temperature on impact phenomena observed in classical experiments. The complementary numerical, easily accessible information, like velocity or pressure field, may help to understand physically the observed outcome.

EXPERIMENTAL METHOD

Drop impact experiments are carried out at the Department of Industrial Engineering, University of Bergamo, whereby the high-speed visualisation techniques with continuous back-light illumination is used to observe droplet impacts into a pool of the same liquid. Millimetric water droplets are generated by an on-demand droplet generator. The drops fall by gravity onto a deep (i.e. depth much larger of drop diameter) water pool crossing an optical trigger device that produce a TTL pulse. This pulse triggers the acquisition of the high speed camera.

Special accuracy is required in the alignment of the water level in the pool and camera position in relation to the water level. Otherwise, refractive and alignment distortions or black stripes within the images due to liquid interfacial phenomena with the pool walls (meniscus) appear. It is worth noting that the dimension of black stripes depends also from the thickness of the pool walls and can only be avoided by a correct and constant water level in the pool. Thereby, the pool is connected to a level water container mounted on a micrometric stage. The micrometric stage allows a precise regulation of the water level, whereby the large surface area of the level pool guaranties its constancy during experiments. Additionally, the camera is mounted on a tilting, rotating and movable platform, so that its lens axis can be independently adjusted.

To increase the degree of observation within the droplet [10], the distance between impact point and camera-facing pool wall is reduced, so that wall effects should be considered for later times after impact.

The recorded images are post-processed to obtain the crater interface as function of time. Hereby, the algorithm comprises background subtraction, contrast enhancement, image cleaning and edge detection using the Laplacian of Gaussian (LoG) method and feature detection. The contrast enhancement including lower and high upper limits of the intensities setting and the intensification factor are adapted to the detectable information. Each experimental investigation is analysed by extracting the following information: (a) impact velocity, diameter and sphericity using the frames before drop impact, (b) crater interface contour as function of time and (c) the quantity and contour of entrapments as function of time.

The temperature of the bath is adapted in the range between about 20 and 40 °C with the aim to vary its thermophysical properties (table 1). Each impact event is repeated three times for statistical reasons at equal pool liquid temperature.

Table 1: Thermophysical properties of water in the applied temperature range

T [°C]	ρ [kg/m^3]	η [kg/(m s)]	σ [N/m]
20 ± 0.5	999.21	$1002.0 \cdot 10^{-6}$	$72.44 \cdot 10^{-3}$
40 ± 0.5	992.22	$653.2 \cdot 10^{-6}$	$69.53 \cdot 10^{-3}$

NUMERICAL METHOD

Hardware and software

The simulations are performed at the Department of Engineering, Politecnico Milano, on a notebook PC with a Intel Core i7-740QM CPU (4 cores @ 1.73 GHz, 8 threads) with 6 GB RAM and on a desktop PC with a Intel Core i7-990X CPU (6 cores @ 3.46 GHz, 12 threads) with 24 GB RAM, both with Ubuntu Linux as the operating system.

Concerning the used software, *interFoam* is a two-phase isothermal finite volume solver which uses a Volume of Fluid (VOF) [13] approach modified with the introduction of an additional term in the volume fraction equation, to obtain interface compression by means of a tuneable parameter. The continuum surface force (CSF) model [14] is used to include surface tension at the interface. A detailed descriptions of *interFoam* and of the underlying models can be found in [7, 8, 15 - 19]. During preliminary tests, OpenFOAM® versions 1.7.1 and 2.1.x gave practically identical results concerning the crater shape, while significant differences were found (despite the use of the same mesh, schemes and settings) for the entrapped bubble, whose existence and dynamics are much better captured by version 1.7.1. Further investigation is at present being carried out to understand this strange behaviour. For this work, version 2.1.x is used.

Model and settings

No modifications were done to the solver for the present simulations and the discretization schemes and settings from the official *damBreak* tutorial case are in general used. The domain is modeled and meshed with the *blockMesh* OpenFOAM® utility. Domain dimensions are 0.02 x 0.02 x 0.015 m in 3D cases and 0.02 x 0.02 m x 5° in the 2D axisymmetric cases. In all cases the boundary conditions are defined as follows:

- wall boundary for the front, back, bottom and external sides of the pool;
- open boundary for the top of the domain ("atmosphere");
- axial symmetry for the axis in the axisymmetric case;
- symmetry plane for the internal "side" of the mid-pool in the 3D case.

Water drops with different diameters, velocities and temperatures were used, in all cases with dry air at the drop temperature as a surrounding medium. Both fluids are assumed Newtonian and incompressible and the flow laminar. Water regions are initialized using the *setFields* and *funkySetFields* OpenFOAM® utilities.

The solver is let free to adapt the time step to keep the Courant number under 0.5. Such requirement is the limit for 2D simulations using the scheme implemented in OpenFOAM® and should be reduced to under 0.3 for 3D cases [17, 18]. The problem is partially addressed by the introduction of some volume fraction sub-cycles, because obviously a very low value of the Courant number would imply very small time steps and consequently extremely long simulations.

Preliminary tests

During the experiments, the distance between the impact point and the camera-facing pool wall has to be quite small to allow a very detailed observation of the phenomena happening within the droplet. The negative counterpart is that wall effects on the crater evolution can only be neglected for the initial stage of drop impact. Moving to the numerical world, the consequence is that a 2D axisymmetrical simulation (with all its benefits in terms of required resources and simulation time) may not give adequate results. The first performed test is therefore a comparison between a 3D simulation and a corresponding 2D axisymmetrical simulation, to evaluate up to which time they show good agreement. Figure 1 shows the results. As for all the cases described in the paper, the drop surface is extracted as the isosurface for volume fraction equal to 0.5. No significant difference appears if other values in the range 0.1-0.9 are used. Cross-sections of such isosurface are then extracted when needed, as in this case. The hypothesis of axisymmetry appears to be acceptable for the initial part of the impact, which is the most interesting for this work.

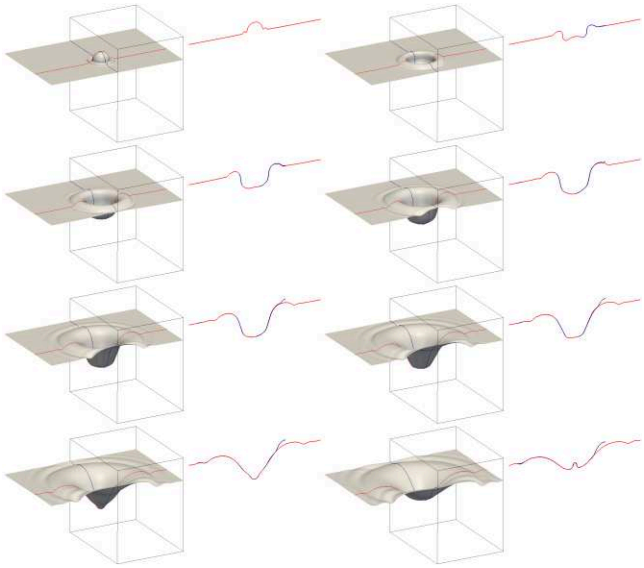

Figure 1: results of the 3D numerical simulation, where two orthogonal cross-sections are evidenced to verify the axisymmetry hypothesis. Time = 1.5 :3 : 22.5 ms (row-wise) from the beginning of the simulation. Mesh: 160 x 160 x 160 cells.

Then, a suitable 2D axisymmetric mesh is searched for. The selected mesh, which will be used as the base mesh for the simulation presented hereafter, is purely structured and composed by hexahedral and wedge elements, with grading in both direction. It is sketched in figure 2 (to increase

visibility, in the figure the mesh resolution is reduced 5 times in each direction with respect to the real one).

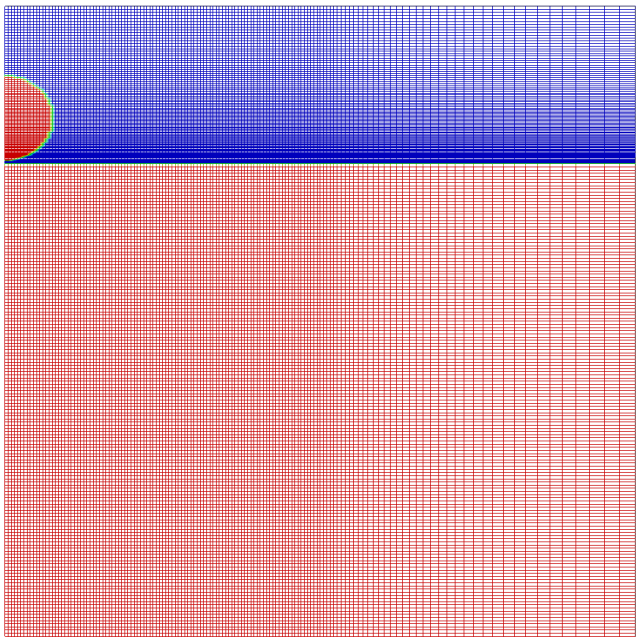

Figure 2: Reference mesh structure for the axisymmetric cases, and initial setting of the volume fraction (red = water, blue = air). Mesh resolution has been decreased 5 times with respect to the real one to improve visibility. The real mesh is 700 x 950 x 1 (665000) cells.

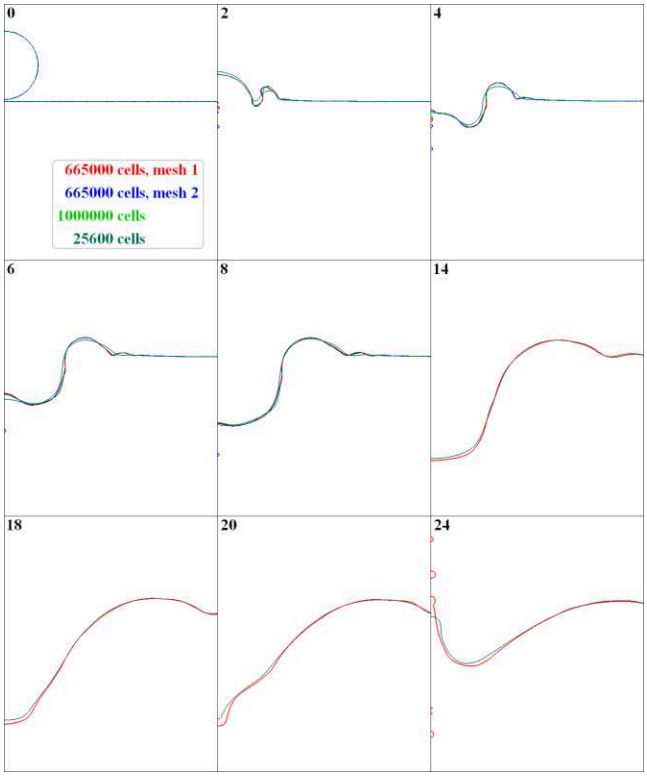

Figure 3: Mesh independence of the numerical crater evolution. Time [ms] from the beginning of the simulation is indicated in the upper left corner of each frame.

Mesh independence of the results is then analyzed on a test case characterized by drop diameter 3.5 mm, drop speed 1.14 m/s, drop temperature 26 °C. Good mesh independence is found, even if the finest structures (bubbles, micro-jetting) are lost with the roughest mesh. Figure 3 shows the results. Finally, some tests are performed to evaluate if the "default" value of the Courant number may be adequate. The discretization schemes proposed in the official *damBreak* tutorial seems to be already a good choice, apart from the temporal discretization which is only first order. Therefore, a test is also performed by replacing it with a Crank-Nicholson "0.5" scheme. Slight improvement is found for some details, but in general no significant difference may be noticed (figure 4), while simulation time with the modified settings is more than 4 times longer (and over one order of magnitude longer for some time steps).

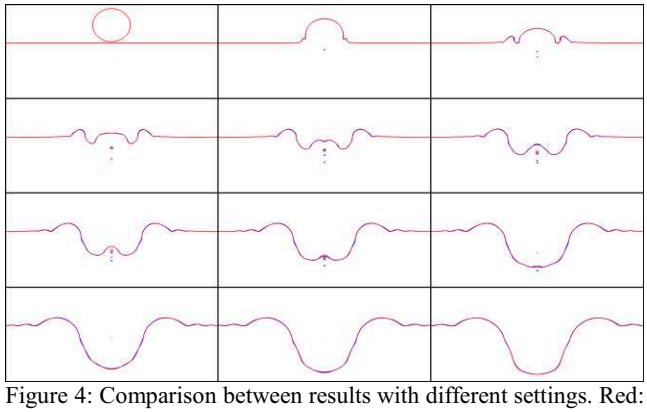

Figure 4: Comparison between results with different settings. Red: Euler time discretization, Co = 0.5, 3 volume fraction sub-cycles; blue: Crank Nicholson "0.5" time discretization, Co = 0.05, 5 volume fraction sub-cycles. Time: 0: 0.8 : 8.8 ms from the beginning of the simulation.

RESULTS

As test cases to verify the performance of the CFD solvers, selected mesh and settings, the impact of a drop having diameter 2.95 mm and impact velocity 1.05 m/s is chosen. The drop temperature is fixed to 24 C± 1°K and the pool temperature amounts 24°C and 40°C, respectively. Figure 5 and figure 6 shows the results superposed to experimental acquisitions for $T_{pool} = 24$ °C and $T_{pool} = 40$ °C, respectively. Both test cases do not feature the trampoline phenomena, since *interFoam* is a two-phase solver and cannot distinguish between drop water and pool water after contact. As reported in table 1, the dynamic viscosity of pool water differs of about 30% for the two test cases. This leads to slightly larger depth and faster recoil at higher pool temperatures in the experiments. But, this influence is within the experimental repetition fluctuation. The entrapment of initial air bubbles - produced by rupture of the thin air sheet which remains entrapped between impacting drop and pool - seems to be unaffected by the variation of bath temperature. Their carrying deep within the pool is influenced by the vortex formation which is visible coloring the impacting drop [20]. This also explains their often chaotic motion (compare figure 8). The entrapment of micro bubbles too is further detailed in figure 8, where the image intensity is adapted on the visibility of entrapments.

From the numerical point of view, it may be stated that the solver is able to reproduce quite well the experimental crater shape and evolution, even if some delay in the latter is present, with consequent imperfect overlapping of the results. Part of such disagreement may be also due to the

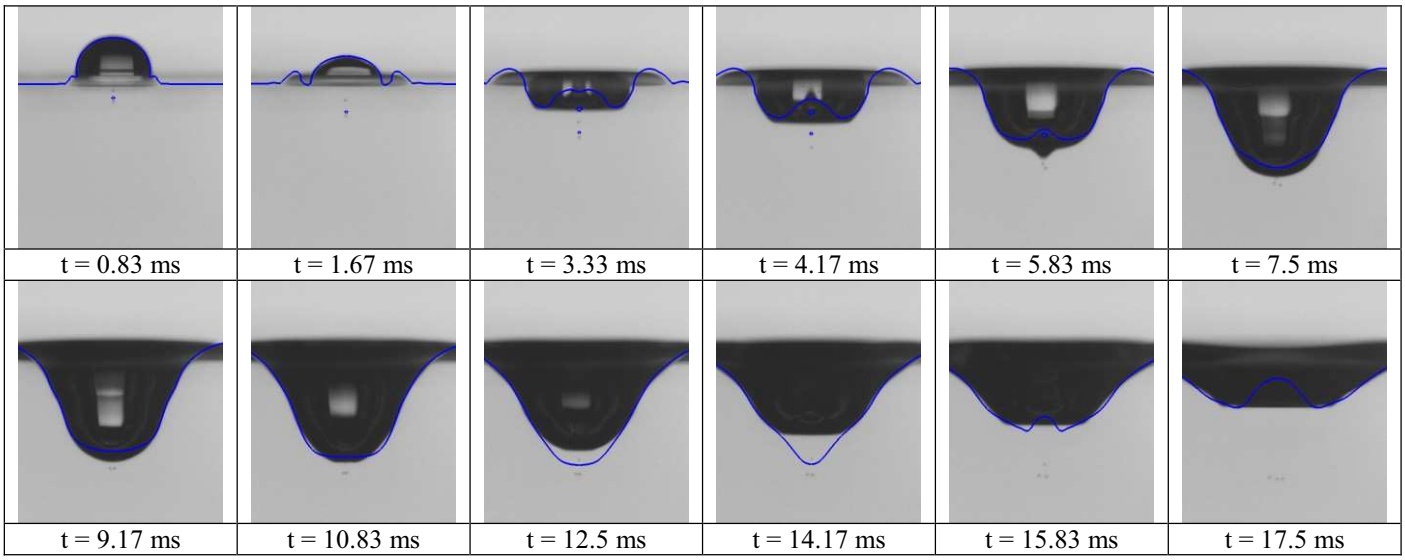

Figure 5: Superposition of the numerical crater profile to the experimental acquisition for D = 2.95 mm, V = 1.05 m/s and T_{pool} = 24°C

fact that the simulation outputs are saved every 10^{-4} s, which does not allow perfect temporal superposition with experimental frames.

As regards the dynamics of the entrapped bubbles (apart from the aforementioned comment about different results between 1.7.1 and 2.1.x OpenFOAM® versions), the immediate coalescence when they are reached by the crater is inherent in the VOF method [21], so bubble displacement by direct contact with the crater interface cannot be observed in simulation. Their lower sinking speed compared to the experimental one may on the contrary be due to the fact that in 2D axisymmetric simulations they are perfectly on the axis, so they are influenced by the center of the crater which is the last part of the latter to move downward. In experiments they may be slightly shifted from the axis, thus experiencing an earlier and stronger downward thrust.

It should be mentioned that altering the liquid properties during the numerical studies, both drop water and pool water properties are changed (again due to the fact that *interFoam* is a two-phase isothermal solver) in difference to experimental approach. Concerning specifically the temperature influence, it can be seen from figure 5 and figure 6 how the first part of the evolution is almost perfectly superposed. Then at the higher temperature the crater reaches a larger depth and recoils faster and with a smaller central cone. A similar, but less pronounced, tendency is also observed experimentally.

The difference of surface temperature of impacting drop and liquid pool could lead to the trampoline phenomena. A series of capillary waves propagates up the impacting drop and converges at its top, pinching off a smaller secondary drop. As shown in detail in figure 7, the secondary drop falls onto the bottom of the crater and is then ejected by the receding crater. This ejection affects the crater shape. Main differences are observed at about 6 ms and 7°ms (expanding crater) and again at about 12 ms and 13 ms (receding crater) after drop impact. Increased surface temperature facilitates the trampoline phenomena, but it seems to be not the only requirement (compare figure 6). Bisighini [23] has reported that a prolate shape of the impacting drop may cause the trampoline phenomena. This observation could not be confirmed as main condition. The ejection of a secondary drop has been observed for prolate as well as for oblate drop shapes and the liquid pool temperature was always higher than 30°C.

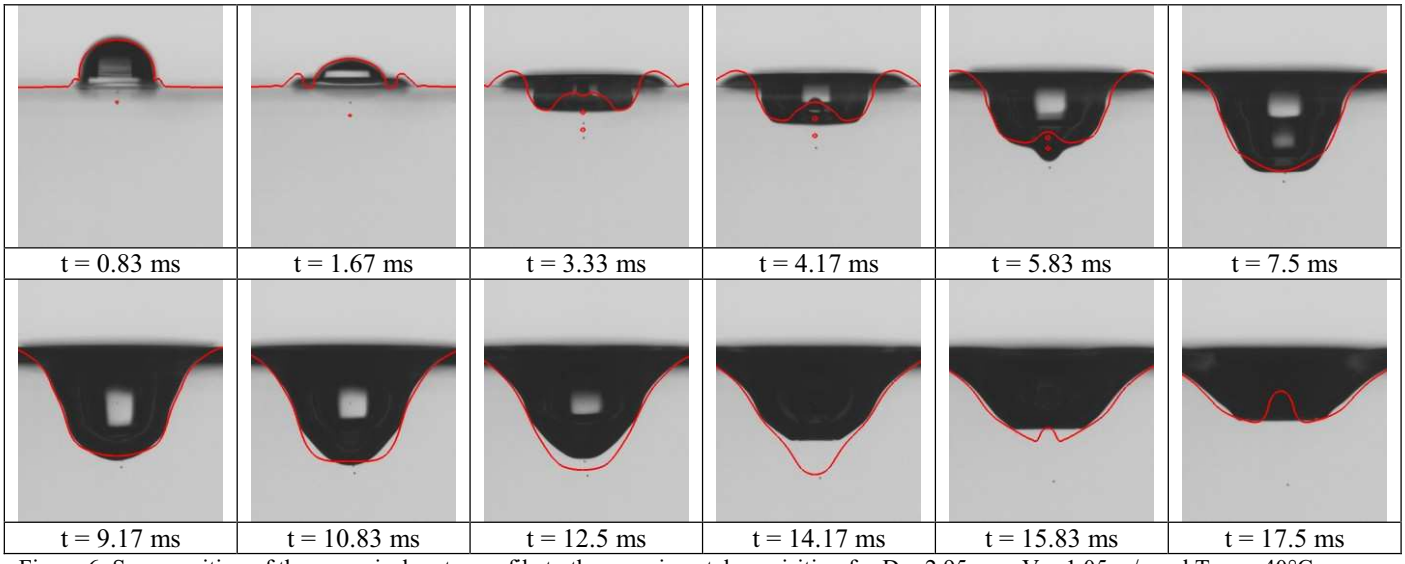

Figure 6: Superposition of the numerical crater profile to the experimental acquisition for D = 2.95 mm, V = 1.05 m/s and T_{pool} = 40°C

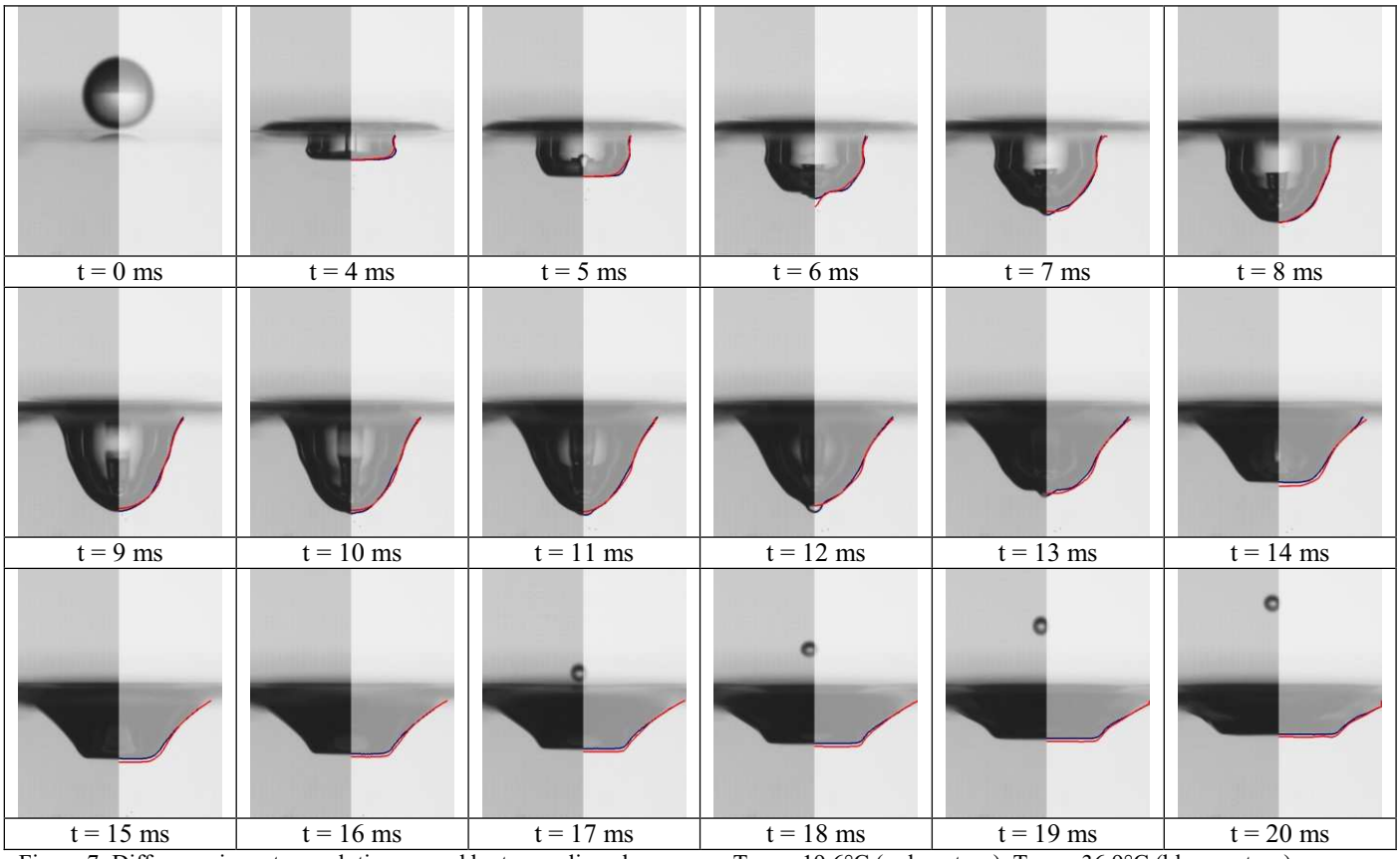

Figure 7: Difference in crater evolution caused by trampoline phenomena: T_{pool} = 19.6°C (red contour), T_{pool} = 36.9°C (blue contour)

Figure 8 shows the evolution of micro-bubbles entrapment of drop impact shown in figure 5. The intensity profile is adapted with the focus on the visualization of entrapped micro-bubbles (figure 8, left side) and afterwards the images are binarized (figure 8, right side). As shown in figure 5 and figure 6, a secondary drop is formed within the crater in analogy to the trampoline phenomena. This drop is not ejected by the receding crater; it is disgorged by the still expanding crater at times of about 6 ms after impact. The crater itself is characterized to that time by a tip. The secondary drop is carried deep inside the pool liquid as shown in figure 9 for times later than 12.5 ms after impact. At earlier time, the disgorged drop is covered by the expanding crater and is not visible in the projected view of the high speed image. The disgorging of the secondary droplet is observed for all tested liquid pool temperatures. It seems to be that the secondary droplet within the crater is always formed and is either disgorged or ejected and the crater shape is governed by one or the other phenomena (see figure 7). The probability of secondary droplet ejection increases with increasing liquid pool temperature which corresponds to an increased difference in dynamic viscosity between impacting drop and pool water.

The test simulations do not predict a secondary drop formation, so that neither the ejection upwards (trampoline) nor the disgorging downward in the pool liquid could be numerically described.

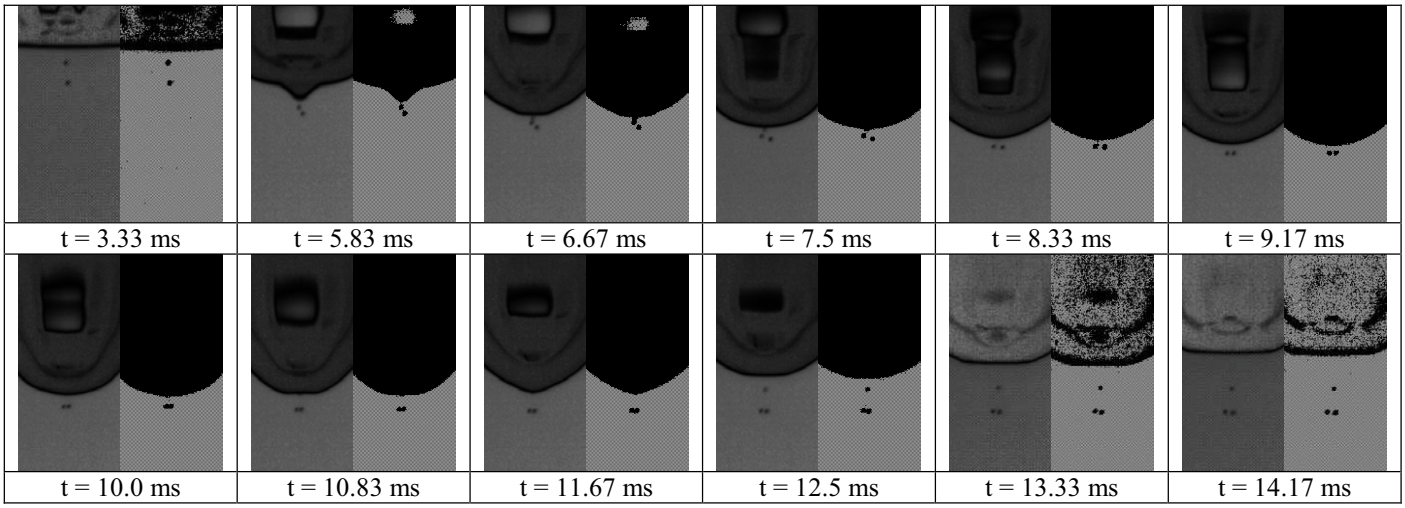

Figure 8: Additional bubble entrapment caused by entrapped drop in crater for D = 2.95 mm, V = 1.05 m/s and T_{pool} = 24°C (impact conditions of figure 5): intensity adapted (left side of each image) and binary images (right side of each image)

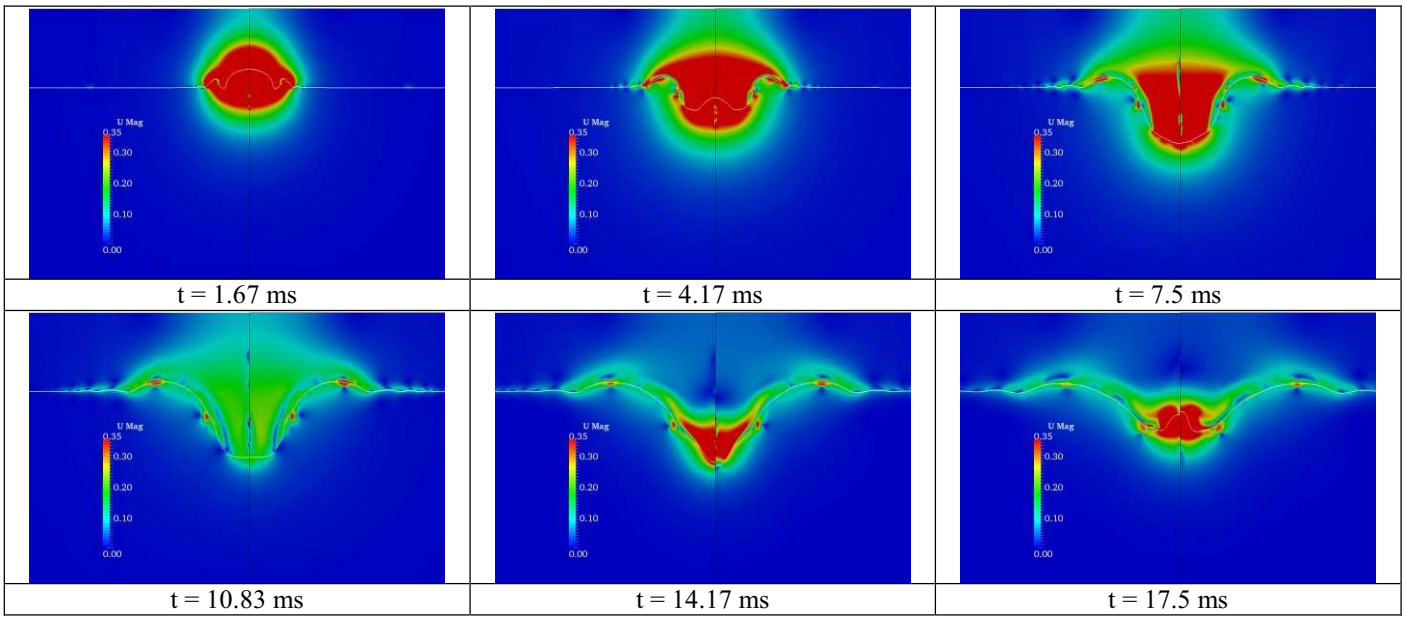

Figure 9: Velocity magnitude calculated by numerical simulation for two test cases for D = 2.95 mm, V = 1.05 m/s and T_{pool} = 24°C (left side of each image) and T_{pool} = 40°C (right side of each image)

Figure 9 shows the comparison between the two numerical test cases T_{pool} = 24 °C and T_{pool} = 40 °C in terms of velocity magnitude. The color scale of the velocity magnitudes is limited between 0 m/s and 0.35 m/s for visibility reasons and velocity profiles below the crater are very similar for both test cases due to the similar crater shape.

A peculiar phenomenon is that of the fast upward jets which can be observed when the crater reaches and incorporates the entrapped bubbles. Such behavior is quite strange and it may be an effect of numerical problems, but it may also have a physical meaning, being related to the capillary pressure within the bubbles. Their radius is between $5e^{-5}$ and $1e^{-4}$ m, resulting in a capillary pressure predicted by the Laplace-Young equation (for spherical bubbles) between 2900 Pa and 1400 Pa (in perfect agreement with the simulated values which are between 3000 Pa and 1400 Pa). When the bubbles coalesce into the crater, the above air is projected upwards.

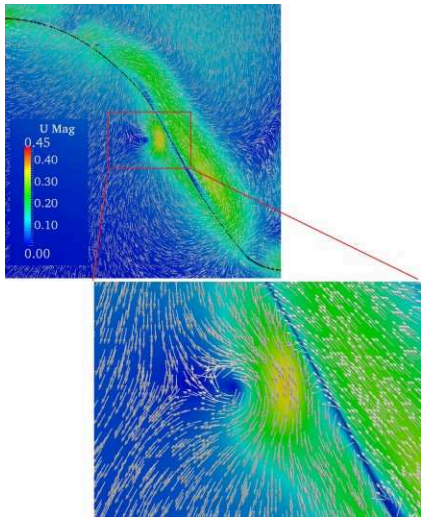

Figure 10: Numerical predicted vortex structure that develops along the crater side (T_{pool} = 24 °C, t = 12.5 ms)

Another interesting phenomenon which could be numerically predicted is the vortex that develops along the crater side (figure 10). This vortex structure at the crater side was visualized dying the impacting drop [20].

CONCLUSION

A comparative study of experimentally and numerically obtained drop impacts into deep pools in the cratering regime aimed to identify the dependence of liquid pool temperature on drop impact phenomena was performed.

The crater shape is influenced by the upward (ejected) or downward (disgorging) motion of secondary drop formed within the crater within the expanding phase. Ejection is facilitates at higher pool liquid temperature.

The *interFoam* solver seems to be a suitable tool for the simulation of drop impacts into pools. Phenomena like trampoline (ejection) or disgorging of the secondary drop and the corresponding influence on the crater shape could not be predicted as they require the utilization of a multi-phase solver.

REFERENCES

[1] Rein, M., *Phenomena of liquid drop impact on solid and liquid surfaces*, Fluid Dyn Res, 1993, 12, pp. 61-93.

[2] Rodriguez, F., Mesler, R., *The Penetration of Drop-Formed Vortex Rings into Pools of Liquid*, J Colloid and Interface Sci, 1988, 121, pp. 121-129.

[3] Yarin, A.L., *Drop impact dynamics: splashing, spreading, receding, bouncing,* Annu Rev Fluid Mech, 2006, 38, pp. 159–192.

[4] Deng, Q., Anilkumar, A.V., Wang, T,G., *The role of viscosity and surface tension in bubble entrapment during drop impact onto a deep liquid pool*, J Fluid Mech, 2007, 578, pp. 119–138.

[5] Peck, B., Sigurdson, L, *The three-dimensional structure of an impacting water drop*, Phys Fluids 1994, 6, pp. 564-576.

[6] *OpenFOAM®*, The open source CFD toolbox, website: http://www.openfoam.com/, accessed March 2012.

[7] Costa A.B., Graham Cooks R., *Simulated splashes: Elucidating the mechanism of desorption electrospray ionization mass spectrometry*, Chemical Physics Letters, 2008, 464, 1-8.

[8] Berberovic E., van Hinsberg N.P., Jakirlic S., Roisman I.V., Tropea C., *Drop impact onto a liquid layer of finite thickness: Dynamics of the cavity evolution*, Physical Review E 79, 036306, 2009.

[9] Roisman I.V., Berberovic E., Jakirlic S., Tropea C., *Dynamics of two-phase flows induced by drop collisions*, Proceedings of the 7th International Conference on Multiphase Flow (ICMF), Tampa (FL,USA), 2010.

[10] Fest-Santini S., Guilizzoni M., Santini M., Cossali G.E., *Drop impacts in pools: a comparison between high speed imaging and numerical simulations*, Proceedings of the Droplet Impact Phenomena & Spray Investigations (DIPSI) Workshop 2011, Dalmine (Italy).

[11] Santini M., Fest-Santini S., Guilizzoni M., Cossali G.E., *Drop impact onto a deep pool: study of the crater evolution*, Proceedings of the 24th European Conference on Liquid Atomization and Spray Systems (ILASS - Europe 2011), Estoril (Portugal), 2011.

[12] Berberovic, E., *Investigation of Free-surface Flow Associated with Drop Impact: Numerical Simulations and Theoretical Modeling*, Ph.D. Thesis, TU Darmstadt, 2010

method for the dynamics of free boundaries, Journal of Computational Physics, 1981, 39, 201-225.

[14] Brackbill J.U., Khote D.B, Zemach C., *A Continuum Method for Modeling Surface Tension*, Journal of Computational Physics, 1992, 100, 335-354.

[15] *The OpenFOAM® User Guide*, available online at website: http://www.openfoam.org/docs/, accessed July 2012.

[16] Weller H.G., Tabor G., Jasak H., Fureby C., *A tensorial approach to computational continuum mechanics using object-oriented techniques*, Computer in Physics, 1998, 12(6), 620-631.

[17] Jasak H., Weller H.G., *Interface-tracking capabilities of the InterGamma differencing scheme*, Technical Report, Imperial College of Science, Technology and Medicine, University of London, 1995.

[18] Gopala V.R., van Wachem B.G.M., *Volume of fluid methods for immiscible-fluid and free-surface flows*, Chemical Engineering Journal, 2008, 141, 204-221.

[19] Ferziger J.H., Peric M., Computational Methods for Fluid Dynamics, 3rd Ed., Springer, 2002.

[20] Santini, M., Fest-Santini, S., Cossali, G.E., *LDV characterization of the liquid velocity field underneath an impacting drop*, 16th Int. Symp. on Appl. Laser Techniques to Fluid Mechanics, Lisbon (Portugal), July, 2012.

[21] Nikolopoulos N., Nikas K.-S., Bergeles G., *A numerical investigation of central binary collision of droplets*, Computers & Fluids, 2009, 38, 1191-1202.

[22] Bisighini, A., *Single and double drop impact onto a deep and thick liquid layer*, Ph.D. Thesis, University of Bergamo, 2009.

DROP DEPOSITION AND LOW-SPEED IMPACT ON FLAT, CURVED AND MICROFINNED SOLID SURFACES: COMPARISON BETWEEN SIMULATIONS, MODELS AND EXPERIMENTS

Manfredo GUILIZZONI[1,C]

[1]Department of Energy, Politecnico di Milano - Via Lambruschini 4, 20156 Milan
[C]Corresponding author: manfredo.guilizzoni@polimi.it

ABSTRACT
The two-phase and multiphase incompressible solvers of the OpenFOAM® CFD package were used to simulate the shape, gentle deposition and low-speed impact of water drops on solid surfaces characterized by means of the contact angle. Smooth flat and curved surfaces and microfinned surfaces were used to benchmark such solvers by comparison with numerically-integrated analytical results, models and experimental results. The simulation were performed on single personal computers to verify what can be obtained with a conventional hardware, without using a cluster. The observed performances are satisfactory even if some problems were encountered.

INTRODUCTION

Numerical simulation is more and more used in many engineering fields and it has reached a high level of reliability for the analysis of complex problems, which up to a few years ago could only be investigated experimentally or by means of very simplified models. Nevertheless, it remains a "dangerous" instrument due to the ill-reposed trust it may give if incorrectly used [1] and there is still a need for further benchmark of simulation results, particularly in those field where simulation is "younger" or more difficult. Computational fluid dynamics (CFD) of multiphase flows is certainly one of the latter cases. Moreover, during the last years many studies were devoted to the development of new materials and surfaces with special characteristics, among which one of the most interesting features is hydrophobicity. Wettability analyses thus gained renewed importance. For the present work, comparisons between numerical, experimental and analytical results was therefore performed for some cases in the fields of drop deposition and low-speed impact onto solid surfaces, to verify the performances of the *interFoam* and *multiphaseInterFoam* solvers of the OpenFOAM® CFD package [2]. The code structure, implemented models and open source nature of OpenFOAM® makes it a very interesting and promising tool, and good results were obtained with it for various multiphase fluid dynamics problems [3–15]. They are mainly related to highly dynamic cases (e.g. drop impact onto liquid [3–8] and solid [9] surfaces), while very few studies [10] are devoted to static or low-speed scenarios. In this work some situations of the latter kind were investigated, with main focus on sessile and gently deposed drop. Smooth flat and curved surfaces and microfin surfaces were tested, by means of axisymmetric and 3D simulations run on structured meshes. A drop-onto-drop impact at 1.4 m/s was also tested.

NUMERICAL PROCEDURE AND INVESTIGATED CASES

Table 1 shows the details of the investigated cases. The *interFoam* solver of the OpenFOAM® open source CFD toolbox [2] was chosen because of its very promising characteristics (e.g. automatic interface tracking and mass conservation) [16–18] and because successful examples of use of *interFoam* in the fields of drop splashing and impact are reported in literature [3–9]. *interFoam* is a two-phase finite volume solver which uses a Volume of Fluid (VOF) [19] approach modified with the introduction of an additional term in the volume fraction equation, to obtain interface compression by means of a tunable parameter. The continuum surface force (CSF) model [20] is used to include surface tension at the interface. A detailed descriptions of *interFoam* and of the underlying models can be found in [3, 4, 16–18, 21]. For one of the simulations, the *multiphaseInterFoam* solver [15, 22] - which is an extension of *interFoam* - was also used. OpenFOAM® versions 1.7.1 and 2.1.x gave practically identical results for the performed simulations. No modifications were done to the solver and the discretization schemes and settings from the official *damBreak* tutorial case were used. The domain was modelled and meshed with the *blockMesh* OpenFOAM® utility. Non-flat domain floors (curved or microfinned) were modelled using Matlab® and in most cases the *snappyHexMesh* OpenFOAM® utility. Purely structured hexahedral meshes were created, apart from the cases where *snappyHexMesh* was used, as the snap of near-boundary cells to the boundary surface results in non-structured mesh regions. In one case (deposition on a microfin surface, case 3b) a home-made pre-processing utility for *blockMesh* was also tested. Domain and mesh dimensions are given in Tab. 1. In all cases the domain is opened on the top, where "open boundary" conditions were implemented. On the sides of the domain either symmetry conditions (axis or plane) or "zero gradient" wall boundary conditions were set for all variables. On the floor of the domain, which is the surface touched by the drops, boundary conditions implementing "constant contact angle" were set. As a first test, contact angle hysteresis (which could have been implemented using the built-in dynamical contact angle boundary condition or more sophisticated models [23, 24]) was neglected. Water drops at ambient temperature (20 °C) were used, with air as a surrounding medium. Both fuids were assumed Newtonian and incompressible and the flow laminar. Water regions were initialized using the *setFields* and *funkySetFields* OpenFOAM® utilities. The solver is let free to adapt the time step to keep the Courant number under 0.5. Such requirement is the limit for 2D simulations using the scheme implemented in OpenFOAM® and should be

reduced to under 0.3 for 3D cases [17, 18]. The problem is addressed by the introduction of some volume fraction sub-cycles. For some cases much lower Courant numbers may be a better solution, particularly to reduce spurious velocities, but this would imply very small time steps and consequently extremely long simulations. As for Newtonian fluids the viscosities of the phases do not intervene in the drop final equilibrium shape, for cases where the latter was the only interest they were increased 100 times with respect to their real values. This partially smooths out the oscillations and speeds-up the convergence to the final shape. For the same cases, the simulations were run until the drop shape visually did not change any more and the maximum speed within the domain was reduced under 0.01 m/s - a purely arbitrary choice, with no further analysis about real or spurious velocities apart from qualitative meaningfulness of the results (Figs. 1, 2). Concerning the used hardware, simulations were performed on a notebook PC with a Intel Core i7-740QM CPU (4 cores @ 1.73 GHz, 8 threads) with 6 GB RAM and on a desktop PC with a Intel Core i7-990X CPU (6 cores @ 3.46 GHz, 12 threads) with 24 GB RAM, both with Ubuntu Linux as the operating system.

Case	**Surface type**	**Drop speed [m/s]**	**2D / 3D simulation**	**Domain [mm] and number of cells**
Wetting drop	Smooth, flat	Sessile	2D axisym.	5x5, 62500, 250000, 1000000
Nonwetting drop	Smooth, flat	Sessile	2D axisym.	5x5, 62500
Drops on curved surface	Smooth, curved	Sessile	3D	5x11x10, 2140842
Drop on microfin surface	Microfin	Gently deposed (very low speed impact)	3D	case 1: 4x4x5, 2118150; case 2 and 3a: 10x5x4.23, 2911000; case 3b: 10x5x4.23, 3125000
Drop-onto-drop impact	Smooth, flat	1.4	2D axisym.	5x5, 62500

Table 1: Details of the investigated cases.

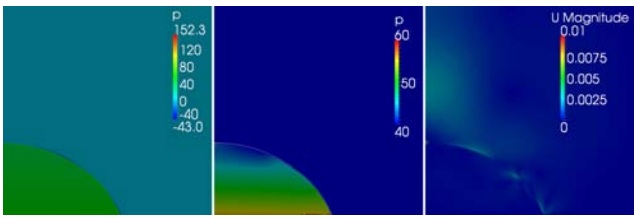

Figure 1: Wetting drop: pressure and velocity magnitude at "equilibrium".

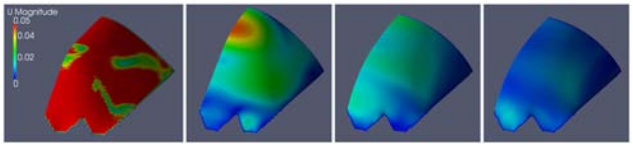

Figure 2: Deposition on the microfin brass surface: reduction of the velocities towards equilibrium (time = 100:10:130 ms).

EXPERIMENTAL SET-UP

The set-up available at the Multiphase Fluid dynamics Laboratory of the Department of Energy, Politecnico di Milano was used for the experimental validation of the results. It is located on an anti-vibrating optical bench (Newport, SA Series, 1.2 x 0.80 m) with a carrying structure in aluminium alloy. A high precision metering pump (Cole-Parmer Instrument Company, model AD74900) completed by suitable syringes and needles (Hamilton) allows to generate microlitre drops of controlled volume. The surfaces under investigation can be characterized, in terms of profile and roughness, by means of a "surface analyzer" (SM Sistemi di Misura s.r.l., model RT80). A 800 W lamp equipped with a diffuser provides the lighting necessary to the photographic and video acquisitions. Still images can be taken using a SLR digital camera Nikon D90 with a AFS 60mm F2.8 Macro lens, while a Canon DM-XM2 videocamera and a Nikon AW100 compact camera can be used to capture videos at 25, 120 and 240 fps. Detailed description of the experimental procedure for image processing, contact angle measurement and drop shape analysis can be found in [25] for flat and curved surfaces and in [26] for microfin surfaces.

WETTING DROP ON A FLAT SURFACE

The first investigated case was the sessile drop on a hydrophilic (contact angle 70°) ideal (chemically omogeneous, smooth, flat) solid surface. A 2D axisymmetric simulation was performed. The drop was initialized as a cylinder (height = 2 mm, diameter = 4 mm) using the *setFields* OpenFOAM® utility and let evolve towards its final equilibrium shape. In the given conditions, the latter may be described by the Laplace-Young equation which for the sessile drop case reads (ΔP_{apex} being the pressure jump at the drop apex, y axis centered in the drop apex and with downward direction):

$$\Delta P_{apex} + \left(\rho_{drop} - \rho_{\substack{surrounding\\fluid}}\right) g y = = \sigma_{LV}\left(\frac{1}{R_1} + \frac{1}{R_2}\right) \quad (1)$$

or in arc length coordinates (s,ϕ) [27]:

$$\frac{d\phi}{ds} = \frac{2}{R_{apex}} + \frac{\left(\rho_{drop} - \rho_{\substack{surrounding\\fluid}}\right) g}{\sigma_{LV}} y - \frac{sin\phi}{x} \quad (2)$$

where R_{apex} is the curvature radius at the drop apex.

Equation 2 may be easily integrated numerically so that comparison between such result and the output of numerical simulations can be performed. The latter should trivially reproduce the correct contact angle, which is set as a boundary condition, but also the Laplacian drop profile. As the method implemented in OpenFOAM® is a volume method and the shape and position of the interface is not explicitly tracked, such check is a validation of the model, to see if it is able to reproduce correct interface shapes. As already told, the simulations were run until the drop shape visually did not change any longer and the maximum speed within the domain reduced under 0.01 m/s. At that point, a cross-section of the calculated drop shape was extracted by the ParaView® postprocessor and saved as an image. For all the cases described in the paper, the drop surface was extracted as the isosurface for volume fraction equal to 0.5. No significant difference would in any case appear if other values in the range 0.1-0.9 should have been used. Cross-section of such isosurface were then extracted when needed, as in this case. The procedure for drop shape analyis described in [25, 26, 28] was then applied using such image instead of an experimental side-view picture of a drop. Figure 3 shows the results of the comparison. As it can be seen, the agreement both in the contact angle and in the drop profile is very good. This first investigated case will serve also as a basis for a following one, where another drop will be let fall on the sessile one analysed here.

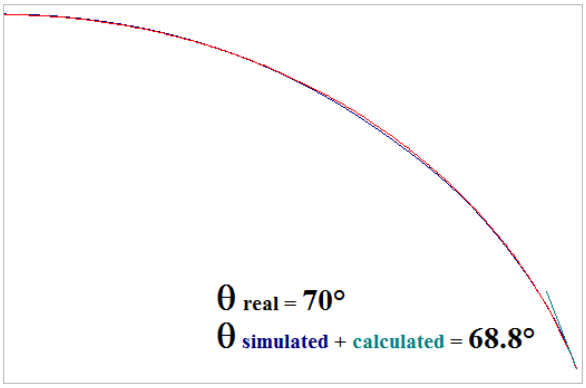

Figure 3: Comparison between the numerical and "analytical" (numerical integration of the Laplace-Young equation) results for the shape of a water drop on a hydrophilic surface.

Figure 4 shows the mesh dependence of the simulation results: it is evident how the drop evolution from the initial cylindrical shape to the final equilibrium shape is heavily dependent on the mesh at the beginning, while the final shape is correctly reproduced with all the three meshes.

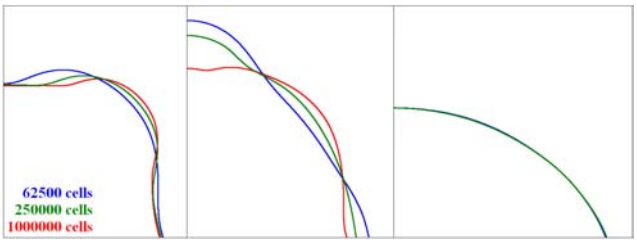

Figure 4: Wetting drop: mesh [in]dependence of the results (time = 10 ms, 20 ms, 200 ms).

NONWETTING DROP ON A FLAT SURFACE

The same kind of analysis was then performed for a drop on a hydrophobic surface (Fig. 5) The contact angle was modified into 120°, while all the other settings were left unaltered. Many side views of the numerical drop profile were extracted at different zoom levels, to investigate also the effect of the image resolution on the procedure for drop shape analysis. As it can be seen in Fig. 6, the latter as almost no influence and the agreement between *interFoam* results and the Laplacian drop profile is very good in this case too.

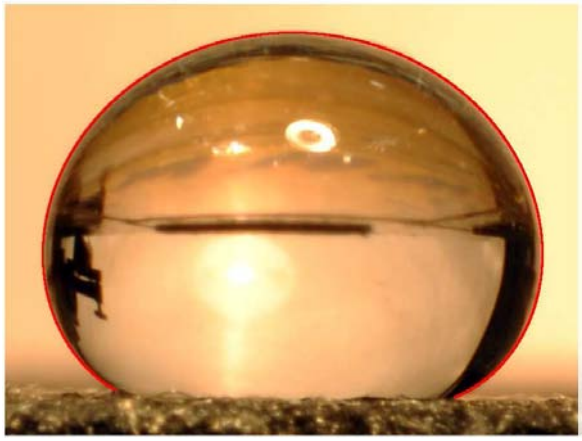

Figure 5: Water drop on a hydrophobic surface. The drop contour fitted with the procedure described in [25] is evidenced, showing the very good agreement between the Laplacian and the real drop profiles.

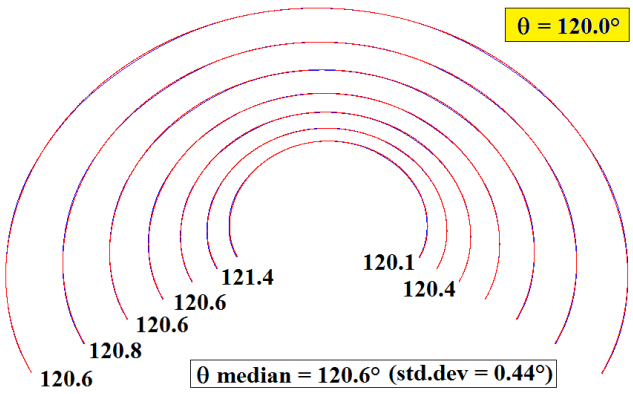

Figure 6: Comparison between the numerical and "analytical" (numerical integration of the Laplace-Young equation) results for the shape of a water drop on a hydrophobic surface and contact angle determination using images with different resolutions, to investigate the effect of such parameter on the measurement.

The ability of *interFoam* to correctly reproduce drop shapes (both in wetting and nonwetting conditions) may allow its use for improved VOF simulations of cases where the drop shape has been up to now considered as spherical or commercial solvers have been used (e.g. simulation of dropwise cooling [29–31], drop growth and detachment in the channels of fuel cells [32–34]).

WETTING DROPS ON A CURVED SURFACE

In a previous paper [25], a procedure to determine the static contact angle from measurements on curved surfaces was proposed. On a curved surface, if the drop is not perfectly symmetric with respect to the curvature (as it is in [35]) the contact angle is still a static as-placed one [36], but at each point of the contact line a different component of "recession" or "advancement" can be hypothesized [37] (Fig. 7), so that a different contact angle in the spectrum between the minimum receding and the maximum advancing contact angles is actually measured. Therefore, a new approach was proposed: the angle between the tangent to the drop profile and the horizontal ("drop angle" in the following) is plotted as a function of the angle between the tangent to the base profile and the horizontal ("base angle" in the following). The angles are measured from $-\pi$ to $+\pi$ along with the scheme shown in Fig. 8. Such function shows a fair linear trend and a linear fitting can be calculated. The intercept of the fitting is the value of the drop angle in correspondence of a horizontal baseline (base angle = 0°). The linear fitting implicitly keeps in account the "advancing" and "receding" contributions to the drop angles due to the baseline inclination, contributions which are zero when the baseline is horizontal. Therefore the cited intercept is an estimate for the "equilibrium" contact angle of an "as placed" drop on a flat surface. From that, the maximum advancing, minimum receding and equilibrium contact angles can be estimated following the approach described in [36].

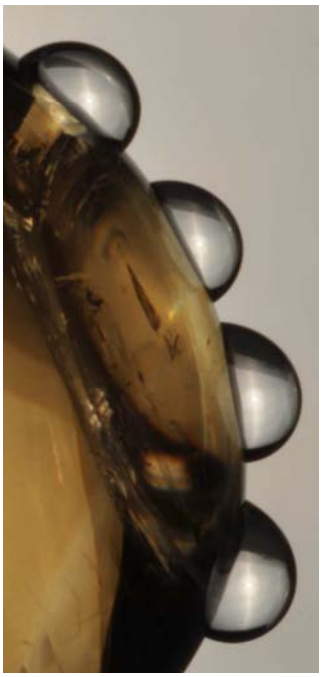

Figure 7: Drops on a curved surface: effect of the surface curvature and inclination.

For the present paper, the described procedure was applied to numerically simulated drops on curved surfaces. Such surfaces were created and converted into a STL file using Matlab® and they were introduced as the bottom boundary of the domain using the *snappyHexMesh* OpenFOAM® utility. Boundary conditions of slight hydrophobicity (static contact angle 100°) were set on such surfaces. The drops

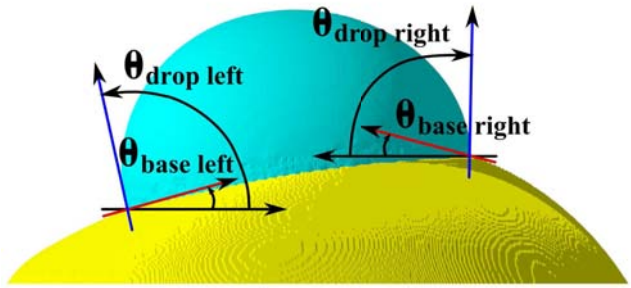

Figure 8: Sketch of the measured angles for contact angle determination on a curved surface.

were initialised as spheres intersecting the curved domain floor using the *funkySetFields* OpenFOAM® utility and let evolve towards their equilibrium shape. Then, base and drops contours were extracted as before from cross-sections of the results using ParaView®. Smoothing splines were fitted to each contour and tangents to the resulting curves were calculated at the contact points. Fig. 9 and 10 show an example of results. The agreement is good and this is a confirmation of the validity both of the simulations and of the procedure.

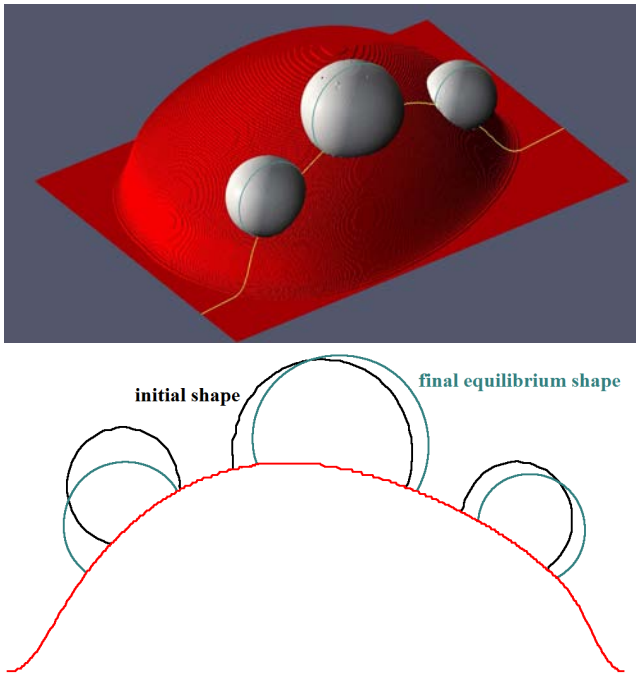

Figure 9: Drops on curved surfaces: 3D view of the equilibrium shape and cross-sections of the initial and final shapes.

DROP DEPOSITION ON A MICROFIN SURFACE

At the Department of Energy, Politecnico di Milano has been active for some years now a research program about drop interaction with microfin surfaces, both from the adiabatic point of view (drop deposition and impact, drop shape, contact angles - Fig. 11) and from the thermal point of view (evaporative dropwise cooling) [26, 38]. Comparisons were therefore performed between numerical simulations and experimental data for drop deposition and drop shape on surfaces with microfins having triangular section. Three

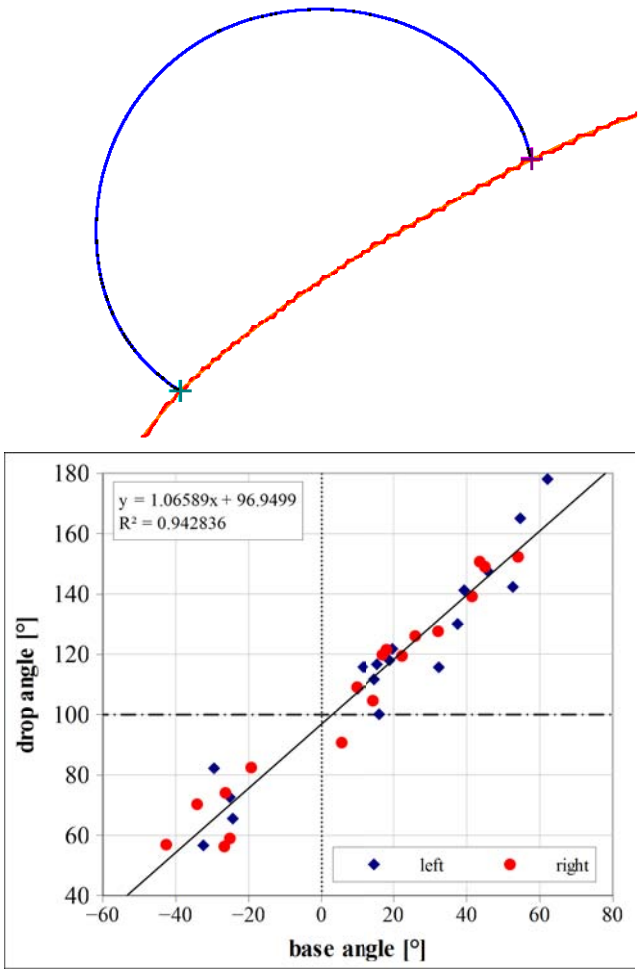

Figure 10: Drops on curved surfaces: contact angle measurement using the procedure described in [25].

cases were simulated: the deposition of a $85 \cdot 10^{-9}$ m^3 water drop onto an aluminium microfin surface characterized by microfin height H = 250 µm, base B = 500 µm, spacing S = 880 µm (case 1), and the deposition of a $85 \cdot 10^{-9}$ m^3 (case 2) and a $80 \cdot 10^{-9}$ m^3 (case 3 a and b) water drops onto a brass microfin surface characterized by microfin height H = 400 µm, base B = 865 µm, spacing S = 1250 µm. For cases 1, 2 and 3a the surface was modelled and converted into a STL file using Matlab® and then introduced as the bottom boundary of the domain using the *snappyHexMesh* OpenFOAM® utility. For the third case, a home-made pre-processing Matlab® file was also tested. It creates a *blockMeshDict* file readable by the *blockMesh* OpenFOAM® starting from two matrixes containing the heights of the "floor" and the "ceiling" of the domain (case 3b). Figure 12 shows some details of the geometry and mesh for the different cases.

The drop was initialized as a sphere with the lower point at $5 \cdot 10^{-4}$ m over the base surface, then it was let fall due to gravity and evolve towards the static equilibrium shape. Such relaxation time is quite long if compared with the time step imposed to respect the Courant number limits: setting real viscosities, it is of the order of 0.3-0.4 s to macroscopically reach the final shape (despite oscillations are still present); it becomes shorter and with dampened oscillations if increased

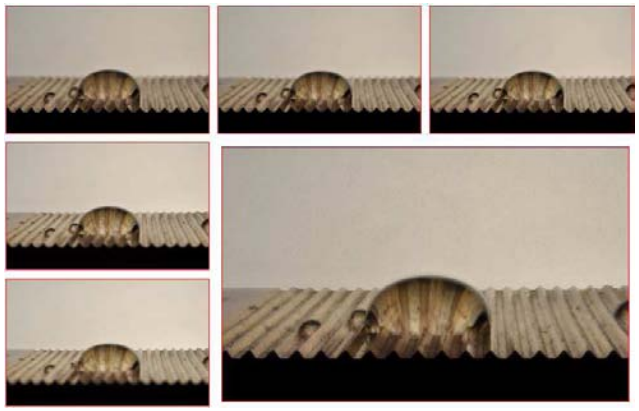

Figure 11: Deposition on the brass 400 µm microfin surface, 85 µl water drop: experimental results with DOF enhancement by image blending, in order to focus both the drop and the surface sample.

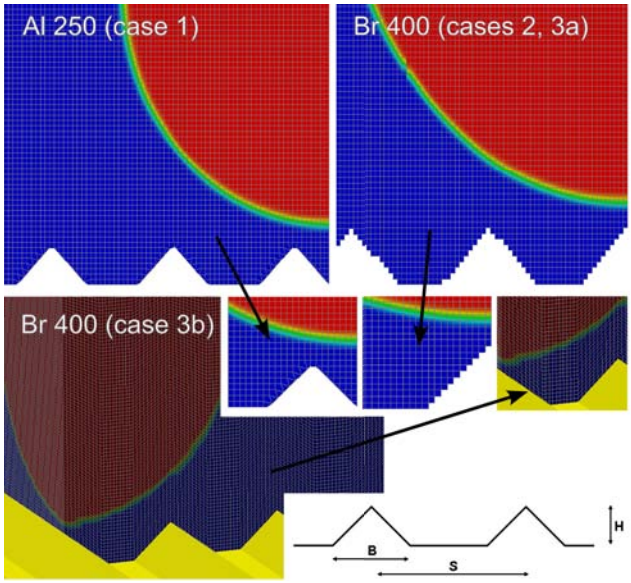

Figure 12: Drop deposition on microfin surfaces: details of the geometry and meshes for the three investigated cases.

viscosities are used. The consequence is that the simulation were extremely time consuming (up to 28 days for case *3b*).

Figures 13, 14, 15 show some results from the simulations, while Figs. 16, 17 show some image sequences (to be observed row-wise) extracted from experimental video acquisitions at 240 fps. They were adjusted in brightness and contrast to improve their visibility. The case in analysis is the gentle deposition of a drop of water on the brass 400 µm microfin surface. Despite the very low resolution (320x240 px) of the experimental images, they allow to observe the good agreement with the numerical results from the qualitative point of view and in terms of time duration of the deposition transient. Figure 18 shows an analogous image sequence for a low-speed drop impact, where the same features highlighted in [39] (e.g. ridges, aligned drop front) can be recognized.

Concerning the final equilibrium condition, the drop shape and dimensions were compared with experimental results and models [40]. Starting from the latter, Fig. 19 shows the results of the comparison of the simulated contact profile (case 3a) with the equation by Chen *et al.* [40]. As the

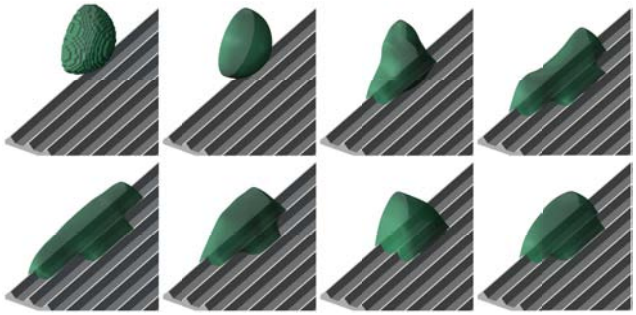

Figure 13: Drop deposition on the aluminium 250 μm microfin surface: 3D view of the numerical drop shape evolution (drop volume $85 \cdot 10^{-9}$ m^3, time = 0:14:98 ms).

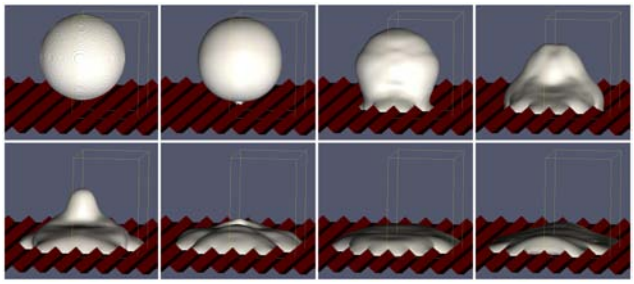

Figure 14: Drop deposition on the brass 400 μm microfin surface: 3D view of the numerical drop shape evolution (drop volume $85 \cdot 10^{-9}$ m^3, time = 0:8:48 ms).

drop dimensions are an input for the model, the true subject of the comparison is the projected shape. The agreement is satisfactory, particularly if considering that the model was developed for smaller grooves, which impose a much smaller distortion to the drop.

On the contrary, the agreement is not good when the cross-microfin section is considered (Fig. 20). The simulated drops cover the same number of grooves of the real ones, but the 85 μl drop on the brass surface is much lower than the real one. For case 3a, part of the fault is of the modelling of the microfin surface: creating it as a jagged surface forces the contact angle to be imposed on a horizontal or vertical surface, while in reality the contact line is along a oblique surfaces. Case 3b was run specifically to verify this aspect, by modelling the domain with truly oblique and not jagged microfin sides. Unfortunately improvement is only slight, suggesting that other issues still affect negatively the agreement. Among them, some concern the experimental part: it is difficult to let the drop fall exactly with the same height and shape of the simulations. The real drop detaches from a Plexiglas® block mimicking a infinite horizontal surface and in many cases it touches the base surface before complete detachment from the block (see the first frames of Figs. 16 and 17), being therefore different in shape from the spherical drop initialized in the simulations. The problem might be solved by slightly increasing the height of deposition, but this would influence a lot the final drop shape, which would become much more "flat" and "axisymmetric" with respect to the truly sessile one [26].

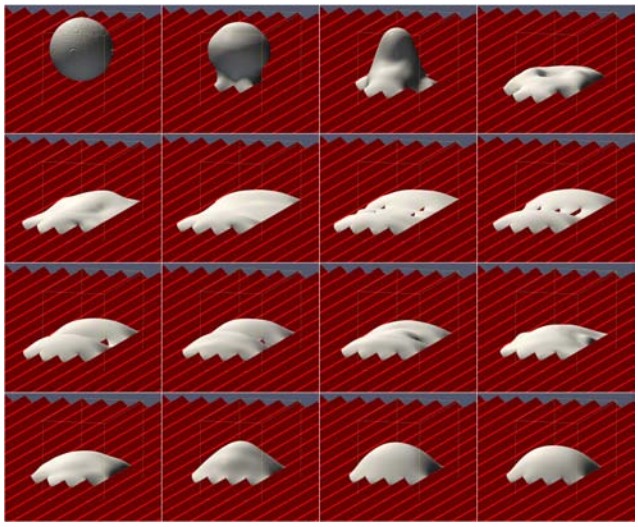

Figure 15: Drop deposition on the brass 400 μm microfin surface: 3D view of the numerical drop shape evolution (drop volume $80 \cdot 10^{-9}$ m^3, time = 0:8:120 ms).

DROP-ONTO-DROP IMPACT

The last performed simulation concerned the impact of a drop onto another drop previously deposed on a flat hydrophilic surface. While a large number of studies can be found in literature concerning drop impact onto liquid films, from both the experimental and CFD points of view, very few papers [41] are available about drop-onto-drop impacts.
The simulation of this case started from the final results of the case of the wetting drop, with the latter in the role of the sessile drop. The second drop was initialized (again using the *funkySetFields* OpenFOAM® utility) as a sphere with diameter 2 mm, moving along the vertical direction at 1.4 m/s towards the domain floor and the first drop. Simulations were performed both using the *interFoam* solver and the *multiphaseInterFoam* (version 1.7.1) solver. With the latter, the water belonging to each drop can be distinguished during all the simulation [7]. Figure 21 shows the results: on the first column the *interFoam* output (where the colors indicate mesh resolution), on the second column the *multiphaseInterFoam* (where the colors indicate the different liquid phases, first and second drop). It can be noticed how the results are mesh independent and the agreement between the two-phase and the multiphase solvers is good for the first time steps, then the multiphase solver shows an evolution (including complex mixing between the two drops) which seems less realistic and credible. The third column of Fig. 21 shows experimental results. The resolution offered by the Nikon AW100 at high speed frame rates (320x240 px at 240 fps) was in this case insufficient to capture the details of the interaction between the two drops. Such results were therefore obtained by shooting photo sequences (at 4 fps, exposure time 1/4000 s) of many impacts with the D90 DSLR and extracting the most interesting images. Consequently, it is impossible to say at which precise time step the experimental pictures correspond, and only a qualitative comparison can be performed. Moreover, the drops dimensions do not strictly correspond to the numerical ones. Despite these heavy limitations, it may be said that the numerical simulations, particularly with the two-phase

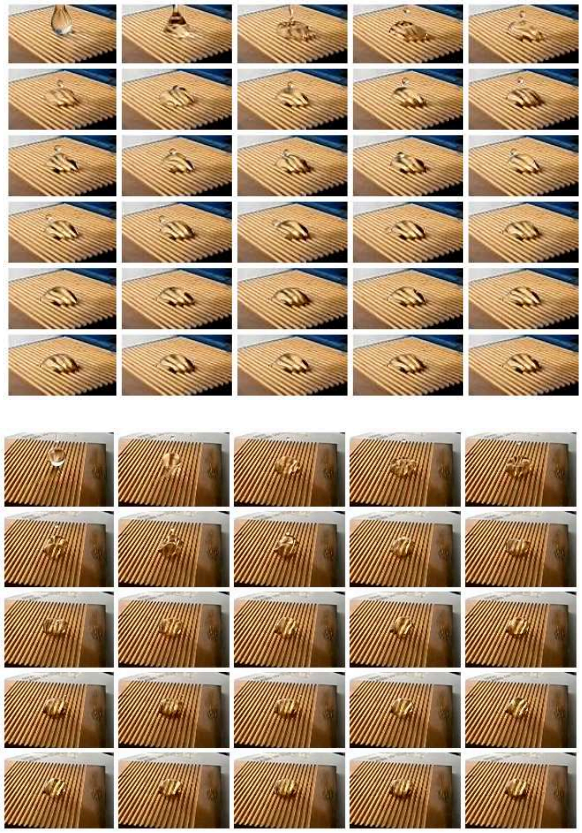

Figure 16: Drop deposition on the brass 400 μm microfin surface: experimental video acquisitions at 240 fps.

solver, correctly captured many phenomena observed during the experiments: e.g. the shape of the second drop just after the impact, the crater which forms in the first drop, the "donut" shape and central cone during the recoil.

CONCLUSIONS

Some comparisons were performed between numerical results, experimental results and models to evaluate the performances of the two-phase and multiphase solvers of the OpenFOAM® CFD package in the fields of drop deposition and low-speed impact. The cases of the sessile drop on a hydrophilic and hydrophobic flat and curved surfaces showed very good agreement between numerical results and experiments/models. Good qualitative agreement was also found for the cases of drop deposition on microfin surfaces and drop-onto-drop impact. From the quantitative point of view, the latter cases evidenced on the contrary some discrepancies, which may in part be attributable to modeling inaccuracies and difficulties in reproducing exactly the same initial conditions between simulations and experiments. In summary, the two-phase OpenFOAM® solver appears to be a fairly reliable tool for CFD simulations in the field of drop-surface interaction. Further validation is on the contrary needed for the multiphase solver, despite its very promising characteristics. Results can be obtained using a single personal computer, even if the simulation time for most cases is very long (between some days and one month).

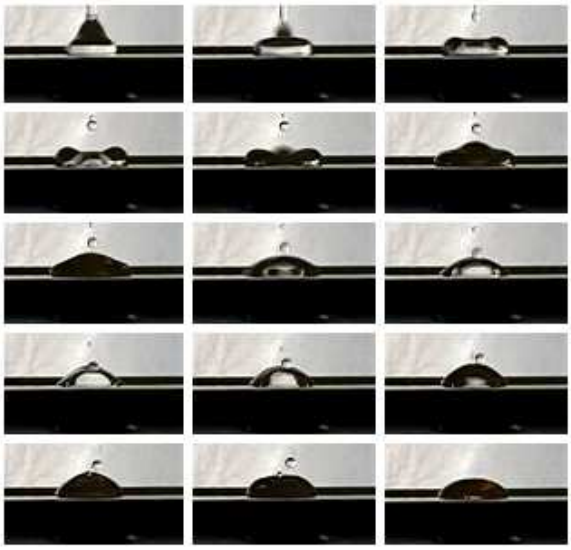

Figure 17: Drop deposition on the brass 400 μm microfin surface: experimental video acquisition at 240 fps, side view (fins are orthogonal to the camera direction).

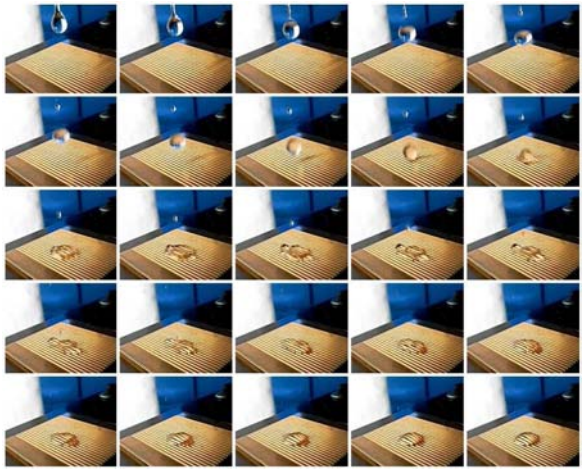

Figure 18: Low-speed impact onto the brass 400 μm microfin surface: experimental video acquisition at 240 fps.

ACKNOWLEDGMENTS

Prof. Giorgio Sotgia started the research activity about drop-surface interaction and microfin surfaces at the Department of Energy, Politecnico di Milano. His contribution is gratefully acknowledged.

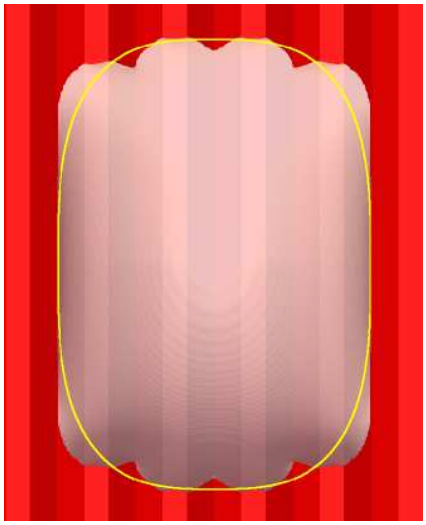

Figure 19: Deposition on the brass 400 µm microfin surface, 85 µl water drop: comparison of the simulated contact profile and apparent contact area (case 3a) with the model by Chen *et al.* [40].

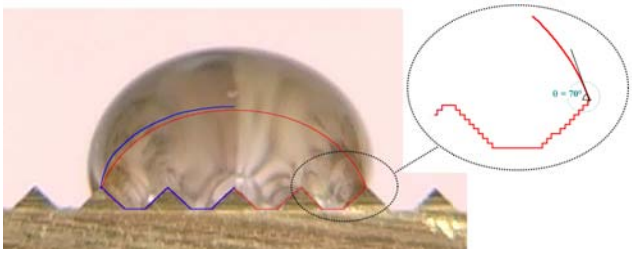

Figure 20: Deposition on the brass 400 µm microfin surface, 85 µl water drop: comparison of the simulated (red: case 3a, blue: case 3b) and experimental cross-section profile.

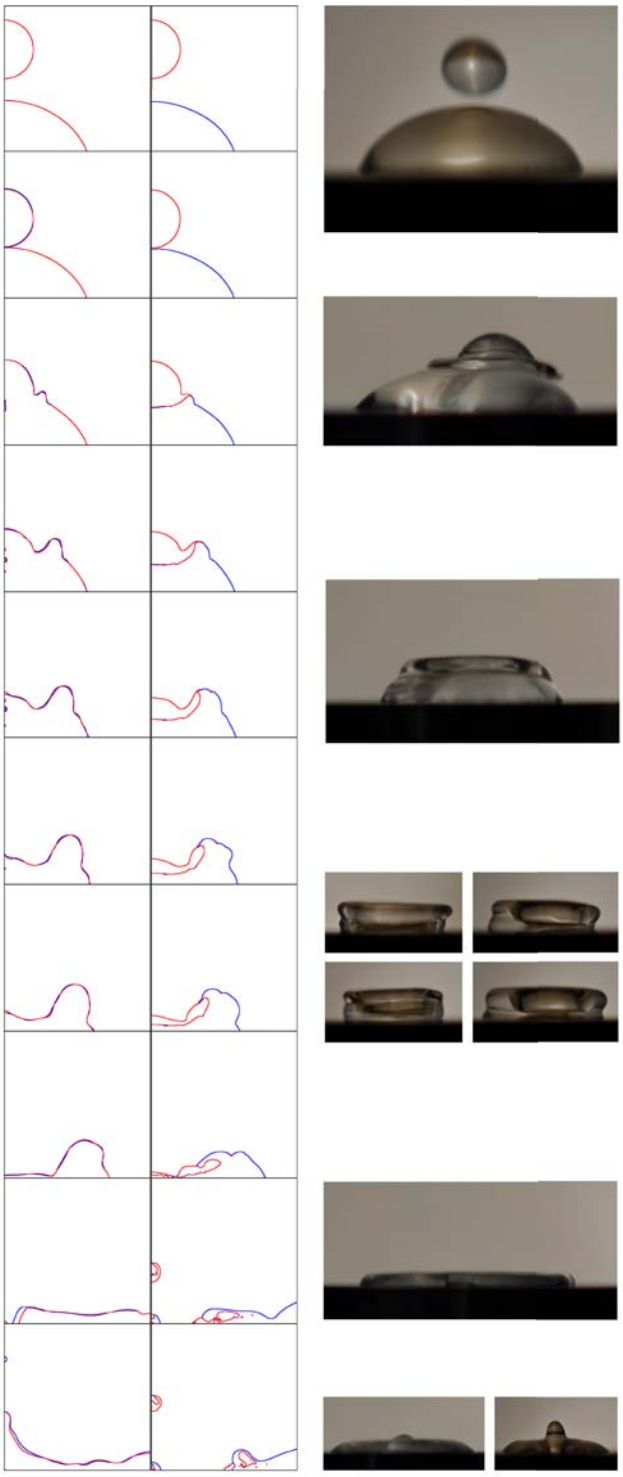

Figure 21: Drop-onto-drop impact simulated using *interFoam* (left column, blue: results with a mesh composed by 62500 cells, red: results with a mesh composed by 250000 cells) and *multiphaseInterFoam* (right column, blu: first drop, red: second drop), compared to experimental results (shots at 4 fps, exposure time 1/4000 s).

REFERENCES

[1] WS Atkins Consultants et al., *Best Practice Guidelines for Marine Applications of Computational Fluid Dynamics*, MarnetCFD, website: https://pronet.wsatkins.co.uk/marnet/publications/bpg.pdf, accessed June 2012.

[2] OpenFOAM®, The open source CFD toolbox, website: http://www.openfoam.com/, accessed March 2012.

[3] Costa A.B., Graham Cooks R., *Simulated splashes: Elucidating the mechanism of desorption electrospray ionization mass spectrometry*, Chemical Physics Letters, 2008, 464, 1-8.

[4] Berberovic E., van Hinsberg N.P., Jakirlic S., Roisman I.V., Tropea C., *Drop impact onto a liquid layer of finite thickness: Dynamics of the cavity evolution*, Physical Review E 79, 036306, 2009.

[5] Roisman I.V., Berberovic E., Jakirlic S., Tropea C., *Dynamics of two-phase flows induced by drop collisions*, Proceedings of the 7^{th} International Conference on Multiphase Flow (ICMF), Tampa (FL,USA), 2010.

[6] Fest-Santini S., Guilizzoni M., Santini M., Cossali G.E., *Drop impacts in pools: a comparison between high speed imaging and numerical simulations*, Proceedings of the Droplet Impact Phenomena & Spray Investigations (DIPSI) Workshop 2011, Dalmine (Italy).

[7] Santini M., Fest-Santini S., Guilizzoni M., Cossali G.E., *Drop impact onto a deep pool: study of the crater evolution*, Proceedings of the 24^{th} European Conference on Liquid Atomization and Spray Systems (ILASS - Europe 2011), Estoril (Portugal), 2011.

[8] E. Berberovic, *Investigation of Free-surface Flow Associated with Drop Impact: Numerical Simulations and Theoretical Modeling*, Ph.D. Thesis, TU Darmstadt, 2010.

[9] Roisman I.V., Weickgenannt C.M., Lembach A.N., Tropea C., *Drop impact close to a pore: experimental and numerical investigations*, Proceedings of the 23^{rd} Annual Conference on Liquid Atomization and Spray Systems, Brno, Czech Republic, September 2010.

[10] Sabry M.N., ElGharieb E., *Droplet dynamics over a super hydrophobic surface*, Thermal Issues in Emerging Technologies (ThETA 3), Cairo (Egypt), 2010.

[11] Gomaa H., Kumar S., Huber C., Weigand B., Peters B., *Numerical Comparison of 3D Jet Breakup Using a Compression Scheme and an Interface Reconstruction Based VOF-Code*, Proceedings of the 24^{th} European Conference on Liquid Atomization and Spray Systems (ILASS - Europe 2011), Estoril (Portugal), 2011.

[12] Jacobsen F., *Application of OpenFOAM for designing hydraulic water structures*, Open Source CFD International Conference, Barcelona (Spain), 2009.

[13] Paterson E., Smith K., Ford S., *Simulation Of Wakes, Wave Impact Loads, And Seakeeping Using OpenFOAM*, 4^{th} OpenFOAM Workshop, Montreal (Canada), 2009.

[14] Horvath A., Jordan C., Lukasser M., Kuttner C., Makaruk A., Harasek M., *CFD Simulation of Bubble Columns using the VOF Model: Comparison of commercial and Open Source Solvers with an Experiment*, Chemical Engineering Transactions, 2009, 18, 605-610.

[15] Gram A., *Modeling Free Surface Flow using multiphaseInterFoam*, PhD course in CFD with OpenSource software, Chalmers University of Technology, 2008, website: http://www.tfd.chalmers.se/~hani/kurser/OS_CFD_2008/AnnikaGram/reportAnnikaGram.pdf

[16] Weller H.G., Tabor G., Jasak H., Fureby C., *A tensorial approach to computational continuum mechanics using object-oriented techniques*, Computer in Physics, 1998, 12(6), 620-631.

[17] Jasak H., Weller H.G., *Interface-tracking capabilities of the InterGamma differencing scheme*, Technical Report, Imperial College of Science, Technology and Medicine, University of London, 1995.

[18] Gopala V.R., van Wachem B.G.M., *Volume of fluid methods for immiscible-fluid and free-surface flows*, Chemical Engineering Journal, 141 (2008) 204-221.

[19] Hirt, C.W., Nichols, B.D., *Volume of fluid (VOF) method for the dynamics of free boundaries*, Journal of Computational Physics, 1981, 39, 201-225.

[20] Brackbill J.U., Khote D.B, Zemach C., *A Continuum Method for Modeling Surface Tension*, Journal of Computational Physics, 1992, 100, 335-354.

[21] Ferziger J.H., Peric M., *Computational Methods for Fluid Dynamics*, 3^{rd} ed., Springer, 2002.

[22] Andersson P., *Tutorial multiphaseInterFoam for the damBreak4phase case*, PhD course in CFD with OpenSource software, Chalmers University of Technology, 2010, website: http://www.tfd.chalmers.se/~hani/kurser/OS_CFD_2010/patrikAndersson/patrikAnderssonReport.pdf

[23] Roisman I.V., Opfer L., Tropea C., Raessi M., Mostaghimi J., Chandra S., *Drop impact onto a dry surface: Role of the dynamic contact angle*, Colloids and Surfaces A: Physicochemical and Engineering Aspects, 2008, 322, 183-191.

[24] Criscione A., Rohrig R., Jakirlic S., Roisman I.V., Tropea C., *Impacting Droplets: Dynamic Contact Angle Modeling in OpenFOAM*, 7^{th} OpenFOAM Workshop, Darmstadt (Germany), 2012.

[25] Guilizzoni M., *Drop shape visualization and contact angle measurement on curved surfaces*, Journal of Colloid and Interface Science, 2011, 364, 230-236.

[26] Guilizzoni M., Sotgia G., *Experimental analysis on the shape and evaporation of water drops on high effusivity, microfinned surfaces*, Experimental Thermal and Fluid Science, 2010, 34, 93-103.

[27] Rotenberg Y., Boruvka L., Neumann A.W., *Determination of surface tension and contact angle from the shapes of axisymmetric fluid interfaces*, Journal of Colloid and Interface Science, 1983, 93(1), 169-183.

[28] Fest-Santini S., Guilizzoni M., Santini M., Cossali G.E., *Drop Impact onto hydrophobic and superhydrophobic surfaces*, XXIX National UIT Heat Transfer Conference, Turin (Italy), 2011.

[29] Hu, H., Larson, G., *Evaporation of a sessile droplet on a substrate*, Journal of Physical Chemistry, 2002, 106, 1334-1344.

[30] Ruiz O.E., Black W.Z., *Evaporation of water droplets placed on a heated horizontal surface*, Journal of Heat Transfer - Transactions of the ASME, 2002, 24, 854-863.

[31] Mollaret R., Sefiane K., Christy J.R.E., Veyret D., *Experimental and Numerical Investigation of the Evaporation into Air of a Drop on a Heated Surface*, Chemical Engineering Research and Design, 2004, 82(4), 471-480.

[32] Cho S.C., Wang Y., Chen K.S., *Droplet dynamics in a polymer electrolyte fuel cell gas flow channel: Forces, deformation, and detachment. I: Theoretical and numerical analyses*, Journal of Power Sources, 2012, 206, 119-128.

[33] Zhu X., Sui P.C., Djilali N., *Dynamic behaviour of liquid water emerging from a GDL pore into a PEMFC gas flow channel*, Journal of Power Sources, 2007, 172, 287-295.

[34] Zhu X., Liao Q., Sui P.C., Djilali N., *Numerical investigation of water droplet dynamics in a low-temperature fuel cell microchannel: Effect of channel geometry*, Journal of Power Sources, 2010, 195, 801-812.

[35] Bormashenko E., *Wetting of Flat and Rough Curved Surfaces*, Journal of Physical Chememistry C, 2009, 113, 17275-17277.

[36] Tadmor R., Yadav P.S., *As-placed contact angles for sessile drops*, Journal of Colloid and Interface Science, 2008, 317, 241-246.

[37] Extrand C.W., Moon S.I., *Contact Angles on Spherical Surfaces*, Langmuir, 2008, 24, 9470-9473.

[38] Guilizzoni M., Sotgia G., Osnato F., *Evaporation of sessile and impinging water drops on microfinned metallic surfaces*, XXVII National UIT Heat Transfer Conference, Reggio Emilia (Italy), 2009.

[39] Kannan R., Sivakumar D., *Drop impact process on a hydrophobic grooved surface*, Colloids and Surfaces A: Physicochem. Eng. Aspects 2008, 317, 694-704.

[40] Sommers A.D., Jacobi A.M., *Wetting phenomena on micro-grooved aluminum surfaces and modeling of the critical droplet size*, Journal of Colloid and Interface Science, 2008, 328, 402-411.

[41] Nikolopoulos N., Strotos G., Nikas K.S.P., Theodorakakos A., Gavaises M., Marengo M., Cossali G.E., *Single droplet impacts onto deposited drops. Numerical analysis and comparison*, Atomization and Sprays, 2010, 20 (11), 935-953.

EXPERIMENTAL AND NUMERICAL ANALYSIS OF THE SINGLE DROPLET IMPACT ONTO STATIONARY ONES

N. Nikolopoulos[1,2], G. Strotos[2], K.S Nikas[2], A. Theodorakakos[3], M. Gavaises[4], M. Marengo[5], G.E. Cossali[5]

[1] Centre for Research and Technology Hellas, 4th km Ptolemais Mpodosakeiou, Ptolemaida, Greece
[2] Technological Education Institute of Piraeus, Mechanical Engineering Department, Fluid Mechanics Laboratory, 250 Thivon & P. Ralli str., Aegaleo, 12244, Greece
[3] Fluid Research Co. 49 Laskareos Str, 11472, Athens, Greece
[4] City University London, School of Engineering and Mathematical Sciences Northampton Square, EC1V 0HB, London, UK
[5] Dept. of Industrial Engineering, University of Bergamo, viale Marconi 5, 24044 Dalmine, Italy
[C]Corresponding author: Nikolopoulos Nikos, n.nikolopoulos@certh.gr, 4th km Ptolemais Mpodosakeiou, Ptolemaida, Greece

ABSTRACT

The present paper investigates experimentally and numerically the impact of a spherical water droplet onto a stationary sessile one lying onto a substrate. The experiments were performed with two different film thicknesses, three different We numbers and two surface contact angles (two substrates, aluminium and glass). For this purpose a CCD camera was used and the corresponding qualitative and quantitative characteristics regarding the time evolution of the phenomenon, such as the diameter and height of the evolving crown, were obtained by image analysis. The aforementioned investigation was extended applying also the V.O.F (Volume Of Fluid) numerical methodology for the prediction of the temporal evolution of the phenomenon, so as to identify important characteristics of the induced flow field, not easy to be measured. This permits the in depth understanding of the governing flow laws, which resemble to those in the case of a droplet impact onto shallow films. The governing Navier-Stokes equations are solved both for the gas and liquid phase coupled with an additional equation for the transport of the liquid interface. An unstructured numerical grid is used along with an adaptive local grid refinement technique, increasing the numerical accuracy along the liquid-gas interface with the minimum computational cost. The numerical model is validated against the corresponding experimental data showing a good agreement. The regimes of deposition and splashing are identified as a function of We number and of the maximum thickness of the steady film, which is affected by the surface wettability properties. Moreover, following an analysis of the controlling parameters describing the temporal evolution of the lamella spreading, the role of We and Oh numbers as also of the wetting contact angle were identified, providing analytical expressions for the main dimensions characterizing the phenomenon.

INTRODUCTION

The sequential impact of droplets onto solid and/or liquid surfaces is an interesting phenomenon which can be found in many engineering applications such as metallurgical industry, surface cooling, fire suppression, electronic circuits, inkjet printing etc. The investigation of any related to droplet impacts phenomenon requires the examination of the most significant dimensionless numbers, such as the Weber number (We), the Reynolds number (Re) and the Froude number (Fr), defined as:

$$We = \frac{\rho_l U_0^2 D_0}{\sigma}, \quad Re = \frac{\rho_l U_0 D_0}{\mu_l}, \quad Fr = \frac{U_0^2}{g D_0} \tag{1}$$

Other dimensionless numbers often used, relevant to the aforementioned, are the Ohnesorge (Oh) and the Bond (Bo) number, defined as:

$$Oh = \frac{We^{1/2}}{\mathrm{Re}} = \frac{\mu_l}{\sqrt{\rho_l \sigma D_0}}, \quad Bo = \frac{We}{Fr} = \frac{\rho_l g D_0^2}{\sigma} \tag{2}$$

The present investigation examines the impact of a droplet onto a stationary one. The phenomenon is expected to be a combination of the phenomena observed during droplet impact either onto a solid wall and/or onto a shallow film. A brief review of the phenomena observed during droplet impact onto solid and liquid surfaces can be found in Rein 1993 [1], along with some representative numerical works related with these phenomena [2-7]. However, despite the in depth investigation of droplet impacts onto solid surfaces and films of various thickness, very few information can be found in the literature as far as droplet impact onto sessile ones is concerned. For this reason, this study is focused on the experimental and numerical investigation of a finite chain of water droplets (two and three droplets in a row, after reaching a stable shape) impinging on a solid wall under atmospheric conditions, where the impacting droplet velocity, the height of the pre-existing liquid film, and the wettability characteristics of the solid substrate are the controlling parameters. The main difference with the most common experiments of impact on uniform liquid films is related to the influence of wall wettability on this phenomenon. Such an influence is evidenced both on the thickness of the film formed by the previously impacted drops and on the dynamic contact angle, which influences the movement of the contact line after the impact of the last drop.

EXPERIMENTAL SETUP

The experimental rig used for the experiments is shown in Fig. 1. It comprises of a drop generator made by a suspended needle positioned at a distance ranging between 150 and 440 mm from the solid wall and connected with a small water tank. The detachment of single droplets is achieved by a small pressure pulse produced by the opening of a solenoid valve. The droplet diameter was

measured after enlarging the falling droplet's pictures at various time instants. The mean value was equal to Do = 4.02 mm, with a repeatability better than 6%, while the impact velocities ranged between 1.7 and 2.8 m/s. Two different solid plates were used, of either aluminum or glass composition, in order to analyse the effect of wettability on the evolution of the phenomenon. In all cases, distilled water at approximately 20°C under atmospheric conditions was used. A charge-coupled device (CCD) camera (Colour PCO SensiCam, 1280 × 1024 pixels) and a short duration flash lamp (Strobe) were used in order to capture the evolution of the phenomenon at various time instants before and after impact. Calibration for size measurements was obtained from the image analysis of pictures of known dimension bodies (needles).

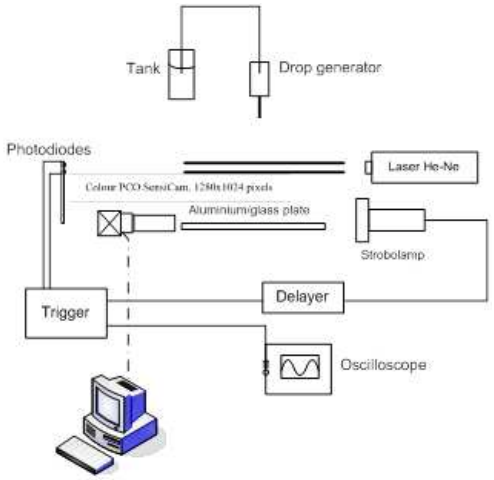

Figure 1: Drop impact test rig

	Case	D_0 (mm)	U_0	We	Re	Plate	δ=h/D_0	ACA (°)
2 droplets	A	4.02	1.7	161	6800	Aluminium	0.215	60
	B	4.02	2.5	348	10000	Aluminium	0.23	60
	C	4.02	2.6	377	10400	Aluminium	0.234	60
	D	4.02	2.2	270	8800	Glass	0.130	10
	E	4.02	2.4	321	9600	Glass	0.146	10
	F	4.02	2.65	391	10600	Glass	0.120	10
3 droplets	A	4.02	1.7	161	6800	Aluminium	0.329	60
	B	4.02	2.5	348	10000	Aluminium	0.277	60
	C	4.02	2.6	377	10400	Aluminium	0.266	60
	D	4.02	2.2	270	8800	Glass	0.140	10
	E	4.02	2.4	321	9600	Glass	0.180	10
	F	4.02	2.65	391	10600	Glass	0.162	10

Table 1: Examined cases, the number of droplets refer to those used to build the residual liquid bulk.

The image analysis of the experimental data allowed identification of at least two different regimes: (a) a deposition regime, with the formation of a crown but not followed by a breakup, and (b) a splashing regime characterized by the crown's breakup into numerous satellite droplets. Reasonably, an additional regime should exist for low impact velocities, where the impacting droplet deposits on the stationary liquid bulk, without the formation of any crown. This also occurs in the case of an impacting droplet onto a thin liquid film [8], but this regime was not investigated experimentally in the present paper.

Representative figures depicting the temporal evolution of droplet impact onto sessile ones are given in Fig.2a, 2b, 2c and 2d, but more information on these can be found in [9-10]. Table 1 reports the experimental conditions, in dimensionless form, for all the performed experiments. The time evolution of the phenomenon can be described by four main phases, whose characteristics can be distinguished from the relevant images. As shown in Fig. 2a, the droplets merge at once after their first contact, and the lamella's rim moves towards the liquid–solid contact line that, after being reached by the lamella, starts to move radially (compare the picture at 2.64 ms and 6.24 ms). During this spreading phase, the crown evolves radially and vertically. At subsequent times this crown evolves, as in the case of a droplet impacting onto a liquid film [11–13]. Dependent on the initial kinetic energy (impact velocity) and surface energy of the impacting droplet, this crown may either start collapsing without (deposition regime, Fig. 2a, t = 9.84–13.44 ms) or with (splashing regime, Fig. 2c, t = 2.75–9.52 ms) jetting phenomena and secondary droplets detachment.

During the final collapse, the surface energy is transformed back to kinetic energy under the effect of surface tension forces and gravity, and the crown begins to recede toward the solid substrate. For case A (low We, equal to 161) the formation of rim instabilities is observed, but no jets are produced because the kinetic energy is not high enough (Fig. 2a, t = 6.24 ms). Increasing the We number of the impacting droplets, the detachment of satellite droplets becomes more evident, even at the first stages of impact. This phenomenon shows similar characteristics to the "prompt" splash phase occurring in the case of a single droplet onto shallow films [11–13]. The remaining lamella later collapses for all cases examined, under the effect of gravity.

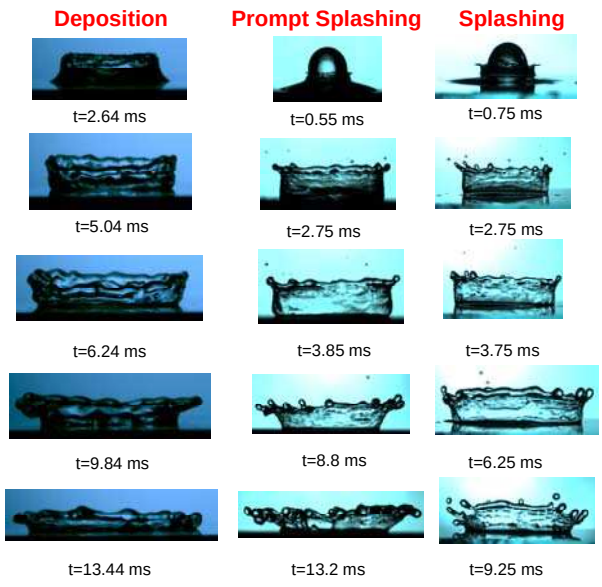

Figure 2: a) Temporal evolution of case A (2 droplets), b) Temporal evolution of case C (2 droplets), c) Temporal evolution of case F (2 droplets).

NUMERICAL SETUP

Each phase (gas and liquid) is identified by the volume fraction α (ratio of liquid volume in a cell over the cell volume), following the Volume of Fluid Method (V.O.F) methodology by Hirt & Nichols [14]. The α-function is equal to 1 for a point of the computational domain inside the liquid phase, 0 inside the gas phase and lies between 0 and 1 in the gas-liquid interface. The discretization of the convection terms of the velocity components is based on a high resolution convection-diffusion differencing scheme (HR scheme) proposed by Jasak [15]. On the other hand, the discretization of equation of α needs a special treatment in order to avoid numerical diffusion and smearing of the interface. Thus, the high-resolution differencing scheme CICSAM proposed by Ubbink & Issa [16-17] is used and the time derivative is discretized using the second–order Crank-Nicolson scheme, as also small Courant number approximately 0.2-0.3. The non-linear system of the flow equations is solved numerically on a two-dimensional axisymmetric unstructured grid, using a recently developed adaptive local grid refinement technique, (Theodorakakos & Bergeles [18]), which enhances the accuracy at the interface region and achieves low computational cost compared to the case of a uniform grid with the same resolution.

A base grid is used and the cells at the region of the interface are subdivided according to the levels of local grid refinement used, while the interface lies always in the densest grid region since the grid is reconstructed every 10 timesteps. For the cases examined here, a base grid consisting of 3600 cells and 5 levels of local grid refinement was used. This resulted in a resolution of D0/516 at the interface region, which is found to be sufficient for a grid independent solution to be achieved after numerical tests. The number of computational cells varied from 17000 to 24000 (depending on the interface shape) while a uniform grid with the same resolution would require 3.68 million cells.

The time in the graphs presented will be non-dimensionalised as:

$$\tau = t \cdot \frac{U_0}{D_0} \qquad (3)$$

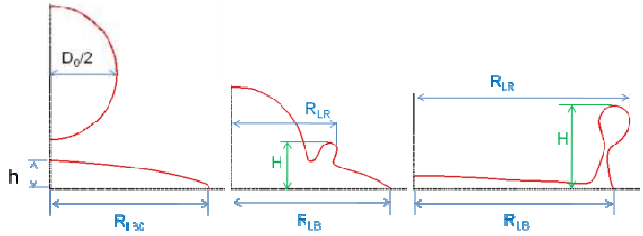

Figure 3a: Problem geometry and definition of the measured magnitudes.

Figure 3b: Longitudinal and azimuthal waves on the surface of the expanding crown, t=2.75ms and (b) satellite droplet detachment during the crown's collapse, t=6.75ms (case E, 3droplets).

Crown's rim radius

The results obtained from the numerical simulation of the examined cases for the temporal evolution of crown's dimensionless radius are presented in Fig. 4a for the cases of 2 droplets and in Fig. 4b for the cases of 3 droplets. In these figures the left one (a) refers to the aluminum substrate and the right one (b) to the glass substrate. As it can be seen, the numerical predictions for the temporal evolution of crown diameter are in a good agreement with the corresponding experimental data and the deviations from the experimental data observed at later stages of the phenomenon, are attributed to the three-dimensional phenomena which become important and cannot be represented with validity by the present axisymmetric simulation. Fig. 4 reveals the invalidity of the axisymmetric numerical approach for the evolution of the phenomenon, after the time that three dimensional effects are evident.

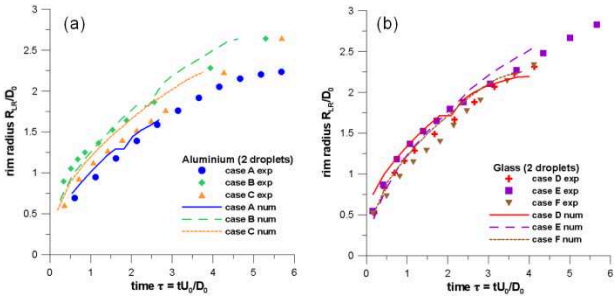

Figure 4a: Temporal evolution of rim's radius for impact on aluminium (a) and glass (b) substrate for the case of 2 droplets.

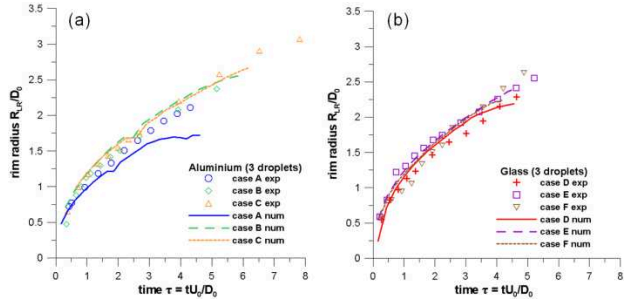

Figure 4b: Temporal evolution of rim's radius for impact on aluminium (a) and glass (b) substrate for the case of 3 droplets.

Base radius

The results obtained from the numerical simulation of the examined cases as far as the temporal evolution of lamella's base dimensionless radius is concerned, are presented in Fig. 5a for the cases of 2 droplets and in Fig. 5b for the cases of 3 droplets. The results for the base radius are characterized by uncertainties in the experimental measurements. The predictions are in a good agreement with the corresponding experimental data, at the initial and middle stages of impact. At latter stages

discrepancies between experimental data and numerical results are owed to the three dimensional character of the phenomenon, which cannot be represented with validity by the present axisymmetric formulation of the physical problem. The base radius is almost constant until around to τ=2 and later the motion of the rim pushes the deposited lamella on the wall to move. That is the reason why there is a time delay for the base radius to increase. At later stages, which are not presented here, the deposited lamella on the wall recedes and finally reaches a stable form.

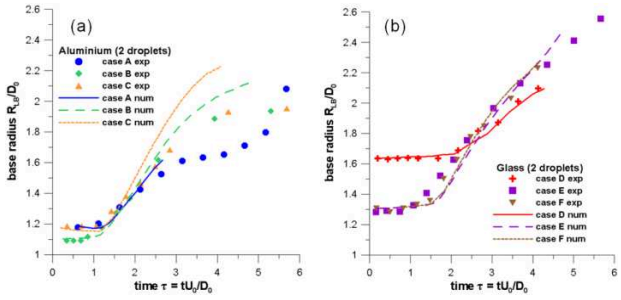

Figure 5a: Temporal evolution of base radius for impact on aluminium (a) and glass (b) substrate for the case of 2 droplets.

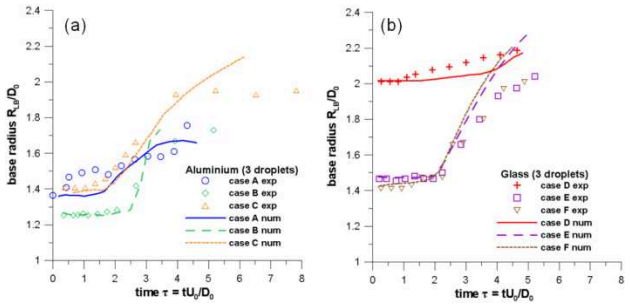

Figure 5b: Temporal evolution of base radius for impact on aluminium (a) and glass (b) substrate for the case of 3 droplets

Crown's height

The results obtained from the numerical simulation of the examined cases for the temporal evolution of the non-dimensional crown's height are presented in Fig. 6a for the cases of 2 droplets and in Fig. 6b for the cases of 3 droplets. The height of the crown increases with time, reaches a maximum, and then decrease under the effect of gravity. The three dimensional character of the deposited lamella and the large fingers, which are inducing on its top rim cannot be represented by the present numerical approach owed to its axisymmetric form.

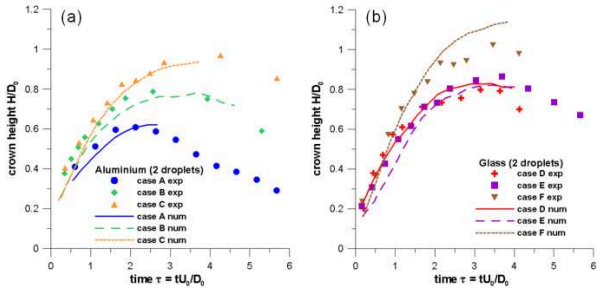

Figure 6a: Temporal evolution of crown's height for impact on aluminium (a) and glass (b) substrate for the case of 2 droplets.

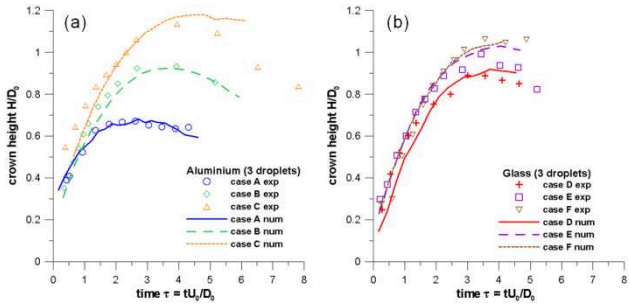

Figure 6b: Temporal evolution of crown's height for impact on aluminium (a) and glass (b) substrate for the case of 3 droplets.

Flow field regimes

In this section, selected frames showing the temporal evolution of droplet shape, dimensionless pressure and dimensionless velocity are presented for cases A2 and F2 in Fig. 7, Fig. 8. Cases A and C have almost the same boundary conditions (2 droplets and aluminium surface) but different We numbers (We=161 and We=376 respectively), while cases C and F have similar We numbers but different boundary conditions regarding the shape of the sessile droplet. In these frames details of the flow field are also presented in enlarged pictures. The dimensionless pressure is presented in the left part of the pictures, while the dimensionless velocity magnitude is presented in the right part of the figures. These magnitudes are defined as:

$$p^* = \frac{p - p_\infty}{\frac{1}{2}\rho_l U_0^2}, \quad U^* = \frac{|\vec{u}|}{U_0} \tag{4}$$

For reasons of distinctness, a narrow range of values for pressure and velocity is presented despite the fact that at the initial stages of impact large values are observed for these magnitudes. Furthermore, the gas-liquid interface presented, corresponds to a VOF value equal to 0.5. For all cases, an advancing crown is created from the early stages of impact (Fig. 7. τ=0.613, Fig. 8. τ=0.317) originating from the peripheral points of the junction of the falling droplet with the sessile droplet. The crown moves radially outwards and vertically upwards and at its edge a thicker rim is formed (Fig. 7. τ=2.133, Fig. 8. τ=1.803). Its motion pulls the lower liquid mass to rise and the base of the sessile droplet increases.

At the initial stages of impact (τ≈0) the dimensionless pressure locally at the point of impact reaches a value of 6-7 and it is proved that the same value is observed for all cases, irrespective of impact velocity. This reveals the dimensionless character of the phenomenon as far as We number and wettability effects for the initial stages of the evolution of the phenomenon are concerned, at least for the range of parameters investigated in this paper. Later, within a short time interval of approximately τ=0.1-0.6 the maximum pressure is approximately equal to 1.8-2.5 (Fig. 8, τ=0.317) and its distribution in space is forming an oblique pressure gradient pointing from the axis of symmetry towards the rim of the crown (Fig. 7. τ=0.613-

1.120, Fig. 8. τ=0.704-1.803). This pressure gradient is responsible for the formation of the crown, since it pushes liquid mass in the diagonal direction, while the shear stress from the recirculating gas phase at this region, enhances the development of the crown. At subsequent times the pressure inside the liquid is further decreasing and exhibits a quite uniform distribution in space.

More information and details for the experiments and the numerical results can be found in [9,10].

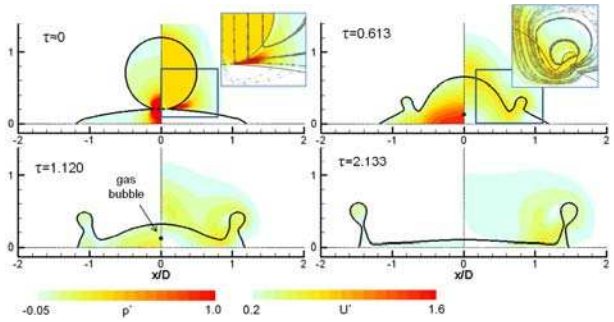

Figure 7: Selected frames of case A2 (We=161, Frh=340) showing the gas-liquid interface, the dimensionless pressure distribution (left hand side) and the dimensionless velocity distribution (right hand side). In the enlarged regions, representative streamlines are shown.

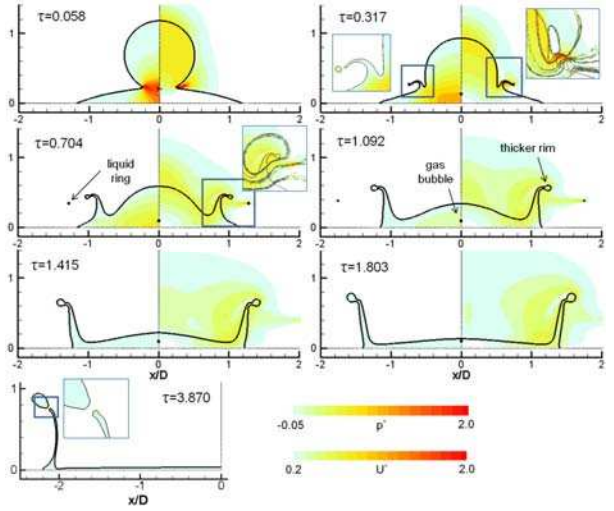

Figure 8: Selected frames of case F2 (We=391, Frh=1483) showing the gas-liquid interface, the dimensionless pressure distribution (left hand side) and the dimensionless velocity distribution (right hand side). In the enlarged regions, representative streamlines are shown.

CONCLUSIONS

The experimental analysis of the measurements revealed that the governing physics of this type of phenomenon is quite similar to the one controlling the impact of a droplet onto shallow liquid films, although the influence of the wall wettability introduces some important differences in terms of the shape of the aforementioned liquid bulk. The crown rim diameter follows a law similar to the case of a droplet impingement onto a uniform film. The VOF methodology has been used to predict a set of experimental data presented in detail in the first part of this work. The phenomenon of droplet impact onto a sessile droplet was approached following an axisymmetric formulation of the governing equations, which is valid for the initial and intermediate stages of the evolution of the phenomenon, applying simultaneously an adaptive local refined unstructured grid. The predictions of the numerical model were in good agreement with the experimental data for the crown's dimensions and base diameter. Following the model validation a comprehensive discussion of the flow field regimes was presented. During the early stages of impact high pressure is built up at the points of impact and inside the liquid mass an oblique pressure gradient is developed, promoting the formation of the advancing crown. The initial pressure built-up is responsible for the entrapment of gas bubbles inside the liquid, whilst bubble rings were also identified. At later stages, three-dimensional phenomena, such as the disintegration of crown's rim into secondary droplets are predicted, thus allowing for the axisymmetric simulation of the phenomenon to be valid until three dimensional characteristics are evident.

ACKNOWLEDGMENT

The financial grant of the European Commission through the Marie Curie Felloship (2003) and the support of UNIVERSITÀ DEGLI STUDI DI BERGAMO (Prof. M. Marengo, G.E. Cossali) are gratefully acknowledged.

REFERENCES

[1] Rein M., *Phenomena of liquid drop impact on solid and liquid surfaces*, Fluid Dynamics Research, 12 (1993) 61-93.
[2] Nikolopoulos N., Theodorakakos A., Bergeles G., *Normal impingement of a droplet onto a wall film: a numerical investigation*, International Journal of Heat and Fluid Flow, 26 (2005) 119-132.
[3] Nikolopoulos N., Theodorakakos A., Bergeles G., *Three-dimensional numerical investigation of a droplet impinging normally onto a wall film*, Journal of Computational Physics, 225 (2007) 322-341.
[4] Nikolopoulos N., Nikas K.-S., Bergeles G., *A numerical investigation of central binary collision of droplets*, Computers & Fluids, 38 (2009) 1191-1202.
[5] Nikolopoulos N., Theodorakakos A., Bergeles G., *Off-centre binary collision of droplets: A numerical investigation*, International Journal of Heat and Mass Transfer, 52 (2009) 4160-4174.
[6] Strotos G., Nikolopoulos N., Nikas K.-S., *A parametric numerical study of the head-on collision behavior of droplets*, Atomization and Sprays, 20 (2010) 191-209.
[7] Nikolopoulos N., Theodorakakos A., Bergeles G., *A numerical investigation of the evaporation process of a liquid droplet impinging onto a hot substrate*, International Journal of Heat and Mass Transfer, 50 (2007) 303-319.
[8] Rioboo, R., Bauthier, C., Conti, J., Voue, M., and Coninck, J., *Experimental investigation of splash and*

crown formation during single drop impact on wetted surfaces, Exp. Fluids, 35:648–652, 2003.
[9] N. Nikolopoulos, G. Strotos, K.S. Nikas, A. Theodorakakos, M. Gavaises, M. Marengo, G. E. Cossali. *Experimental investigation of a single droplet impact onto a sessile drop*, Atomization and Sprays, 20(10), (2010), 909–922.
[10] N. Nikolopoulos. G. Strotos, K.S. Nikas, A. Theodorakakos, M. Gavaises, M. Marengo, G. E. Cossali. *Single droplet impacts onto deposited drops. Numerical analysis and comparison*, Atomization and Sprays, 20(10), (2010), 935–953.
[11] Cossali G.E., Coghe A., Marengo M., 1997, *The impact of a single drop on a wetted solid surface*. Experiments in Fluids, 22, 463-472
[12] Cossali G.E., Brunello G., Coghe A., Marengo M., 1999. *Impact of a single drop on a liquid film: experimental analysis and comparison with empirical models*. Italian Congress of Thermofluid Dynamics UIT, Ferrara 30 June.
[13] Cossali G.E., Marengo M., Coghe A., Zhdanov S., 2004. *The role of time in single drop splash on thin film*. Experiments in Fluids, 36, 888-900.
[14] Hirt C.W., Nichols B.D., *Volume of Fluid (Vof) Method for the Dynamics of Free Boundaries*, Journal of Computational Physics, 39 (1981) 201-225.
[15] Jasak H., *Error analysis and estimation for finite volume method with applications to fluid flows*, in, Ph.D Thesis, Imperial College of Science Technology & Medicine, University of London, 1996.
[16] Ubbink O., Issa R.I., *A method for capturing sharp fluid interfaces on arbitrary meshes*, Journal of Computational Physics, 153 (1999) 26-50.
[17] Ubbink O., *Numerical prediction of two fluid systems with sharp interfaces*, in, PhD Thesis, Department of Mechanical Engineering, Imperial College of Science, Technology & Medicine,University of London, 1997.
[18] Theodorakakos A., Bergeles G., *Simulation of sharp gas-liquid interface using VOF method and adaptive grid local refinement around the interface*, International Journal for Numerical Methods in Fluids, 45 (2004) 421-439.

INVESTIGATION OF FUEL WALL FILMS USING LASER – INDUCED – FLUORESCENCE

Florian SCHULZ [C], Jürgen SCHMIDT

Institute of Fluid Dynamics and Thermodynamics
Otto-von-Guericke University Magdeburg
PO 4120, 39106 Magdeburg, Germany
[C]Corresponding author: florian.schulz@ovgu.de

ABSTRACT
Modern gasoline engines use the principle of direct injection. During the warm-up and for early injections the spray droplets contact the piston surface. As a result of the spray-wall interaction a wall film occurs. The liquid film as a fuel rich zone is one important reason of high soot emissions. Therefore it is necessary to carry out investigations on wall film forming and evaporation. It is aimed to reduce the wall film mass. The method of Laser-Induced-Fluorescence is able to quantitatively visualize wall films. Using this technique it is possible to study the effects of spray shape, orientation, operating pressure, injection quantity as well as distance from the wall.
The boundary conditions of the test section are close to those of an emission test engine. As a simplified approach the LIF measurements are taken under normal ambient conditions. The applied injector is a common high-pressure six hole nozzle controlled by a magnetic system. Two parameters were varied: the injection pressure and the distance between nozzle and wall. As a result the spatial and time resolved wall film thicknesses were found.
The first aim was to design a sensitive setup without using intensifiers. This resulted in a very fine-resolution gray scale and height information. Subsequently the analysis of the measuring system and the calibration were conducted.

INTRODUCTION

The first known investigations of water films were performed by Hopf in 1910. The method using a micrometer screw to measure the film thickness was used by scientists until 1963. In the meantime new methods were developed. Dunkler and Berglin (1952) measured capacity differences and Jackson (1955) was the pioneer using a radioactive tracer in the fluid. In 1964 Hewitt et al. were conducting the first fluorescence based film measurements followed by Hiby in 1968.

So the idea of applying fluorescence to wall films is known since 60 years. But with the development of intense and precise excitation sources the method became more applicable. Le Cos et al. (1994) were one of the first using a laser for inducing the fluorescence in liquid films. At the beginning point wise measurements were performed, eg. Meingast et al. 2000 or Lindgren et al. 2002. For many applications selective height information are sufficient. So Cheng et al. and Lida et al. published local LIF wall film measurements in 2009. Due to further developments in laser and camera hardware recently the first spatial resolved wall film thickness experiments have been carried out. Alonso et al. (2009) were interested in gasoline films and Magnusson et al. 2010 were investigating diesel films.

The method is based on findings of Bouger (1729) and Lambert (1760) who described the phenomena of light absorption. Later Beer (1852) found that the transmittance of light depends on the absorband concentration. For the Laser-Induced-Fluorescence the tracer represents the absorband and so the LIF-signal is proportional to the absorbed light. In this sense the Beer-Lambert-Law can be written as follows:

$$I_f = \cdot I_0 \cdot \left(1 - \exp\left(- \cdot C \cdot h\right)\right) \qquad (1)$$

The dependency on the wavelength does not emerge from the equation. So the fluorescence signal intensity $\boldsymbol{I_f}$ is directly proportional to the intensity of the excitation radiation $\boldsymbol{I_0}$ and to the quantum efficiency $\boldsymbol{\phi}$. From special interest is the logarithmic correlation between the LIF-signal and the length of the light path $\boldsymbol{h}$ (e.g. film thickness). The molar absorption coefficient ε and the molar concentration of the absorband $\boldsymbol{C}$ (e.g. tracer) have the same behaviour. The experiments described in this paper are based on this correlation.

EXPERIMENTAL METHOD

This study focuses on the LIF investigations of spray-wall interaction and fuel films. As a first approach the injection process of the real homogeneous charged Otto engine is replaced by the experimental setup illustrated in figure 1. The fuel is ejected onto a flat 50 × 50mm quartz surface by a symmetric six hole gasoline nozzle for central position. Only one of the six spray jets is used for the evaluation.

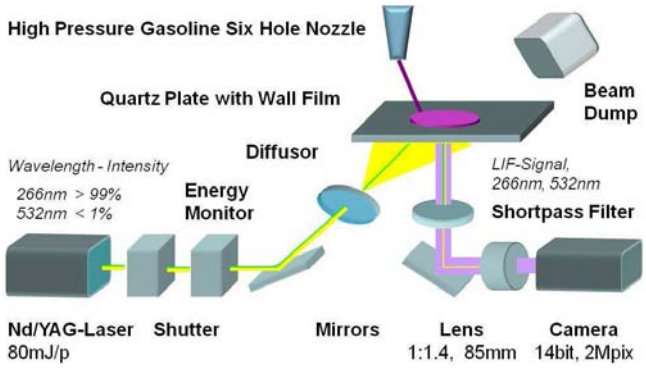

Figure 1: Schematic experimental setup

Both the Nd/YAG-Laser which excites the fuel and the camera which represents the LIF-signal detector are located underneath the quartz plate. In this arrangement, the interruption effect of the spray is minimized in the visualization. Decoupling the forth harmonic wavelength of 266nm the Spectra-Physics Quanta Ray LAB-170-10 Nd/YAG-Laser provides pulse energy up to 120mJ/pulse at a frequency of 10Hz for a pulse duration of only 4ns.

The high energy of one pulse will immediately start to evaporate the liquid film, which causes a bubble formation. Therefore it is necessary to expand and homogenize the laser profile and to reduce the laser power. By setting laser power to 80mJ/pulse and adjusting the beam profile the maximum fluorescence signal can be archived. Contrary to previous experiments using continuous lasers the film-images have a high sharpness of movement resulting from the short pulse duration.

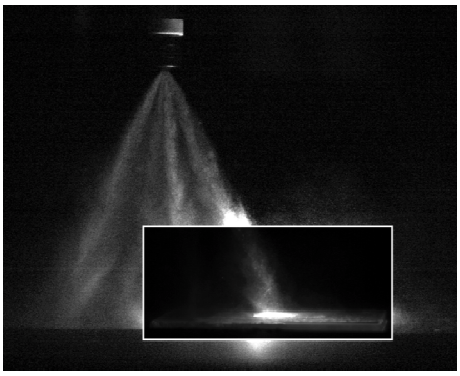

Figure 2: Side view of the injection onto a quartz plate

Two more components are important for working with a pulse laser. The laser shutter which is placed directly behind the laser blocks the beam. For safety reasons the radiation passes the shutter only during the recording. Behind the shutter the energy monitor is located. Because the laser exhibits a pulse to pulse energy fluctuation the energy monitor detects the individual pulse energy. Later the signal is used for correction purposes.

properties	**iso-octane**	**3-pentanon**
boiling point [°C]	99	101
density [g/cm^3]	0.69	0.81
molar mass [g/mol]	114.2	86.1
vapor pressure at 20°C [hPa]	51	37.6
heat of vaporisation [kJ/mol]	38.5	35.1

Table 1: Properties of iso-octane and 3-pentanone

In the early phase of the experiments it was found that most surfaces in the lab and also the mirrors and lenses are sensitive –in form of fluorescence– to the laser radiation which caused significant background noise. Therefore it is necessary to minimize the number of laser optics and to avoid light scattering by a precise alignment of the optical laser path. Also the beam dump is indispensable. In this context the beam expander with its lenses was substituted by one 5° UV diffuser optic to achieve a homogeneous laser profile. The width of the homogenized laser profile is set by adjusting the distance between diffuser and quartz surface.

The LIF Signal is detected by an Imager pro X 2M camera combined with the trigger controlling from LaVision. The 14-bit CCD camera, with 16,000 gray levels, has a resolution of 1,600 × 1,200 pixels. In combination with the 85mm Zeiss lens with a set f-number of 1.4 the maximum of light can be captured. This composition enables a very fine gray-scale and height resolution. In addition a 20mm extension tube was mounted between camera and lens. Because the area of interest has an extension of only 50 × 50mm this is necessary to obtain a maximum spatial resolution. According to this, the area of 1 × 1mm is represented by 1024 pixels. This is much more than required for a good image. But for the post processing it is useful in order to smooth sensor noise without losing spatial information.

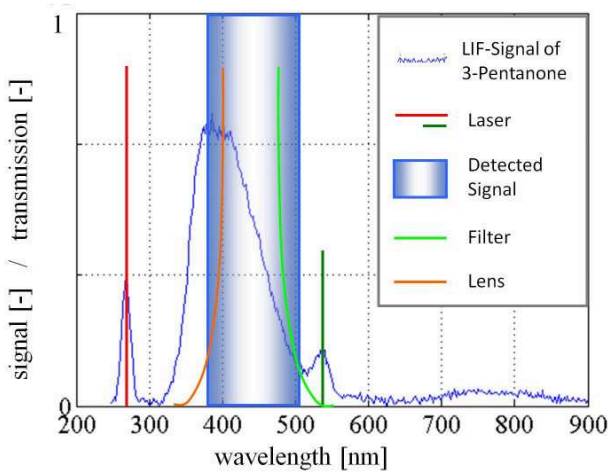

Figure 3: Wavelengths and signal location

The injected liquid can be considered as a component of the experimental setup. It influences the signal intensity and the wavelength of the LIF signal and therefore the other components of the setup. For instance, if the signal wavelength is only found in the UV region, an intensifier with UV lens has to be used. In the present study the binary mixture of 5% vol. 3-pentanone in iso-octane was chosen as fuel substitute. Iso-octane is the basis and non-fluorescing. The LIF-signal producing tracer is 3-pentanone. Compared to other tracers, like toluene, 3-pentanone produces only a very low response signal (Fujikawa et al. 1997, Wieland et al. 2005). But the physical and chemical properties match best with those of iso-octane (table 1). That is why in combustion systems research the combination of iso-octane and 3-pentanone is commonly used as a substitute of gasoline. Another important issue is that 3-Pentanone is most sensitive to an excitation wavelength of 266nm.

For LIF measurements one of the most important issues is the selection of the signal wavelength. Since the LIF-signal of 3-pentanone is really low it is necessary to avoid the detection of signals which do not have their origin within the wall film. Therefore the spectral response of 3-pentanone in iso-octane was measured in a fluorescence spectrometer (RF-5301PC). The response signal of 3-pentanone excited with 266nm is plotted in figure 3. To

capture only the wall film signal the 532nm laser radiation is cut off with the help of a 500nm (FWHM of 10nm) short-pass filter. Signals below 360nm are absorbed by the lens. Radiation noise within the sensitive detection field is deleted in the post processing.

CALIBRATION

To be able to derive a height information from the LIF-signal a precise height calibration is necessary. Therefore three different calibration methods were tested. First the most common thickness calibration, second the concentration calibration and third the droplet calibration were carried out. All three methods are supposed to give the desired LIF-signal intensity for a known film height. This correlation can be applied for the following film height measurements.

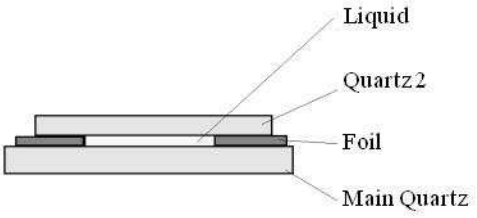

Figure 4: Film height calibration setup

Figure 4 illustrates the setup for the thickness calibration. By positioning a foil between the main quartz plate and second quartz plate a defined distance inside the plates is generated. Both quartz glasses have a very smooth surface with a corrugation less than 150nm. Two foils were used, one with a thickness of 40µm and another with 80µm. So that it was possible to adjust eight film thicknesses between 40 and 320 µm. Of course eight steps would not be necessary if a linear correlation between the LIF-signal intensity and the film height is assumed – like it is usually done for thin layers. But this assumption and the reproducibility of the calibration should be proven for the setup. The 3-pentanone / iso-octane mixture was injected with a syringe und drawn into the gap by capillary force. In order to avoid buoying upward of the upper quartz the plates were clamped together.

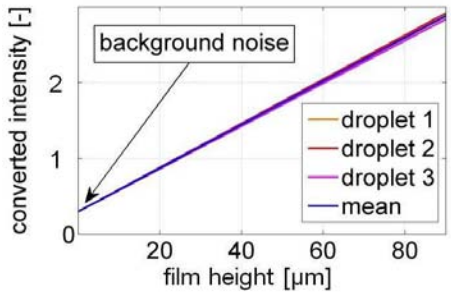

Figure 5: Results from droplet calibration

The same setup is used for the second method, the concentration calibration (Cheng et al. 2010). This calibration was executed in combination with the thickness calibration just by varying the concentration of 3-pentanone between 1.25% and 15% (vol.). The idea of this calibration is that there is the same correlation between the LIF-signal and concentration like it is between the LIF-signal and film thickness. This results from the Beer-Lambert-Law. Using this relationship it is sufficient to set one defined film height and change the concentration of 3-pentanone.

For the droplet calibration as the third method a droplet with a defined volume is placed onto the main quartz plate. Although using a micro syringe it is difficult to obtain the desired volume. This is due to the adhering liquid on the syringe and evaporation. Therefore a series of droplets was balanced on a high resolution balance, in order to get a mean droplet size. This is about 10% below the adjusted syringe volume. For the later experiments the LIF-signal / height correlations of at least three droplets were averaged. But figure 5 demonstrates that the calibration curves match really close.

There are different approaches to receive the LIF-signal / height correlation out of the droplet images e.g. the refractive index matching imaging introduced by Drake et al. (2002) for a rough surface. Because of the thin films as a first approximation a linear correlation was used. With the help of the LIF-Signal / volume correlation,

$$\frac{I_{f,pixel}}{\sum_{ij} I_{f,ij}} = \frac{h_{pixel}}{\sum_{ij} h_{ij}} = \frac{h_{pixel}}{V_{drop} / A_{pixel}} \qquad (2)$$

a height for each pixel is calculated. This leads to a slight overestimation of the film thicknesses. The estimation will soon be substituted through the Beer-Lambert-Law, which leads to a nonlinear system of equations.

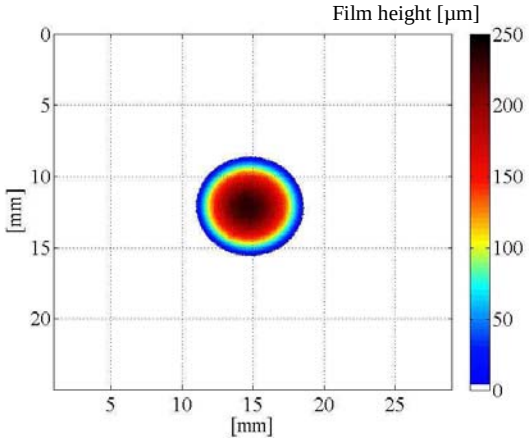

Figure 6: Droplet height

The experimental results show that the concentration method is the most sensitive method. It is very difficult to create a mixture with an error less than 5% (vol.). Therefore the results scatter. The measurements of the fist method are very reproducible. It was found that the LIF-signal behaves linear up to certain thicknesses, for instance for 5% (vol.) of 3-pentanone up to 160µm or for 10% (vol.) of 3-pentanone up to 80µm. Beyond this height the logarithmic trend starts to get visible. For both calibrations – the first and the second method – an additional quartz was used to adjust a defined height. But it became evident that this quartz influences the measuring system. Especially, due to light scattering at the edges of the quartz the background noise and the LIF-signal rises. The resulting

signal is not accurately comparable to the LIF-signals of wall films measured without the second quartz plate. That is why the droplet calibration was chosen for further investigations. A droplet image derived from a 5.4µl droplet is presented in figure 6.

IMAGE PROCESSING

Quantitative Laser-Induced-Fluorescence measurements always require a detailed post-processing. For this reason it is necessary to prepare the experiments before starting the measurements. Therefore the adjustment of the laser power was carried out first with a Coherent power meter, FieldMaxII-TOP. In this step the sensitivity range of the energy monitor was attuned to the laser power.

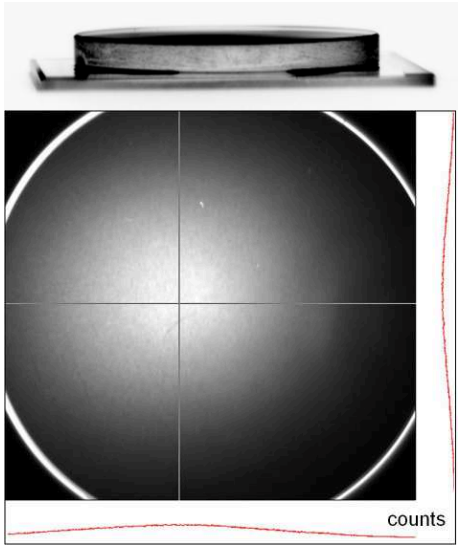

Figure 7: Laser profile image (bottom), side view negative (top)

The first record is a dark image to smooth the sensor signal. This is necessary because of a different sensitivity of the MOS capacitors. A background image can help to erase the noise which occurs between the fuel film and the camera, e.g. on the mirror in front of the camera.

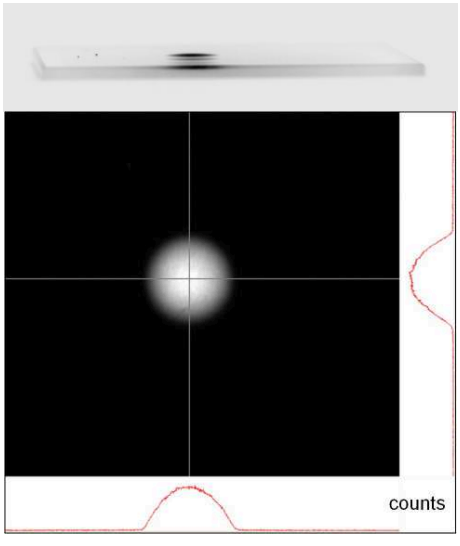

Figure 8: Droplet image (bottom), side view negative (top)

The second step is to take a laser profile image (figure 7), because the spatial distribution of the excitation energy must be considered in the calculation. To get the laser profile the same setup as in figure 4 was used. At last droplet images like figure 8 are recorded. After this procedure the wall film experiments were executed.

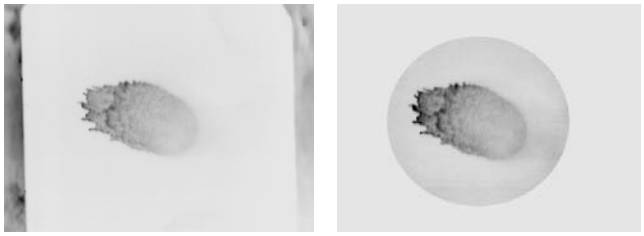

Figure 9: Wall film raw image (left), Wall film image energy and profile corrected (right)

In the post processing procedure all images are energy corrected, first. Here the pulse energies of the images recorded by the energy monitor are set into a relationship and the overall image intensities are adapted. This is followed by the profile correction. The intensities of areas with lower laser power are adapted to the maximum value. Figure 9 contrasts the raw image of a wall film with the energy and profile corrected image. This is also done for the droplet images. With the help of these images the LIF-signal / height correlation (figure 5) is calculated. Applying the film height function to the processed wall film intensity fields, the film thickness information is obtained. As an example in figure 10, the film thickness image of figure 9 is plotted.

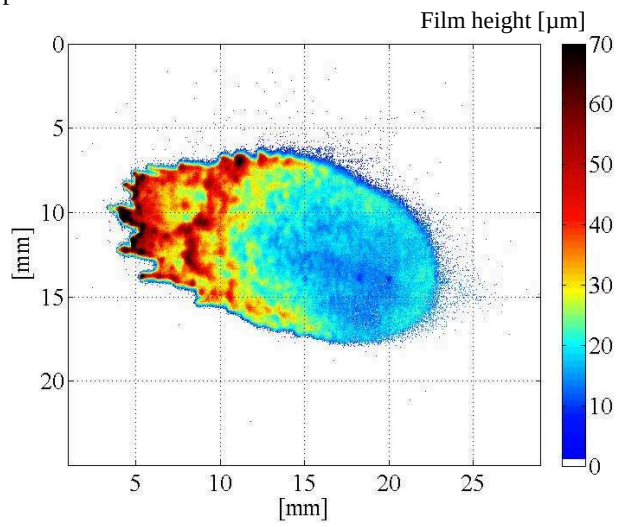

Figure 10: Wall film height image

CONCLUSION

This report highlights the opportunities to study fuel wall films with the use of Laser – Induced – Fluorescence. Compared with previous studies, the use of modern hardware allows much better information about the fuel distribution and the wall film heights. However, this requires a detailed calibration of the measurement system. For the intensity calibration different methods were tested.

The drop calibration provided the most accurat reproducible calibration results.

Following the post-processing, it is possible to compare the resulting wall films. Thereby, the influences of the boundary conditions can be determined and quantified. Interesting parameters are the maximum wall film height, the film area and the deposited fuel mass. The implementation of parametric studies is planned. Singe images of preliminary investigations are presented in figure 11. The images are taken 10ms after start of injection and the injected fuel mass is constant.

The financial support of the German Research Foundation (DFG-Graduiertenkolleg 1554) is gratefully acknowledged.

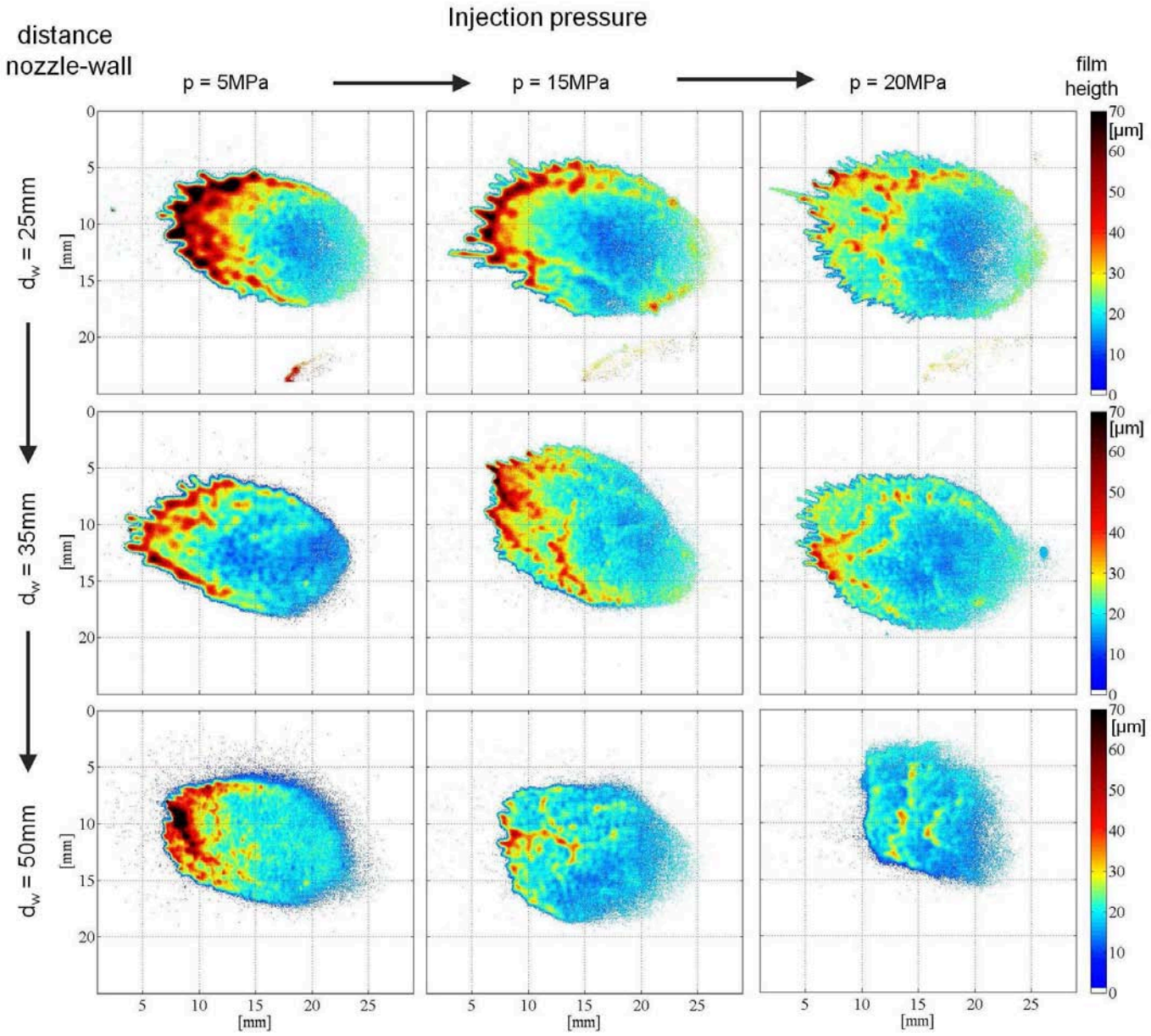

Figure 11: Film thickness images for different boundary conditions

REFERENCES

[1] Alonso M., Kay P. J., Bowen P. J., Gilchrist R., Sapsford S., ***A laser induced fluorescence technique for quantifying transient liquid fuel films utilising total internal reflection***, Exp Fluids 48 (1) 2010, S. 133–142.

[2] Beer A., ***Bestimmung der Absorption des rothen Lichts in farbigen Flüssigkeiten***, Annalen der Physik und Chemie. 86, 1852.

[3] Bouguer P., ***Essai d'optique, Sur la gradation de la lumière***, Claude Jombert, Paris 1729.

[4] Cheng Y., Deng K., Li T., ***Measurement and simulation of wall-wetted fuel film thickness***, International Journal of Thermal Sciences 49 (4) 2010, S. 733–739.

[5] Cho H., Min K. ***Measurement of liquid fuel film distribution on the cylinder liner of a spark ignition engine using the laser-induced fluorescence technique***, Measurement Science and Technology 14 2003, S. 975–982.

[6] Drake M. C., Fansler T. D., Rosalik M. E., ***Quantitative High-Speed Imaging of Piston Fuel Films in Direct-Injection Engines using a Refractive-Index-Matching Technique***, ILASS Americas, Madison,WI, 2002, S. 58–62.

[7] Dukler A.E., Berglin O.P., ***Characteristics of flow in falling liquid films***, Chem. Engng. Progr., 48, 557/563, 1952.

[8] Fujikawa T., Hattori Y., Aklhama K., ***Quantitative 2-D fuel distribution measurements in an SI engine using laserinduced fluorescence with suitable combination of fluorescence tracer and excitation wavelength***, SAE technical paper series 972944; 1997.

[9] Hewitt G.F., Lovergrove P.C., Nichols B., ***Film thickness measurement using fluorescence technique***, Pt. 1. Description of the method; AERE-R 4478, 1964.

[10] Hiby J.W., Eine Fluoreszenzmethode zur Untersuchung des Transportmechanismus bei der Gasadsorption im Rieselfilm, Wärme- und Stoffübertragung, 105/116, 1968.

[11] Hopf L., ***Turbulenz bei einem Flusse***, Ann. Phys., 777/808, 1910.

[12] Jackson M.L., ***Liquid films in viscous flow***, AIChE J., 231/240, 1955.

[13] Lambert J. H., ***Photometria, sive de mensura et gradibus luminis, colorum et umbrae***, Sumptibus Vidae Eberhardi Klett, 1760.

[14] Meingast U., Staudt M., Reichelt L., Renz U., Sommerhoff F.-A., ***Analysis of Spray/Wall Interaction under Diesel Engine Conditions***, SAE Technical Paper (2000-01-0272), Detroit 2000.

[15] Le Coz J.F., Catalano C., Baritaud T., ***Application of laser induced fluorescence for measuring the thickness of liquid films on transparent walls***, Proc. 7th Int. Symp. On Applications of Laser Techniques to Fluid Dynamics, ed. Adrian RJ, Lisbon, Portugal, 1994, pp.29.3.1-29.3.8.

[16] Lida M., Yoshikawa K., Arcoumanis W., ***Fuel Film Behavior Analysis Using Simulated Intake Port***, SAE Technical Paper, 2009

[17] Lindgren R., Block R., Denbratt I., ***Development of a Wall Film Thickness Measurement Device***, Proceedings of the 1st International Conference on Optical and Laser Diagnostics, London, 2002.

[18] Magnusson A., Begliatti M., Hervás F.B., Andersson M., ***Characterization of Wall Film Formation from Impinging Diesel Fuel Sprays using LIF***, 23rd Annual Conference on Liquid Atomization and Spray Systems. Brno, ILASS – Europe 2010, S. 1–10.

[19] Park S., Ghandhi J.B., ***Fuel Film Temperature and Thickness Measurements on the Piston Crown of a Direct-Injection Spark-Ignition Engine***. Warrendale, SAE International 2005.

[20] Wieland K., ***Photophysical characterization of toluene and 3-pentanone for quantitative imaging of fuel/air ratio and temperature in combustion systems,*** PhD Thesis, University of Heidelberg, 2005.

Author index

ISBN – 978-88-97413-04-2